ABSTRACT

(Physics)

EXPERIMENTAL STUDIES OF TWO-DIMENSIONAL GRANULAR SYSTEMS USING GRAIN-SCALE CONTACT FORCE MEASUREMENTS

by

Trushant Suresh Majmudar

Department of Physics
Duke University

Date: _____

Approved:

_____
Robert P. Behringer, Supervisor

_____
Daniel Gauthier

_____
Henry Greenside

_____
David Schaeffer

_____
Thomas Witelski

An abstract of a dissertation submitted in partial fulfillment of the requirements for the degree of Doctor of Philosophy in the Department of Physics in the Graduate School of Duke University

2006

EXPERIMENTAL STUDIES OF TWO-DIMENSIONAL GRANULAR SYSTEMS USING GRAIN-SCALE CONTACT FORCE MEASUREMENTS

by

Trushant Suresh Majmudar

Department of Physics
Duke University

Date: _____

Approved:

_____
Robert P. Behringer, Supervisor

_____
Daniel Gauthier

_____
Henry Greenside

_____
David Schaeffer

_____
Thomas Witelski

Dissertation submitted in partial fulfillment of the
requirements for the degree of Doctor of Philosophy
in the Department of Physics
in the Graduate School of
Duke University

2006

Abstract

In this thesis we will investigate the behavior of two-dimensional granular systems using novel contact force measurements. One of the most unusual aspects of granular systems is the inhomogeneous distribution of boundary forces in the bulk sample. Investigating this behavior requires us to study the behavior of the system under different loading conditions like isotropic compression, and shear. Most experimental studies of granular systems have relied upon measurements at the boundaries of the system. Though useful, these measurements do not provide information about the micro-mechanics of the system. Information about the grain-scale behavior of the system is important to distinguish between various models of force distributions in granular systems.

In light of this, we have developed a novel experimental method that allows us to measure the normal and the tangential contact forces, for each grain, at every contact. Our approach utilizes the property of birefringence exhibited by some materials, and allows us to visualize the stresses within each grain. We use the stress information and solve the inverse problem of obtaining the contact forces that produce a given stress pattern. We use these contact force measurements to study isotropically compressed, and sheared states.

We find significant differences in the distributions of normal forces for sheared and isotropically compressed systems. For sheared systems, the distribution of normal forces has an exponential tail, whereas for isotropically compressed systems, the distribution falls faster than an exponential. We also find that sheared systems show anisotropic force-chain structure with long force chains roughly along principal strain directions. We quantify this anisotropy by compution two-dimensional force-force correlations, and find long-range, almost power-law like correlation in the direction

of force chains. Isotropically compressed systems have only short-range correlations in all directions. The spatial correlation of forces serves as a quantitative measure for the qualitative idea of force-chains. Next we focus our attention on each of these systems, and study them individually.

For isotropically compressed systems, we study the problem of jamming. We find the exact point where the system jams. Theoretical studies have indicated that a loose granular system under compression jams at a critical packing fraction, and that the average number of contacts per grain grows in a power-law fashion, with an exponent of 0.5. We indeed find a transition point in the packing fraction, and a power-law growth of average contact number. We find that the exponent of the power-law can range from 0.5-0.56, depending on the choice of the critical packing fraction. The pressure in the system increases with the distance from the critical packing fraction, as a power-law, with an exponent of 1.1.

In the next set of experiments, we focus on the evolution of sheared systems, specifically from the point of view of plastic deformation. We study the grain motions, and the stress-strain behavior of the system under one cycle of forward and reverse shear. From the contact force measurements, we find that the stress-strain curve for the system is clearly hysteretic - signifying energy loss in the system. It has linear elastic segments interrupted by drops in stress of varied magnitudes. The stress drops signify plastic events. The grain motions also reveals interesting features. There are three distinct regions in which the grains move differently; two corners where the grains show homogeneous elastic displacement separated by a diagonal band consisting of vortices. This pattern is completely destroyed upon reversing the direction of shear. The initial pattern of the displacements of grains in the reverse-shear phase is more quadrupolar in appearance.

Acknowledgements

I would like to thank many people who have helped and supported me over the years. These people include:

- My advisor, Bob Behringer, for his guidance, and encouragement. I consider myself fortunate to have had the opportunity to learn from him.
- My fellow lab mates, Bob Hartley, Junfei Geng, Meenakshi Dutt, John Wambaugh, Brian Utter, Karen Daniels, Peidong Yu, Ken Mckenzie, Jun Uehara, Brian Tighe, Mathias Sperl, Jeanman Sur, Jie Zhang, Shomeek Mukhopadhyay, and Jean-Phillipe Matas.
- My parents, brother, Dev, and sister, Shivani.
- My wife, Hemali Phatnani, without whom none of this would be possible.

Contents

List of Tables

List of Figures

Chapter 1

Introduction

This thesis deals with granular systems, and my attempts at understanding the many fascinating properties of systems as simple as sand. I will take the experimental approach towards this goal, but with an eye on, and making use of the theoretical developments of the last century. The questions I will address will be simple. How and why do granular systems behave differently in many respects than other solid or fluid systems? Before I can answer these questions, I must begin by describing what are granular systems, and why study them in the first place. I will briefly describe some unique features of granular systems. I will then describe my attempts at studying granular systems.

1.1 Granular systems: definition and description and relevance

We are all aware of granular systems. These grainy materials are so ubiquitous that often we do not pay any attention to the fact that we handle such materials on a daily basis. Sand on the beach, sugar, salt, cereal, the list can go on and on. So what are granular systems? Simply put they are systems composed of a large collection of *macroscopic* grains, interacting with each other, and the fluid surrounding them. If the grains do not interact with the surrounding fluid, then the system is termed *dry granular material*, as opposed to a wet granular material, for example, the wet sand on the beach. In this thesis we will deal exclusively with dry granular systems.

Let us make our definitions more precise and describe a few properties of granular systems:

- Grain sizes can range from a few hundred microns to several meters and beyond.
- Grains interact via repulsive contact forces.
- The contact interactions are frictional and highly dissipative due to kinetic friction.
- Thermal energy is negligible compared to the kinetic and the potential energy of the grains; granular systems are *athermal*.

We will take up each of these items in turn. Grains in a granular systems can span a very large range of size scales; from a few hundred microns (powders) to several meters (boulders). The scales can even be larger, as in the case of rings of saturn, which are composed of very large rocks. In dry granular systems, there are no attractive interactions between the grains, which in turn means that unlike an elastic solid, an aggregate of grains do not support tension or stretching. This property has important consequences for the stability of the system.

Friction plays an enormously important role in inter-grain interaction. As we will see shortly, static friction between the grains results in history dependence, i.e the state of the system at any given time depends on its entire history. Sliding friction dissipates most of the energy in a very short time, causing terrestrial granular systems to remain stationary unless a large amount of energy is continuously put in the system.

Thermal fluctuations have no effect on the dynamics of the system. Consider an average grain of size $\approx 1mm$, and mass $\approx 1mg$. Its potential energy difference in moving by a height equal to its diameter is given by $\delta E_p = mgd \approx 10^{-8}$ Joules. In contrast, the thermal energy scale at room temperature of $300 \deg K$ is $E_T =$

$kT \approx 10^{-21}$, where k is the Boltzmann constant. Thus, $\delta E_P >> E_T$, which in effect means that the grains do not respond to thermal fluctuations. Unlike fluids or gases, granular systems do not reach equilibrium through grain-motion generated via thermal fluctuations.

The frictional dissipation of energy, and the athermal nature of granular systems results in the rather unique consequence that granular systems can remain in a metastable state indefinitely, unless extra energy is supplied externally. For example, unlike fluids, sand poured from a container makes a heap instead of spreading out like a liquid.

All of these properties mentioned above may sound as if they are mainly scientific curiosities, but these properties have enormous consequences for many industrial processes, and environmental events. For example, many industries store granular materials in silos, which tend to break inexplicably as shown in Figure 1.1d, mostly during discharge of the material from the silo [Eib84]. This problem has been studied for decades, but as yet has eluded complete solution. It has been reported that 40% of the chemical processing industry deals with granular materials [EGD94]. Other issues relevant for industries include better methods of mixing granular systems, and avoiding segregation of grains of different sizes. These isuues have enormous economic implications, and even a minor improvement would mean billions of dollars in savings.

Besides the industrial applications, there is a plethora of naturally occurring phenomena involving granular materials, from beautiful examples sand dunes (Figure 1.1b), to catastrophic events like avalanches Figure 1.1c. These phenomena are equally fascinating and challenging to understand. A whole range of scientific disciplines like physics, geophysics, mechanical engineering, chemical engineering, and materials sciences, are involved in studying these phenomena.

Having seen some examples of granular systems in this section, we now turn to a

(a)

(b)

(c)

(d)

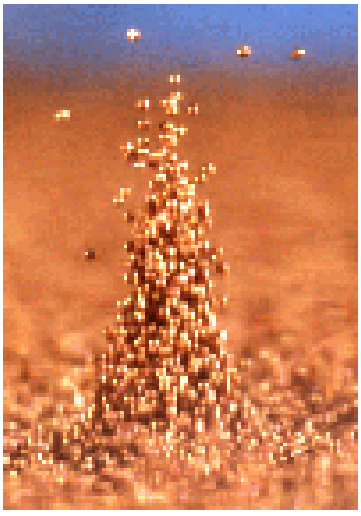

(e)

Figure 1.1: Images of granular systems: (a) Sand castle. (b) Sand dunes. (c) Snow avalanches. (d) Collapse of a silo. (e) vertically oscillating granular system.

more technical description relevant for our studies. Although some of the examples discussed earlier are cases of dynamic granular systems, in this thesis we will deal exclusively with static or quasi-static systems. In the next section we describe some unique features of granular systems relevant to such static and quasistatic systems.

1.2 Unique features of granular systems

Granular systems can behave like solids, liquids, or gases [JNB96b]. Consider sand in a container. When it is just sitting undisturbed, it behaves like a solid, whereas if it is poured out of the container, it flows and behaves like a liquid. A dust storm, on the other hand, is an example of a granular system behaving like a gas. We will focus here on understanding some properties related to static, and slowly moving systems.

1.2.1 Contact forces, friction, and indeterminacy of the forces

The all-important property for granular systems, from our point of view, is the nature of contact forces between grains of the system. As mentioned earlier, the contact forces are *repulsive*, *frictional*, and *dissipative*. We will consider peculiar effects of each of these properties.

Grains in any realistic dry granular system resist being compressed against each other. They are usually hard grains but not infinitely rigid. This resistance manifests itself as a repulsive force between particles, much like pushing on a spring. At the same time, for dry granular systems, there are no attractive forces between the grains. One consequence of this is the lack of ability to support tension in the system; a granular system cannot be stretched like a spring or a rubber band. This causes granular systems in some metastable states to be extremely fragile to perturbations.

The other component of the contact force between any two grains is the frictional

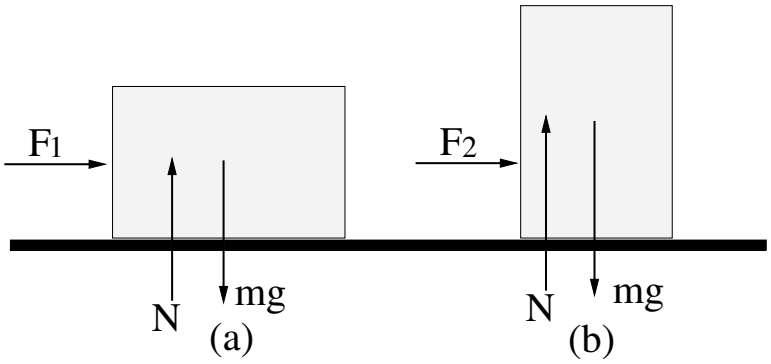

Figure 1.2: Schematic diagram of the normal and frictional forces on a solid.

force. Frictional forces are of central importance to our understanding of the varied phenomena exhibited by granular systems. Before describing its role in granular systems in detail, let us review the well-known laws of solid friction, first given by Amontons in the seventeenth century [Amo99], and a little later by Coulomb [Cou76].

Figure 1.2 shows a solid body resting on a solid plane, in two different orientations. The forces acting on the body are also shown in the diagram. There is the normal force acting on the body. The Amontons-Coulomb law states that the force required to move the body horizontally must exceed its normal force multiplied by the friction coefficient, which is a constant of the material. As long as the applied force is less than this value the body remains at rest. Hence for a body in static equilibrium:

$$\mid F_T \mid \leq \mu F_N \tag{1.1}$$

Once the applied force exceeds this critical value, the body begins to slide. The force required to move the body is the same in both configurations in Figure 1.2. The force of friction does not depend on the area of contact. A noteworthy point here is that the law of friction is in the form of an inequality, which permits a whole continuum of values allowed for the force of friction.

The dissipative aspect of contact forces come into play, once the grains start sliding against each other. When two solid bodies slide past each other, *kinetic*

friction causes a loss of energy. The kinetic force of friction is the force needed to keep the body moving at a constant speed. It is typically lower than the force of static friction. In the absence of a constant driving force, the body quickly comes to rest, losing all of its energy to heat.

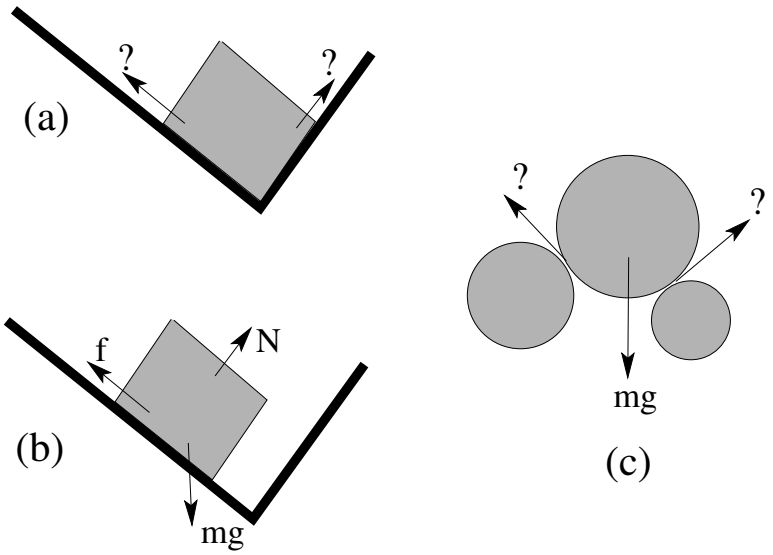

Figure 1.3: Schematic diagram of the indeterminacy of contact forces caused by friction.

We now come to probably the most important issue related to the work presented in this thesis, which stems from the inequality in the law for frictional forces. Figure 1.3 shows schematic diagram of what is known as the *indeterminacy of forces*. It shows a block placed between two perpendicular plates with friction. Let the final resting place of the block be at the intersection of the two plates, as in Figure 1.3a. The crucial point is that it is *not possible* to determine the forces on the block just by looking at the final rest position of the block. If the block came to this position by sliding along left plate, the force of friction would be along the left plate, whereas if it slid along the right plate, the force of friction would be directed along the right plate as shown in Figure 1.3b. *The forces on the block are indeterminate unless one knows the history of its dynamics.*

For frictional solids in contact, it is essential to know how the solids came in contact with each other. This is equally true of grains in a granular system, as shown in Figure 1.3c. The all important issue for us is that the contact forces between the grains can not be determined from a single snapshot of the system, even if one could see all the grains, and knew exactly how they were placed relative to each other. This is due to indeterminacy of the forces; one would need to know the entire history of the assembly.

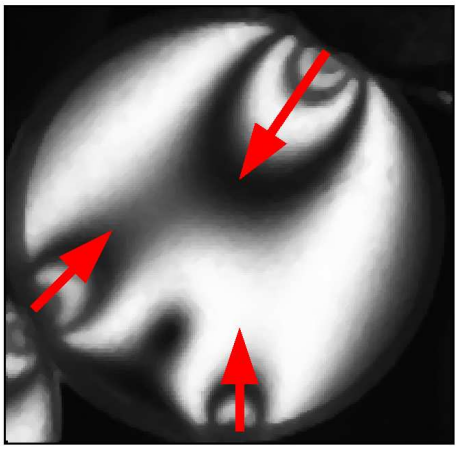

Figure 1.4: An image of a disk with three forces, red arrows show the vector forces.

The second aspect of the same indeterminacy is the mathematical solvability of a mechanically stable configuration. Consider a disk with three forces acting on it, as shown in Figure 1.4. The three vector forces are shown by red arrows. Each force has two components, normal and tangential. In all, for this disk we have six unknown variables. On the other hand, if the disk is in mechanical equilibrium, we have force balance and torque balance. The force balance gives two relations, one for each component of the net force. The torque balance gives one condition between all the force components. This leaves us with three constraints on the six unknowns, an *under-determined* system of equations. Thus, unless extra information regarding the forces is supplied for this system, it can not be solved, even if we know the exact

contact locations. The situation just gets a lot more complicated when we have an aggregate of grains. In order to know all the contact forces for a stable static ensemble, information besides positional data is crucial.

It is the very first goal of the work presented in this thesis to find a method for extracting all the contact forces, both the normal and the frictional forces, for a single grain irrespective of the number of contacts it has, and then extend it to all the particles in the system and find all the forces from a single snapshot of the system.

1.2.2 Distribution of forces

The most striking consequence of the properties described in the previous section occurs in the way external forces are distributed throughout a granular medium. Finite size of the grains, and their frictional properties contribute to a highly unusual response of granular systems to external loads. Under moderate amounts of compression or shear, a granular system exhibits a very fragile balancing act between the grains, where a group of grains are supporting other groups of grains by forming a delicate contact network. This property has a dramatic effect on the way external forces are distributed within the system.

One of the most fundamental features of granular systems is the inhomogeneous distribution of interparticle forces. The most striking evidence of this heterogeneous distribution is in two-dimensional photoelastic systems, where the effect of interparticle forces can be visualized by using birefringent particles. At the system size scales, this inhomogeneity of distribution appears as a filamentary structure of particles carrying more than the average load applied to the system. These groups of particles have been dubbed "*force chains*" [Dan57, HBV99].

Figure 1.5 shows an image of a two-dimensional granular system of birefringent disks. The stressed disks have colored bands, whereas unstressed disks have the

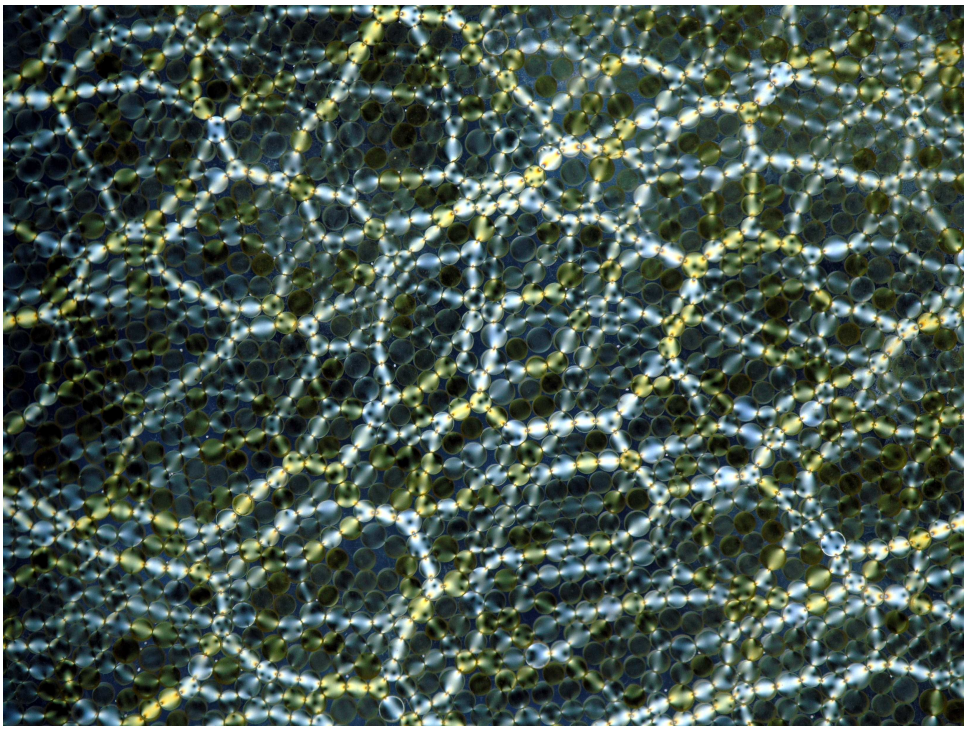

Figure 1.5: A snapshot of force-chains in a two-dimensional granular system of photoelastic disks

background intensity. The heterogeneous distribution of boundary stresses, and the network of force-chains is clearly visible.

One of our goals in this thesis is to understand this heterogeneity in the distribution of forces, or the force-chain structure, in granular systems under different boundary loads. The example shown here of a two dimensional granular system is ideally suited for studying the problems associated with the distribution of forces, especially since these forces can be readily visualized using the property of birefringence exhibited by some materials. The technique of utilizing birefringence to visualize stresses in a material is known as photoelasticity [CL31, Fro41].

In this thesis, we will utilize photoelasticity to exclusively study two-dimensional granular systems. The kind of questions we want the answers to, can most effectively be studied with two-dimensional systems using birefringent particles. The next sec-

tion describes the history of the photoelasticity method briefly, and prior reseach on the problem of force distributions in granular systems.

1.3 Photoelastic method and force distributions

Photoelasticity as a technique to study stress and strain distributions in solids has a century-old history. It was first developed and utilized in France by Mesnager in 1901 [Har40]. It has since been extensively used by the engineering community to determine stress distributions in usually two-dimensional [DR65, Hey52], and recently in three dimensions [ADG92, AD94]. Its use in studying particle aggregates dates back to 1950s, when civil and mechanical engineers needed to find stress distributions in granular aggregates [Dan57, DdJdJ72a]. Over the years the use of this technique has become much more sophisticated and its use in studying granular aggregates has grown [DSR00].

Over last ten years, Bob Behringer's laboratory has utilized photoelastic techniques to study a variety of important problems in granular physics [HB99, GHL$^+$01, HB03] and in the process pioneered a resurgence of interest in its use to study problems in granular physics.

The presence of force chains gives rise to a number of unusual properties exhibited by granular systems in static or even dynamic situations [JNB96a]. In static situations, one of the problems which has been studied for a long time is the response of the granular system to localized loads [dG98, VHC$^+$99], or finding the "Green's function" of the system. Many theoretical models [BCC95, CLM$^+$96, LNS$^+$95, WCC97, CWBC98, CBCW98, Soc98, GG02] have addressed the issue of the stress distribution in sandpiles or other geometries. In sandpiles assembled one grain at a time [vN81, VHC$^+$99, GHL$^+$01, GLBH01, Sav97], the pressure at the base is not necessarily maximum right under the apex of the pile, as one would intuitively expect.

Instead, the pressure maximum may occur somewhat away from the apex. One explanation for this effect is the formation of force-chains, which arch away some of the load sideways and shield the region right below the apex [WCC97].

Similarly in granular silos, the pressure does not increase indefinitely with depth, as it would if it were filled with a fluid [Jan95, VC99, VCB$^+$00, Eib84]. The explanation again is the presence of force-chains, which transfer some of the load to the walls of the silo, thus keeping the pressure constant beyond a certain depth. Of more importance is the failure of silos, the cause of which may be very short-lived, strong force-chains hitting the walls. The forces along the walls of the silos fluctuate by a large amount.

During the course of many experimental and theoretical investigations concerning the nature of stress distributions in granular systems, a strong case has emerged for a need to understand the distribution of contact forces, and equally importantly, their fluctuations and spatio-temporal properties like correlations between force chains [MOB96, MJN98, HB99, VHB99, Nic98, RWJM98].

One of the most enduring features found in many experimental and theoretical studies is the exponential tail in the probability distribution of forces [MJN98, CLM$^+$96, HB99, RJMR96a]. This is found to be true for systems that are static as well as those that are quasi-static. Recently new theoretical results have appeared pertaining force distributions in lattice models [TSS$^+$05, SvHSvS03], and in force ensemble models [SVvHvS04, SVE$^+$04], which suggest that the probability of force distributions may be different under different situations. Specifically, both the lattice model, and the force ensemble model obtain faster than exponential decay for large forces in isotropically compressed systems. For sheared systems, both models regain the exponential tail at high forces [TSS$^+$05, SvHSvS03]. Moreover, in the force ensemble model, the probability distributions of forces differ in the bulk system from

the boundary layers due to contact geometry effects [SEVvH06].

The predictions made by these models have further strengthened the growing body of evidence that granular systems behave differently under different boundary loads. If the system is compressed from all sides, the contact geometry, and the force distributions are different, than if they are sheared in any way. All of these issues have inter-grain contact forces as the fundamental property under investigation. Moreover, most of the numerical and theoretical studies have dealt with the idealized frictionless particles. As we have discussed earlier, friction is an important piece in the complete description of real granular systems, and it is of considerable interest to see under what conditions simulations with frictionless grains can adequately explain features observed in a real granular system.

1.3.1 Jamming

Sand in an undisturbed container remains stationary. Although the constituent material of sand is macro-sized solid grains, we do not say that sand is a solid. Instead the descriptive that has been used the most to describe any granular system at rest is *jammed*. The main reason for this is the observed fact that sometimes the system does not remain in that state when disturbed by the slightest amount. Sand after all can be poured out of the container just like a liquid. In this case we say that the system is flowing or *unjammed*. To be sure, these behaviors are very similar to ordinary solids and liquids, but there are significant differences between solids, liquids and granular systems in the way a granular system makes the transition from jammed to unjammed state and vice versa.

Consider a granular system in a container with a small hole through which the material canescapee. All of us have experienced the annoyance of trying to pour out a grainy material from a container, only to find that suddenly it gets stuck, and stops

flowing. This is very typical of granular systems but it never happens for an ordinary liquid. As long as the opening is of macroscopic size, a liquid will always ooze out. We can say that both the sand and a liquid are flowing, sand can repeatedly get stuck. This is the phenomenon of jamming in the simplest terms.

Many questions arise from these simple observations. For example, when does the system start flowing?. How does it flow ? Why does it stop flowing of its own accord? What material or other parameters do all these behaviors depend on? These questions and more have been studied for a long time by researchers in industries, and engineering and somewhat more recently by physicists.

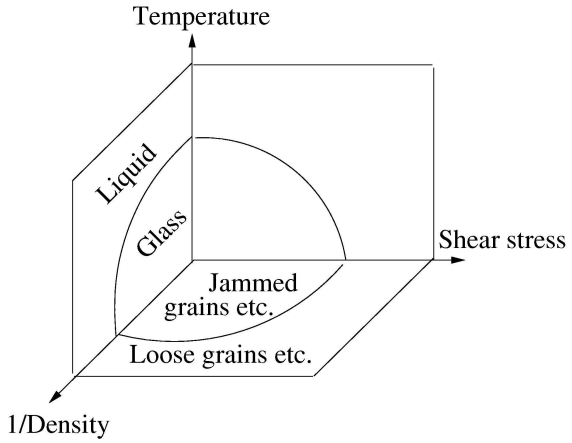

Figure 1.6: Phase diagram of jamming in granular and other systems.

An intriguing idea was put forward by Liu and Nagel [LN98] regarding the transition from jammed to unjammed state, which is captured by a speculative phase diagram shown in Figure 1.6. According to this idea, many systems, with attractive or repulsive interactions, can be tied together in terms of their jamming transitions. A liquid system with attractive interactions becomes jammed when its is supercooled below a critical temperature. Likewise for granular systems, the role of ordinary temperature may be replaced by shear stress. A granular system would jam only when its density was sufficiently high and the shear stress below a critical value. Above a

certain shear stress or below a critical density, the system may become unjammed.

Again, the transition from jamming to unjamming in a granular system in the phase space of density and shear stress depends on the behavior of the system under shear. Also the nature of this transition is truly critical or not is not a priori clear. These issues have to be resolved by experiments which can measure the phase space parameters like the density and the shear stress accurately. Although these parameters can be measured in both two and three dimensions, in three dimensions, measurements are made typically at the boundaries of the container. The shear stresses at the boundaries gets distributed in a highly anisotropic manner. This affects the strength of the system along different directions, and hence the stress at which the system unjams. In other words it may be easier for the system to unjam in certain directions but not in other directions.

A possible way to study these issues would be to measure and characterize mesoscale force-chains in different directions, under different boundary conditions. This brings us back to the need for measuring grain-scale contact forces, their spatial distribution in the form of force-chains, and correlations between these force chains in different directions.

In the end, it may turn out that for large enough systems, and at large enough length scales, the grain-scale detail of contacts and forces may not matter, but rather than assuming this to be true, it would be fruitful to verify it experimentally. One last idea before we end this introduction is the description of contact forces between realistic elastic bodies, which we take up in the next section.

1.3.2 Elastic bodies in contact

The problem of contact forces between real elastic solids was first studied by Hertz [HJS96] within the framework of the elasticity theory. He considered two elastic

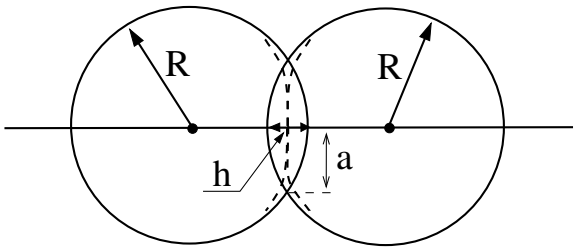

Figure 1.7: Two elastic bodies in contact: Hertz's law.

spheres compressed against each other, as shown in Figure 1.7. If the radii of the spheres are R, and the distance by which they are compressed is h, then Hertz's law gives the force exerted by each sphere on to the other as [LL70a]:

$$F = kh^{\frac{3}{2}} \tag{1.2}$$

where the coefficient $k = \frac{\sqrt{2}}{3}\frac{E}{1-\sigma^2}\sqrt{R}$, and E and σ are Young's modulus, and Poisson ratio respectively.

The force law for quasi-two dimensional solids, for example disks or cylinders, is somewhat more complicated by the fact that there is a logarithmic correction term [LL70a], and the force law becomes:

$$-Flog(F) \propto h \tag{1.3}$$

These laws work with remarkable accuracy, although they involve only normal forces. Finally we note that our model granular material is a collection of small elastic cylinders with circular cross section. Ideally, they should follow the two-dimensional law given in equation 1.3, but in reality, because they are three dimensional objects, and have many asperities, they tend to follow the Hertzian law for three-dimensional solids.

1.4 Overview

In the preceding sections, we have briefly touched upon some aspects of granular physics relevant to what follows in this thesis. It by no means exhausts the range of interesting and challenging problems in granular physics, but for the sake of brevity and our purposes here, we have restricted our discussion of the issues involved in granular systems. One idea that we hope has been conveyed in the preceding is the importance of contact forces in general, and a need to study the behavior of granular systems under different boundary conditions, in particular.

It is a common practice in soil mechanics to treat granular systems using continuum equations, ignoring the fluctuations of forces in the system. We have provided examples of how force fluctuations could play a crucial role in several phenomena. The exact nature of macroscopic description of granular systems starting from grain-scale descriptions is still an unresolved issue. Part of the difficulty lies in lack of experiments with grain-scale information about the forces in bulk systems. The other difficulty arises from theoretical point of view. Many theoretical models with radically different microscopic assumptions and mathematical structure end up giving reasonable agreement with the observed behavior. Without the facility of having experiments with grain-scale data to test the microscopic assumptions, and macroscopic predictions, it becomes impossible to distinguish between various models of force distributions, stress transmission and the response of a system to perturbations. There is a definite need for developing experimental methods, which can obtain information about the grain-scale contact forces in bulk granular systems. With the help of grain-scale positional, and stress information, we can begin to build up our understanding of the behavior of granular systems from micro to macro scales.

In this thesis, we plan to accomplish several goals:

- To study two-dimensional granular systems and use birefringent disks to visualize stress.
- To solve the inverse problem of finding the normal and the tangential contact forces for each contact from the experimental stress data in the bulk sample.
- To prepare granular systems under different boundary conditions like isotropic compression and shear and study the distribution of forces, the structure of force-chains.
- To study isotropically compressed systems from the point of view of jamming, and to determine the jamming transition point for the system.
- To study the plastic deformation, energy dissipation and the stress-strain relashion in sheared systems.

Chapter 2 will introduce the technique of photoelasticity and describe in detail our method of obtaining the contact forces from experimental images. In chapter 3, we apply our method of finding contact forces to study isotropically compressed, uniaxially compressed and sheared granular systems using a biaxial test apparatus. In chapter 4, we focus on jamming transition in isotropically compressed systems. In chapter 5, we study plastic deformation in sheared systems.

Chapter 2

Experimental techniques

Experimental approaches to granular systems depend on the number of spatial dimensions of the system under investigation. They also depend on the scale of the system under scrutiny, i.e the grain-scale or the meso-scale consisting of clusters of few tens of particles or the system size scale. In order to carry out the program outlined in the introduction, we need experimental information about the positions, velocities and forces at all the scales in order to construct a consistent picture of the behavior of the system from micro to macro scale. This means measuring the positions, velocities and the forces experienced by the grains in bulk system as well as macro-scale motion of the system and boundary forces. This is a daunting task for a full three-dimensional (3D) granular system consisting of realistic grains which are irregularly shaped and frictional.

It has been possible to obtain positional information of the grains in bulk two-dimensional (2D) systems [HB99] and at the boundary of a 3D system [CLFB$^+$06, DB05]. It is also possible to obtain stress information at the boundary of a 3D system [EMJN02, MJN98]. Obtaining stress information at the grain scale in bulk 3D systems without disturbing the system is an extremely challenging experimental problem with very few partial solutions so far [ZM05, BWS$^+$05] .

In order to be able to measure grain scale properties of the system, and to understand the emergent macro-scale behavior of the system, we focus exclusively on 2D systems in this thesis. The main reason for this choice is that in 2D systems, we can not only measure positions and velocities of the grains but also the contact forces on each grain in the system. This allows us to completely specify the micro-

mechanical state of the system. We can then take a bottom-up approach and try to understand the macro-scale properties like the force distributions, response function of the system, stress-strain relations and plastic deformation of the system under shear.

Measurements of contact forces at the grain scale are made possible by a novel experimental technique, which forms the first step in this thesis and the crux of this chapter. The main idea behind this technique is to utilize the property of birefringence exhibited by some materials which allows visualization of stress when viewed with polarized light. The observed stress field inside a grain is then used to infer the contact forces that produce the stress field.

In the rest of the chapter, we will begin by covering the basic concepts of photoelasticity which is the optical phenomena exhibited by birefringent materials and concepts of elasticity theory, which models such materials. We will then describe the manner in which these two ideas are combined to form what is known as an inverse problem, i.e computing the contact forces from a given experimental stress pattern. Finally, we will demonstrate, for the first time to our knowledge, successful implementation of our automated method for solving the inverse problem for a large assembly of grains.

2.1 Birefringence, photoelasticity and polariscope optics

Birefringence is a property of certain crystalline and polymeric materials in which the index of refraction within the material changes in response to externally applied stress [CL31, Fro41, DR65, Hey52]. These materials effectively rotate the polarization of light passing through them. A clever utilization of this photoelastic property consists of a stressed sample is viewed through crossed polarizers. This optical setup in which

the sample is placed between two polarizers, with the light source on one side of the sample and the camera on the other side, is known as a polariscope. Viewing the sample in this fashion shows a striking pattern of colored bands (for a white light source) within the sample, which is directly related to the internal stress state of the sample. Details about the phenomenon of birefringence and many of the formulations that follow can be found in references mentioned. Here, a brief description of the process will be given.

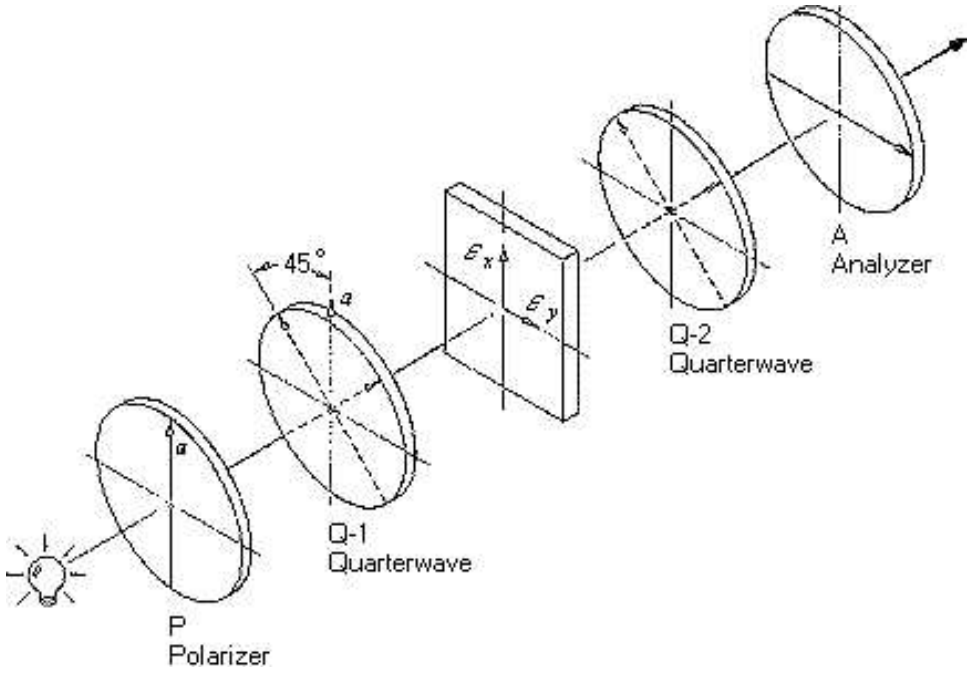

Figure 2.1: Schematic of a circular polariscope containing a sample to be analyzed between complimentary circular polarizers (From Vishay Measurements Corp. www.vishay.com).

Figure 2.1 shows the schematic setup of a typical circular polariscope. The sample to be analyzed is placed between two crossed circular polarizers (a circular polarizer is a combination of a polarizer and a quarter-wave plate). The quarter wave plates on either side of the sample are aligned with their axes mutually perpendicular. The light from a source passes through a circular polarizer and enters the sample. Light traveling within a stressed sample splits into two components depending on polar-

ization, each traveling with different velocities. Due to the differences in velocities, different polarizations of light emerging from the sample come out with different phases at different points of the sample.

In brief, a stressed birefringent sample becomes anisotropic in its optical properties and the index of refraction is spatially varying. Instead of being a scalar constant, now the index of refraction has tensorial form. For a 2D sample, there are two principal values of the index of refraction at every point of the sample. The variation in the index of refraction results in phase variations of the light emerging from the sample. The spatially varying phase α is related to the principle indices of refraction by:

$$\alpha(x, y) = \frac{2\pi(n_1 - n_2)t}{\lambda} \tag{2.1}$$

where t is the thickness of the material, n_1 and n_2 are the principle values of refractive indices, and λ is the wavelength of the light.

The fundamental equation of photoelasticity relates the changes in the refractive index to the stress-state of the sample

$$(n_1 - n_2) = C(\sigma_1 - \sigma_2) \tag{2.2}$$

where σ_1 and σ_2 are the principle values of the stress tensor of the sample, and C is the stress-optic coefficient. The above two equations, when combined, give the relation between the phase of the light emerging from the sample and the principle stress values:

$$\alpha = \frac{2\pi C(\sigma_1 - \sigma_2)t}{\lambda}. \tag{2.3}$$

The goal of traditional photoelastic analysis is to extract the phase α, and infer principle stresses from it. This goal would be simple to accomplish were it not for the

nonlinear optical response of the light intensity. The intensity of the light emerging from the sample and captured by the camera is given by:

$$I(x,y) = I_0 \sin^2(\alpha/2) = I_0 \sin^2[\frac{(\sigma_1 - \sigma_2)\pi C t}{\lambda}] \tag{2.4}$$

where I_0 is the maximum intensity emerging from the sample. This is a nonlinear, periodic function. A simple inversion gives values of phase only in the range 0 to $\pi/2$ instead of increasing magnitude of alpha with increasing stress difference.

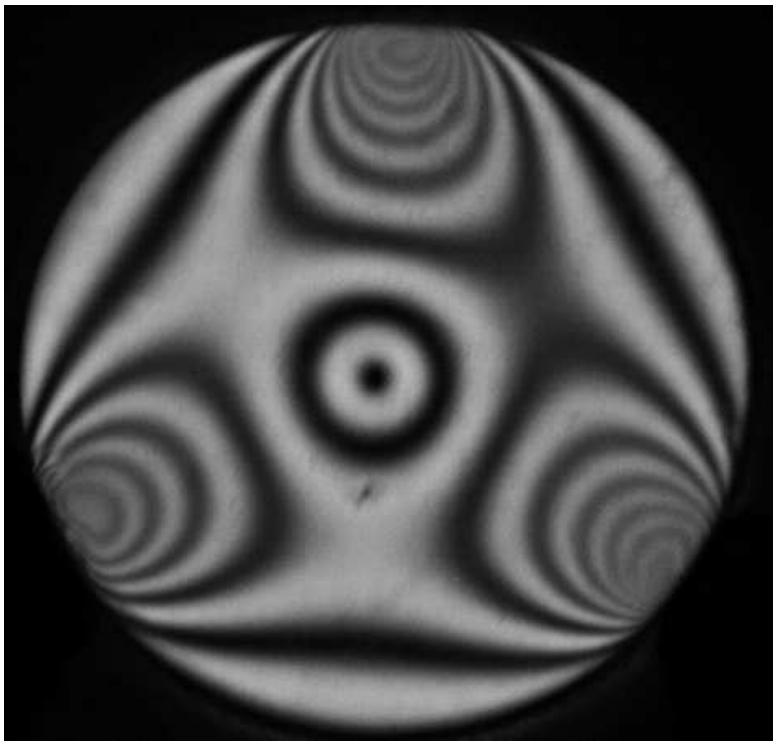

Figure 2.2: Experimental stress pattern of a photoelastic disk with three loads.

The problem of obtaining the phase information or the stresses can be better understood by looking at the image of a stressed photoelastic disk as in Figure 2.2. The disk is under three radially compressive loads. The loads deform the disk and produce stresses in the disk. A pattern of dark and bright bands (for monochrome light source) is seen, which represent contours of equal principle stress difference.

From equation 2.4, it can be seen that whenever the phase of the sin function is an integer multiple of π, the observed intensity drops to 0. This is seen as a dark band. By the same token, whenever the phase of the sin function is an odd half integer multiple of π, the intensity function reaches a maximum and is seen as a bright band. These bands are known as "fringes" and the whole pattern of fringes is known as the "fringe pattern". The density of fringes is low at the edge of the disk and increases towards the contacts. The phase α is the smallest around the edges of the disk and increases towards the contacts. The photoelastic analysis problem is to determine the absolute value of the phase with respect to the phase of the stress-free region. This is difficult to achieve using only a single monochrome image since the phase at a reference point is not known a priori.

Development of various strategies to unwrap the phase and obtain full-field phase information is still an active area of research [Ram00]. In one such approach the phase at a point is assigned manually and then phases at other regions of the sample are calculated. Other more automated approaches make use of two images at two different wavelengths [Che97]. Phase shifting methods involve capturing multiple images at different relative angles between the analyzer and the polarizer. RGB photoelasticity involves capturing full color images and finding the phases at arbitrary loads using calibration look-up tables (LUT) [Ram00]. In this thesis, we will make use of variants of the greyscale and the RGB photoelasticity method. These methods are more suitable when an automated photoelastic analysis is needed on a large collection of particles.

The experimental problem we address in this thesis goes a step beyond getting just the phase information of a stressed sample: ultimately we want to solve the inverse problem of finding the contact forces that produce a given stress pattern inside a sample. This problem can be solved by invoking an appropriate model which

provides analytic expressions for the stress components in an elastic material given the boundary forces. We then fit the experimental data and the model in least-squares sense and obtain contact forces as best-fit parameters.

In order to accomplish this task, we must first choose a model based on the theory of elasticity which represents the situation under investigation reasonably well. A further simplification is introduced by selecting an appropriate model granular system: throughout this thesis, our model granular system is a collection of thin elastic disks of circular cross section. The advantage of choosing thin circular disks as opposed to more realistic shapes of naturally occurring granular media is that the analytic expressions for the stresses are readily calculable using 2D elasticity theory. When such a collection of circular disks is compressed or sheared, they come in contact with each other and exert contact forces on each other. From the grain-scale point of view, when the system is in static equilibrium, the situation can be viewed as if each disk is acted on by arbitrary number of contact forces in arbitrary directions such that the forces and torques are balanced. We need to find a general solution for this case of a single disk and apply it disk by disk on the entire collection. In the following section we will briefly review the essential theoretical concepts of elasticity theory, specifically 2D plane elasticity theory which is used to solve the inverse photoelastic problem.

2.2 Theory of elasticity

An elastic body, as we generally know, is one which can change its shape and size under the action of applied forces and comes back to its original shape and size once those forces are removed. The fundamental quantity which can be used to quantify this behavior is the distance between any two points of the material. Mathematically an elastic material, as opposed to an ideally rigid material, is one in which the distance

between any two points changes in response to externally applied forces. The change in an element of length in the body is known as strain. The definitions of some of the important quantities and useful formulae will be given in the following. The details can be found in many authoritative treatises on elasticity theory [LL70b, TG70]. A brief description can be found in Appendix.

Consider an elastic body described with a fixed set of axes. Let the position vector of a point before deformation be $\mathbf{r}$ and after the deformation be $\mathbf{r}'$. The displacement vector of the point denoted by $\mathbf{u}$ due to the deformation is given by $u_i = x'_i - x_i$, where the subscripts i refer to the three spatial components x,y, and z.

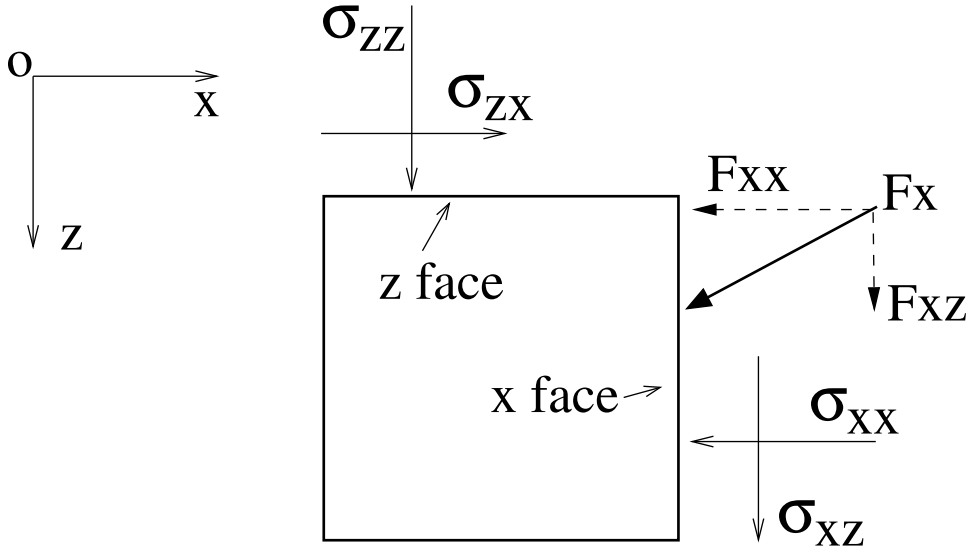

Figure 2.3: Stress tensor components for a two dimensional plane x-z.

The distance between the points after the deformation dl' is related to the distance before the deformation dl via:

$$dl'^2 = dl^2 + 2u_{ik}dx_i dx_k \tag{2.5}$$

where u_{ik} is known as the strain tensor and is defined as:

$$u_{ik} = \frac{1}{2}\left(\frac{\partial u_i}{\partial x_k} + \frac{\partial u_k}{\partial x_i} + \frac{\partial u_l}{\partial x_i}\frac{\partial u_l}{\partial x_k}\right) \tag{2.6}$$

The strain tensor is symmetric tensor, i.e. $u_{ik} = u_{ki}$. The principal values or the eigenvalues of this tensor denote the three independent strains in the three mutually perpendicular directions. The eigenvectors of the tensor are then the principal directions. For small deformations only the first two terms in equation 2.6 are considered as the third term is of higher order and much smaller than the first two terms.

The next important quantity in describing an elastic solid is the stress tensor. This tensor describes the response of the material to externally applied force. Thus if F_i is the applied force in a given direction, then the force on any volume can be written as an integral over the closed surface bounding the volume:

$$\int F_i dV = \oint \sigma_{ik} df_k \tag{2.7}$$

The component σ_{ik} is the i-th component of force on unit area perpendicular to the x_k-th axis, and df_k are the components of the surface element vector $d\vec{f}$, directed along the outward normal. This can be seen from Figure 2.3, where for simplicity stress components are shown for a 2D plane. Although the stress tensor for a deformed elastic solid varies spatially, if the body is in equilibrium, an average of the stress tensor over the entire solid can be calculated, and expressed by a simple formula which involves only the boundary forces and the locations of their points of application.

$$\bar{\sigma_{ik}} = \frac{1}{2V} \oint (P_i x_k + P_k x_i) dA \tag{2.8}$$

where $P_{i,k}$ are the boundary forces, $x_{i,k}$ are the coordinates of points of applications of the forces, dA is the surface area element and V is the volume of the solid.

The fundamental relationship between the stress and the strain in an elastic body is obtained by thermodynamics arguments [LL70b]. The stress tensor is the derivative

of the free energy with respect to strain at constant temperature,

$$\sigma_{ik} = \frac{\partial F}{\partial \sigma_{ik}} \tag{2.9}$$

The relationship between stresses and strains is in general a complicated nonlinear function. If the deformation is small, then for many elastic solids, the strains are linear functions of stresses. This law is known as Hook's law and is expressed for an isotropic solid as:

$$u_{ik} = \frac{\delta_{ik}\sigma_{ll}}{9K} + \frac{(\sigma_{ik} - \frac{1}{3}\delta_{ik}\sigma_{ll})}{2\mu} \tag{2.10}$$

where δ_{ik} is the Kronecker delta, and K and μ are the bulk modulus and shear modulus respectively.

In order to be able to use the formalism of elasticity theory for our model granular system, we need to introduce one more simplification and consider the case in which both the stress and the strain are only in one plane. This results in a considerable simplification and allows for an effectively 2D analysis of a 3D problem [Her82]. The plane elasticity approximation is valid if both the the stresses and strains are small and the z-components of the stress and the strain are zero. We next consider the 2D plane elasticity and its application to solve the problem of a thin disk under external forces.

2.2.1 2D plane elasticity: the problem of concentrated forces on a thin disk.

The plane elasticity approximation is very useful in the context of deformation of thin plates due to external forces. The cases which involve longitudinal deformation of the plates without any bending form a special class of problems. The simplest case we

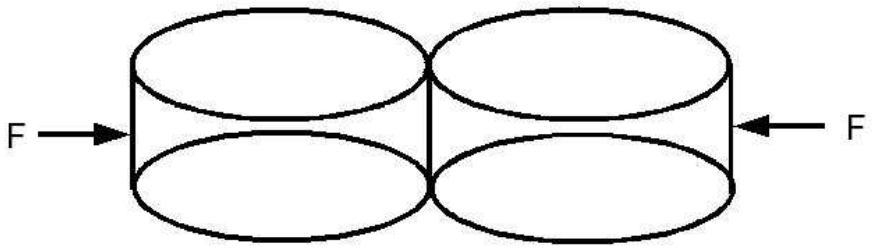

Figure 2.4: Two disks in contact with external force F acting on them.

want to consider is depicted in Figure 2.4. If the plate, which in our case is a circular disk, is at equilibrium, then the forces and torque on it are balanced. If it is sufficiently thin, then the strains can be regarded as uniform over its thickness and only the x and y components of strains are non zero. Similarly the stress tensor also has only x and y components. Thus, the elastic stress tensor reduces to a two dimensional tensor with three independent components σ_{xx}, σ_{yy}, and σ_{xy}, since the tensor is still symmetric and $\sigma_{xy} = \sigma_{yx}$. Now that we have obtained considerable reduction in the complexity of the problem, we need to apply the formalism to the thin disk problem and obtain the solution of stress components in terms of the external forces.

The first step in the solution is to obtain the solution for a point load on a half plane, schematically shown in Figure 2.5. The detailed derivation is given in the Appendix; here we briefly mention some important features of the solution (in radial coordinates with the axes as shown in the figure). A point load acting on a half plane produces radial stresses. The circular regions inside the half plane are lines of equal radial stress. σ_{rr}. The two other components involving the θ coordinate, $\sigma_{r\theta}$ and $\sigma_{\theta\theta}$ are zero due to the symmetry of the problem. The radial stress decays as $1/r$, and has the following functional form:

$$\sigma_{rr} = -\frac{2F}{\pi t}\frac{\cos(\theta)}{r} \tag{2.11}$$

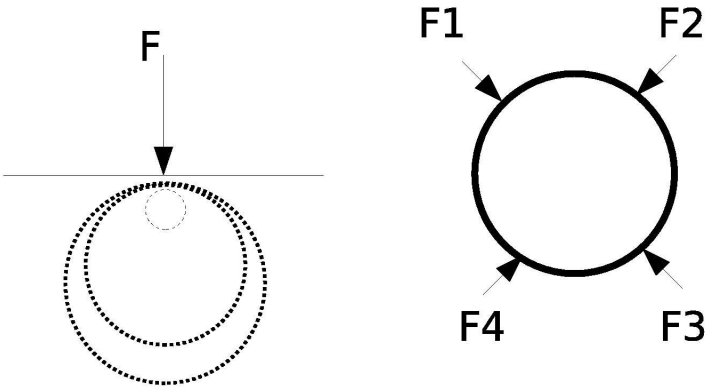

Figure 2.5: Half plane and a circular disk under compressive loads.

where F is the applied load, t is the thickness of the plane, θ and r are the coordinates of the point under consideration. The half plane solution forms the basis for many 2D elasticity problems including the solution for the circular disk problem.

The general solution for a disk acted on by arbitrary number of forces in arbitrary directions is obtained by considering each contact separately and treating that contact as a point force on an elastic half plane. Contributions from each contact are added up and a correction term is added to match the boundary condition [Appendix]. The correction term is required because the circumference of the disk is stress free except at the points of application of the forces. Adding the contributions for each contact separately results in non-zero boundary stresses which need to be made zero by adding the appropriate correction terms. A specific example of the disk problem and the solution is given below. The general solution for any arbitrary situation can be found in the Appendix.

Consider the case where a disk is in equilibrium under the action of two equal and opposite forces, as shown in Figure 2.6. The left panel shows the schematic diagram

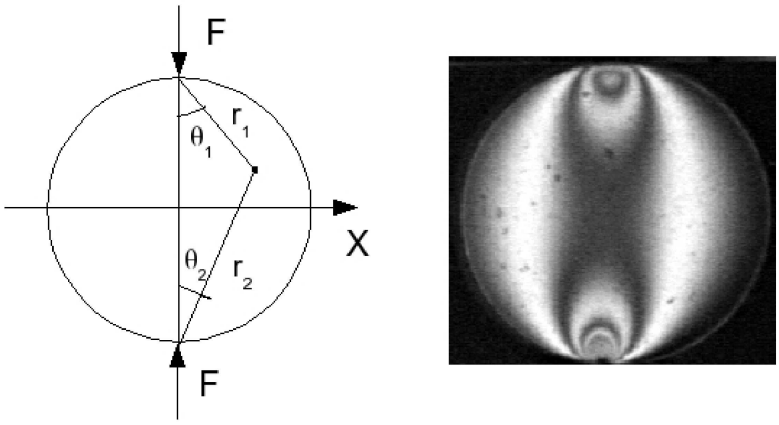

Figure 2.6: Left: Diagram of a disk with two equal and opposite forces. Right: An experimental example of the case.

of the situation. At any point in the disk, the radial stress has two contributions of the type in equation 2.11. Thus the total radial stress at any point is

$$\sigma_{rr}^{total} = \sigma_{rr}^{1} + \sigma_{rr}^{2} \tag{2.12}$$

$$\sigma_{rr}^{1} = -\frac{2F}{\pi t}\frac{\cos(\theta_1)}{r_1} \tag{2.13}$$

$$\sigma_{rr}^{2} = -\frac{2F}{\pi t}\frac{\cos(\theta_2)}{r_2} \tag{2.14}$$

In Eqs. (2.12)-(2.14), each r and θ is measured from the point of application of the force as shown in Figure 2.6. Also, each of the radial stress contribution is directed towards the respective loading points. At the boundary of the disk $\theta_2 = 90^\circ - \theta_1$. Adding both contributions for the boundary of the disk results in an overall radially compressive load of magnitude $\sigma_n = -2F/\pi td$, where d is the diameter of the disk. The correct stress distribution is obtained by adding a uniform tension of magnitude $\sigma_n = 2F/\pi td$ to the solution σ_{rr}^{total}. The deformation of the disk can be obtained easily from the stress components, since for two dimensional, linear, and isotropic elastic solids, the stresses and strains are directly proportional.

The general solution of this problem was first given by Mitchell [MMFJ64]. He

showed that the stresses at any point in the disk produced by N concentrated loads are obtained by combining in appropriate manner radial stress contribution by each contact, and adding to it the isotropic tension σ_n which satisfies the boundary conditions:

$$\sigma_{rr} = -\sum_{i=1}^{N} \frac{2F_i}{\pi t} \frac{\cos(\theta_i)}{r_i} \tag{2.15}$$

$$\sigma_n = \sum_{i=1}^{N} \frac{2F_i}{\pi t d} \sin(\theta_1 + \theta_2)_i \tag{2.16}$$

$$\sigma_{total} = \sigma_{rr} + \sigma_n \tag{2.17}$$

The above set of equations are the solutions we have been looking for. In a large collection of disks at static equilibrium, each disk may have a different number of forces of arbitrary magnitudes and directions, but for each such disk the stress field is given by a solution outlined above. From the above set of equations, we can calculate an analytic expression for $\sigma_1 - \sigma_2$ [Appendix], which is used in equation 2.4. In this way we can create a theoretical model for the observed intensity patterns. The formula for $\sigma_1 - \sigma_2$ depends on the spatial coordinates within the disk and also on the normal and the tangential contact force components, which we intend to extract from the experimental data.

The next stage in the our method involves analysis of the photoelastic images and fitting the observed photoelastic stress patterns within each disk to the model developed above. We will take up each of these issues in the next two sections.

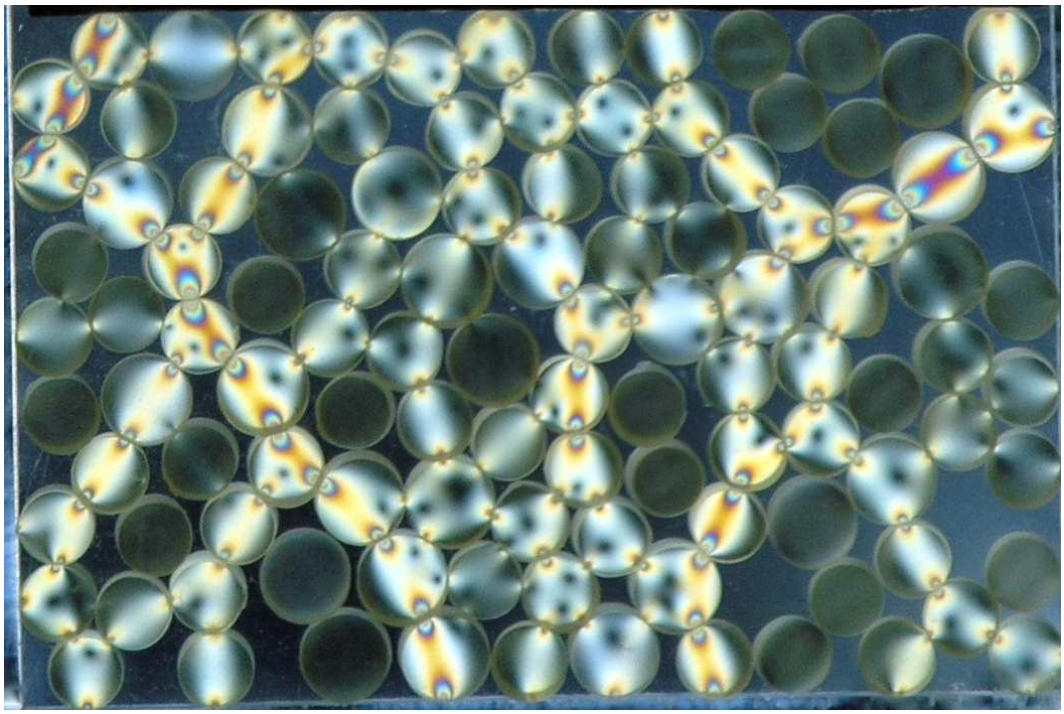

Figure 2.7: An experimental image of stress patterns in a collection of photoelastic disks.

2.3 The inverse photoelastic problem: problem statement and the solution

We have developed the necessary theoretical background for addressing the central experimental challenge put forward in the beginning of this chapter. The experimental problem can be defined much more precisely for our experimental system and understood more clearly with the help of an experimental image. Figure 2.7 shows an experimental image of a collection of photoelastic disks confined in a rectangular enclosure and under compressive boundary forces. The boundary forces are distributed within the system in a non-uniform manner with different disks carrying different amounts of loads. Each disk under compression shows a stress pattern produced by the contact forces acting on it. It can observed that the stress pattern of each disk is different, even if only slightly, from any other disk. More quantitatively, the

stress state of each disk depends on the number of contacts it has, the location of the contacts, and the magnitudes and directions of each of the contact forces. Since the number of combinations of these variables is exceedingly large, for all practical purposes, each disk carrying some finite amount of load has a unique stress state and hence a unique stress pattern.

Our objective is to find the magnitudes and directions of contact forces at every contact of each particle carrying a finite amount of load. In order to achieve this, we need to know several things:

- center of mass of each disk;
- number of contacts for each disk;
- locations of the contacts;
- greyscale or RGB image of stress patterns inside the disks.

We have seen the example of the last item in the above list in Figure 2.7. This is the image obtained by viewing the image through crossed polarizers. If we use white light and a color camera, we obtain a truecolor RGB image, whereas a monochrome light source or a monochrome camera would yield a greyscale image. The RGB images yield three times the information obtained from a greyscale image; on the other hand, a narrowband monochrome light source reduces errors due to wavelength spread, and yields precise fringes for a particular wavelength. We will make use of both kinds of images to study different problems, as our inverse problem solution method is general enough so that it can be modified suitably for both kinds of images.

The first task before finding the contact forces is obtaining the material fringe value, f_σ, which is the combination of constants in the phase of the $sin()$ function of equation 2.4. The details of obtaining this constant will be described in a later

section. Once f_σ is known, the algorithm for solving the photoelastic inverse problem for any particular disk in the sample can be put quite simply as follows:

- locate the center of the disk;
- find out the number of contacts and the x-y coordinates of those contacts;
- consider the stress pattern inside the disk as experimental data;
- fit observed stress pattern to the theoretical stress pattern given by equation 2.4, by keeping the contact force components as fitting parameters;
- treat the best fit parameter values as measured contact forces.

The process of solving the inverse problem can be split into two steps. The first step is to obtain the geometric information about the system, i.e. the disk centers, contact numbers and their locations. The second step is obtaining the contact forces by fitting the analytical model to the observed stress patterns. In what follows, we will take up each step separately and examine the methods involved in each step in detail.

2.3.1 Geometric image analysis: obtaining the particle centers and contacts information.

The center of mass information for objects of any shape within an image requires morphological operations to be performed on the image. The central idea is to confine the region of interest (ROI) within a boundary, eliminate the intensity variations within the ROI and assign a prescribed intensity value such that it is distinctly different from the background and unambiguously identifiable. This step usually results in binarization or thresholding of the image. There are several distinct strategies to obtain centers of dark/bright blobs in bright/dark background. One approach is

to continue the morphological image operations and perform a sequence of erosions and find the ultimate erosion point (UEP). Another approach is to perform moments analysis on the ROI with the first moment being the center of mass. In a different approach, the greyscale or a binary image is convoluted with a specified kernel to obtain the centers. In general finding circular areas and centers of circles is an easier task than most other shapes [Rus99, Gre83]

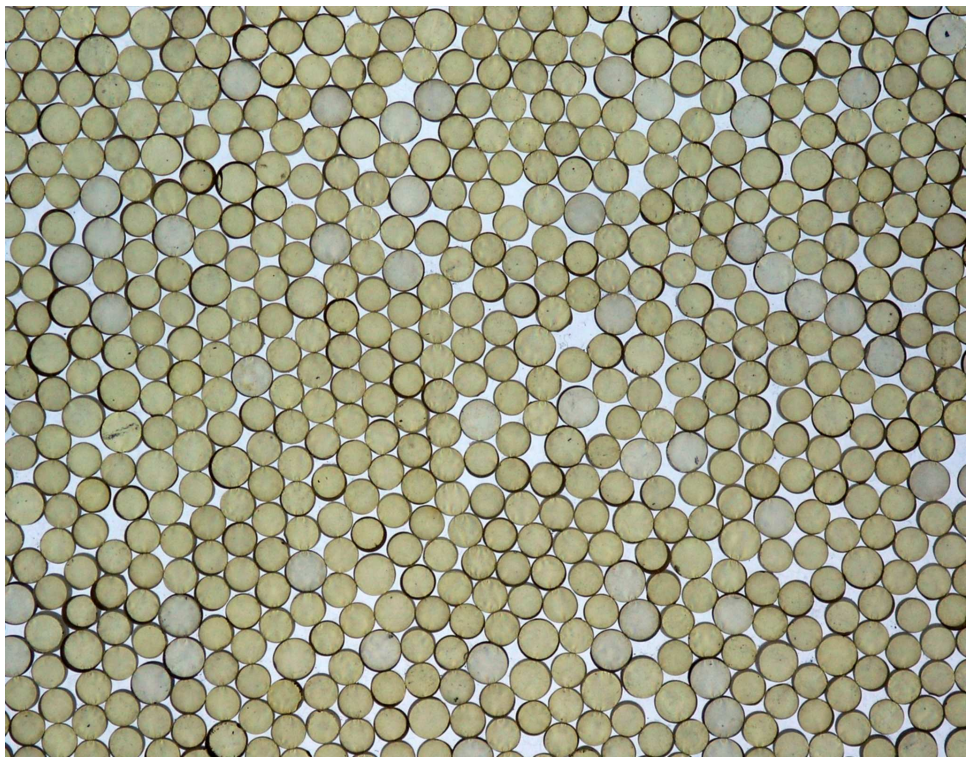

Figure 2.8: Unpolarized image to obtain disk centers and contacts.

An inspection of Figure 2.7 reveals that a simple minded strategy for finding centers of circles is unlikely to work for photoelastic images. The reason for this is the spatially periodic variations of intensities within each disk, which are different for each disk, and which hinder any attempt to apply global rules for finding circles and their centers. This problem is overcome by acquiring a separate image which captures only the particles without the stress patterns. This is accomplished by capturing the image without the analyzer. The resultant image is shown in Figure

2.8. This image is ideally suited to finding circular disks and their centers using any of the approaches mentioned above. We will predominantly use the erosion method which is computationally fast but requires some amount of manual input to improve the accuracy of the method. When a large data set is to be analyzed, the convolution method is more suitable, as it can be completely automated.

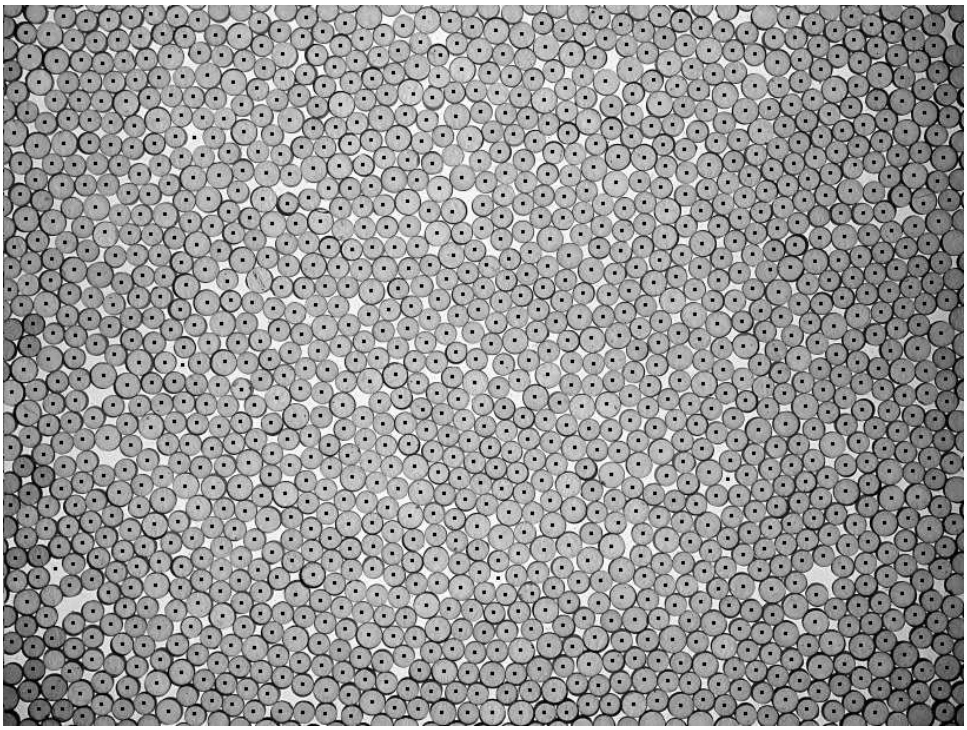

Figure 2.9: An unpolarized image of the disks with centers superimposed.

An example of the centers found by above erosion method is shown in Figure 2.9. The image size is 3264×2448. The erosion method is implemented using software written in C. It is also cross-checked with Matlab codes. Key steps involved in obtaining centers from an unpolarized image are as follows:

- A Sobel edge detector is used to find the edges of the disks.
- The edge-detected image is binarized using an appropriate intensity threshold, and reversed, which results in an image with bright blobs on a dark background.

- Multiple erosions are applied to separate the blobs completely from each other. This results in substantial reduction in the size of the blobs, and also a distortion of the circular shape.

- A few dilations are applied until the blobs grow, so as to become more rounded but still separated from each other.

- A labelling algorithm is applied, which finds the geometric mean of connected bright pixels.

The centers are found with a pixel-level, or even sub-pixel accuracy. The accuracy can be maintained at sub-pixel level by manually adjusting the image processing parameters like the threshold value and the number of erosion-dilation cycles, for a given run. The most important aspect of the process is removal of all the voids of different shapes and sizes. This is accomplished by calculating the form factor $f = L^2/4\pi A$ of the blobs, where L is the perimeter, and A is the area of the blob. For circular disks, the form factor is 1, whereas for non-circular objects it is greater than 1. Retaining objects with form factors close to 1 eliminates the voids which typically have much larger form factors. Although the form-factor criterion is quite accurate, occasionally a disk is missed, or a void is treated as a disk. These cases are corrected manually. Typically, only one or two such erroneous instances occur for an image with roughly 1300 disks.

The next step in our method involves finding particle contacts. Most traditional methods of finding nearest neighbors or contacts employ a euclidean distance criterion. The idea is to check center-to-center distances and consider two particles in contact if this distance is within a few percent of the sum of the radii. Ordinarily this approach would suffice, but for our system this simple approach falls short due to one extra requirement. We want to find not just the possible contacts but the true

force-transmitting contacts. In addition, for the inverse problem solution to work effectively and efficiently, we need a high accuracy in finding true contacts.

In view of this requirement, we implement a two step procedure for finding the true contacts. In the first step we obtain possible contacts by employing the euclidean distance criterion from the centers found as described above. In the second step we use the polarized stress image and examine the region around each possible contacts to determine if there is a transmission of force. This determination is done by looking at the intensity variations and the square of the gradient of intensity, $\nabla I^2_{x,y}$ in a small window around the contact. Typically, when a contact carries a load, it acts as a source point for fringes resulting in rapid variations in the intensity as compared to the rest of the disk or a contact carrying no force. This is due to the variation of stress near the contact. This allows us to identify a true contact based on a cutoff value of the gradients in intensity. If the square of the gradient of intensity is higher than a cutoff value, the contact is treated as a true contact. This procedure is quite accurate with errors around 2%. The error estimate is found by employing the criterion on various test images with manually determined contacts. The primary reason for the errors is the digital image noise and resolution limit.

The intensity gradient, $\nabla I^2_{x,y}$, calculated at each point in the image is a four-way (horizontal, vertical, and both diagonals) average of the intensity difference squared divided by the distance of a line segment joining the pixels:

$$\begin{aligned} \nabla I^2_{x,y} &= \frac{1}{4}\Big[(\frac{I_{x+1,y} - I_{x-1,y}}{2})^2 + (\frac{I_{x,y+1} - I_{x,y-1}}{2})^2 + \\ &\quad (\frac{I_{x+1,y+1} - I_{x-1,y-1}}{2\sqrt{2}})^2 + (\frac{I_{x+1,y-1} - I_{x-1,y+1}}{2\sqrt{2}})^2\Big] \end{aligned} \tag{2.18}$$

for a square pixel array with directions x and y. Each individual component of the gradient is squared to remove the directional dependence.

Finally, the average gradient squared of intensity (G^2) is found by averaging $\nabla I^2_{x,y}$

over the entire N pixels contained within the region of interest (ROI):

$$G^2 = \frac{1}{N} \sum_{x,y} \nabla I^2_{x,y}. \tag{2.19}$$

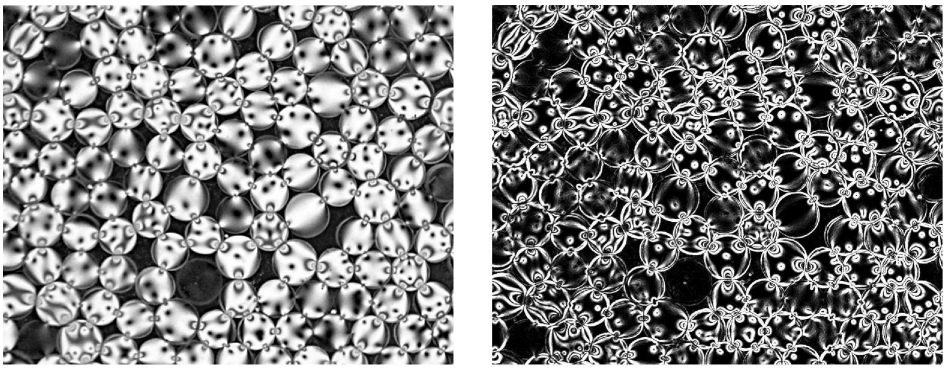

Figure 2.10: An example of an image (left) and its gradient square (right) as an image.

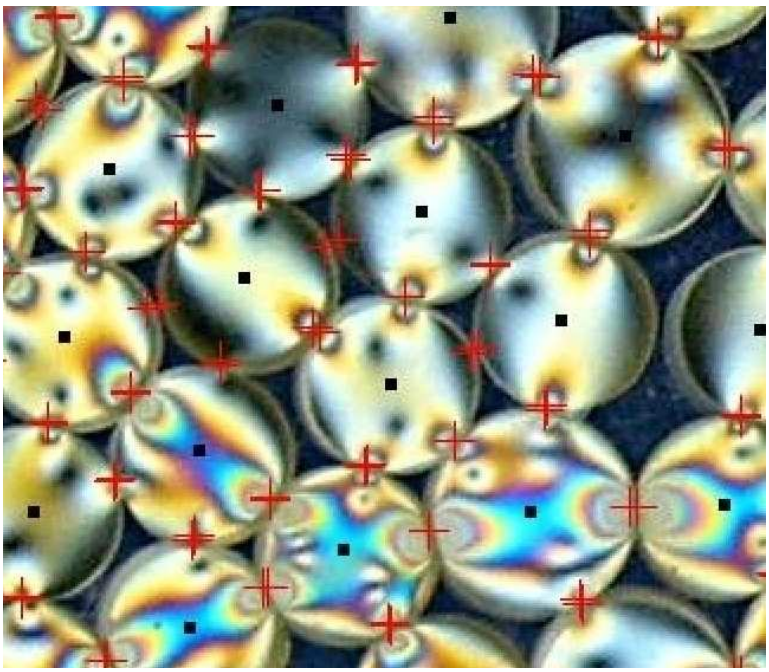

Figure 2.11: Image of the system with centers and contacts.

Figure 2.10 shows an example image (left) and the image constructed by finding the G^2 at every pixel (right). This pixelwise G^2 is then averaged over a suitable

window around the contact to obtain the average G^2 around a contact. The number of fringes increase as the contact force increases, resulting in a higher average G^2 as compared to any other area inside the disk. Figure 2.11 shows the stress image of the system with centers marked as black dots and contacts as red crosses. The average spatial error in finding the contact location is roughly two pixels.

The locations of the centers of the disks and the force-bearing contacts complete the geometric information required prior to the measurement of contact forces. The contact forces can now be found by utilizing the geometric information along with the stress pattern inside the disks and the plane elasticity solution.

2.4 Solving the inverse problem

At this stage of our analysis, we have the geometric information about the disks; the locations of the centers of the disks, the number of contacts each disk has, and their coordinates. Before we begin to implement the solution to the inverse problem, we need to find the relation between the optical response of the material with applied stress. This relation is a property of the material, and can be quantified by a single constant; the fringe value, f_σ, which is defined by combining all the constants in the phase of equation 2.4, and is given by:

$$f_\sigma = \frac{\lambda}{Ct} \tag{2.20}$$

Although it can be found by knowing all the constants exactly, in practice, for a given material of specific thickness, observed under white light, it is found by applying various loads to the sample, and measuring the fringe number at specific locations. For disks, the procedure is somewhat simplified, and rather accurate, since the relation between the material fringe value, diametrically applied loads, and the

fringe number at the center of the disk is very simple. It is given by:

$$f_\sigma = \frac{4F}{\pi DN} \tag{2.21}$$

where, F is the applied load, N is the fringe number at the center and D is the diameter of the disk.

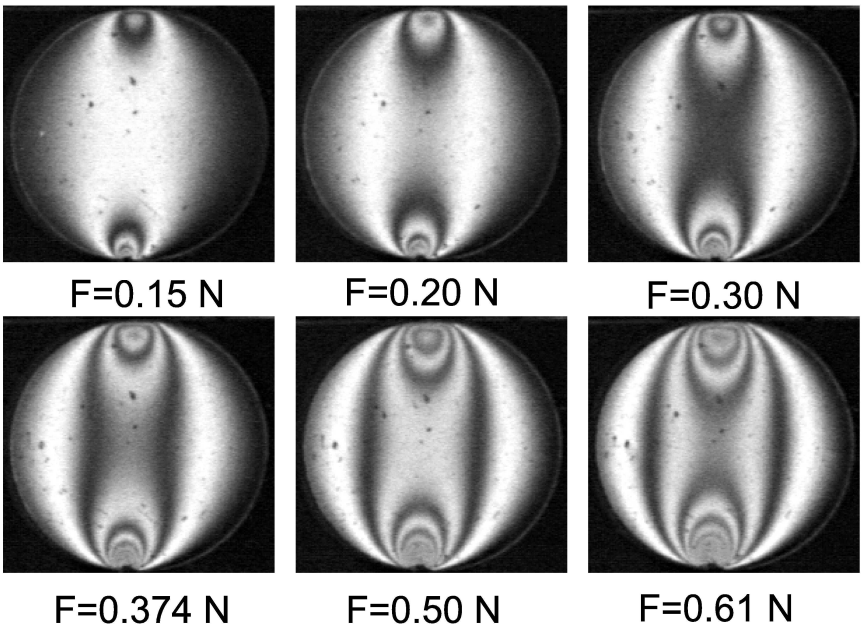

Figure 2.12: A sequence of experimental images of diametrically loaded disks for calibration.

Figure 2.12 shows a sequence of images of diametrically loaded disks with increasing loads. It can be seen that the number of bands or fringes in the disks increase as the load increases. The fringes are contours of constant shear stress, and can be numbered systematically, signifying increase of shear stress as we trace a path from the edge of the disk towards the contact locations. The center of the disk is a saddle point, where fringes originating from the two opposite contact points meet. The fringe number is zero at the boundary and then increases by one half integer for every bright and dark band crossing. Thus the first bright band from the circumference has the fringe number 0.5, the next dark band, 1.0 and so on.

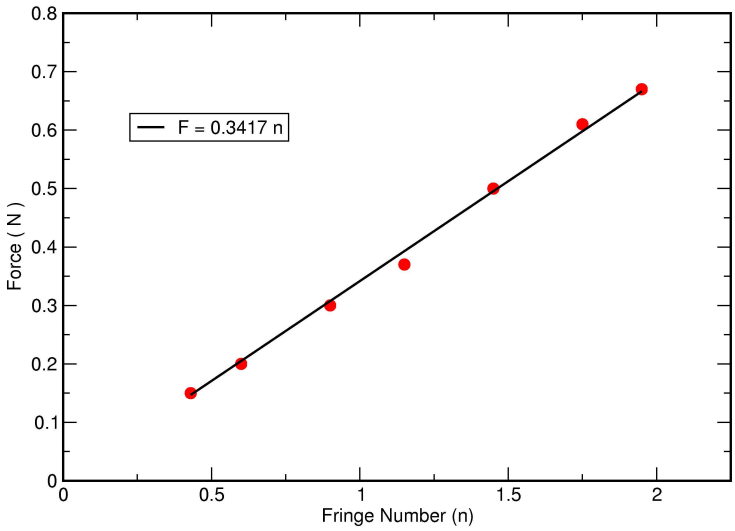

Figure 2.13: Calibration curve for force and fringe number.

Figure 2.13 shows the calibration curve for applied load (F) versus the fringe number (N) at the center of the disk. The applied load is measured with a digital force gauge (IMADA DPS-1) with a resolution of 0.001 N. The slope of the straight line fit to this curve can be used to find the fringe value f_σ, from equation 2.21. The disks used in our experiments are made from a polymer (PS-4, Vishay Inc.); the Young's modulus of the disks is 4 MPa, diameter is around 0.8 cm, and the thickness is around 0.5 cm. For this material, the fringe value comes out to be about 58. Once the material fringe value is known, the analysis for finding contact forces from individual images can begin.

The basic idea in solving the inverse problem is to use equation 2.4, which is rewritten below in terms of f_σ.

$$I(x,y) = I_0 \sin^2[\frac{(\sigma_1 - \sigma_2)\pi}{f_\sigma}] \tag{2.22}$$

The left side of the equation is the observed intensity at a pixel coordinate x and y. The right hand side of the equation has two contributions; one is the known fringe value f_σ, and the other is the principal stress difference $\sigma_1 - \sigma_2$, at the physical coordinate x and y of the disk. The pattern of intensity variation reflects the variation of $\sigma_1 - \sigma_2$ as a function of spatial coordinates. Our procedure for extracting contact forces relies on substituting an analytical expression for $\sigma_1 - \sigma_2$. If we can manage to do that, then we can cast the problem as a non-linear fitting problem between observed intensities and theoretical intensities.

We have derived an exact analytic expression for the stress components for general case of N point contact loads of arbitrary magnitudes and in arbitrary directions, obeying force and torque balance, and acting on the circumference of a disk. The full solution is given in the Appendix. From these stress components, the eigenvalues of the stress tensor can be computed, and hence the difference in the eigenvalues, which is the principal stress difference $\sigma_1 - \sigma_2$. The observed intensities are sin^2 of the principal stress difference, which makes the response highly nonlinear and periodic.

2.4.1 Algorithm for solving the inverse problem

To begin with, we will first consider the single disk problem. Figure 2.14 shows a disk acted upon by a number of forces. Using the plane elasticity theory, we can obtain the individual stress components σ_{xx}, σ_{yy}, and σ_{xy} in terms of the contact forces. For a two dimensional disk, the complete stress tensor is given by:

$$\sigma = \begin{pmatrix} \sigma_{xx} & \sigma_{xz} \\ \sigma_{zx} & \sigma_{zz} \end{pmatrix}. \tag{2.23}$$

The eigenvalues or the principal stresses σ_1, and σ_2 of the stress tensor are given

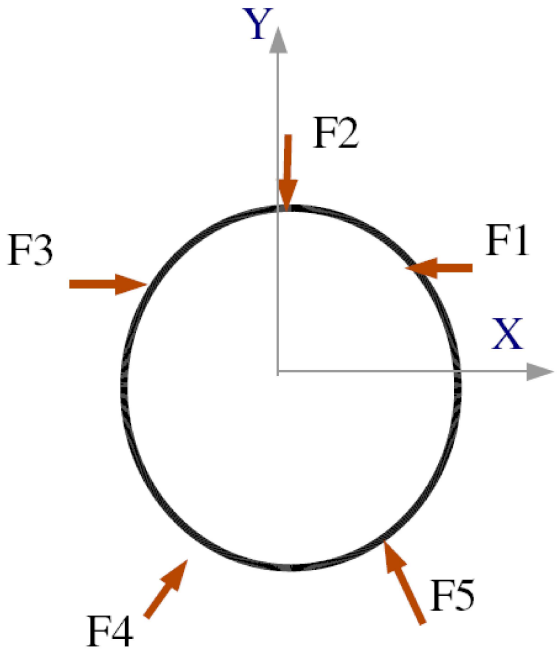

Figure 2.14: Schematic diagram of forces acting on a disk.

by:

$$\sigma_{1,2} = \frac{-(\sigma_{xx} - \sigma_{yy}) \pm \sqrt{(\sigma_{xx} - \sigma_{yy})^2 + 4\sigma_{xy}^2}}{2} \tag{2.24}$$

The principal stress difference is given by:

$$\sigma_1 - \sigma_2 = \sqrt{(\sigma_{xx} - \sigma_{yy})^2 + 4\sigma_{xy}^2} \tag{2.25}$$

The above expression for the principal stress difference is a function of contact force components which we need to extract. The way in which we implement the algorithm for extracting these forces can best be understood with the help of a few examples.

Consider, for a single disk, the simplest possible situation of two equal and opposite forces acting on the boundary of the disk as shown in Figure 2.15. We begin by finding the center of the disk, marked in the image as x. The locations of the contacts can also easily be found in from the image. The black circle in the image

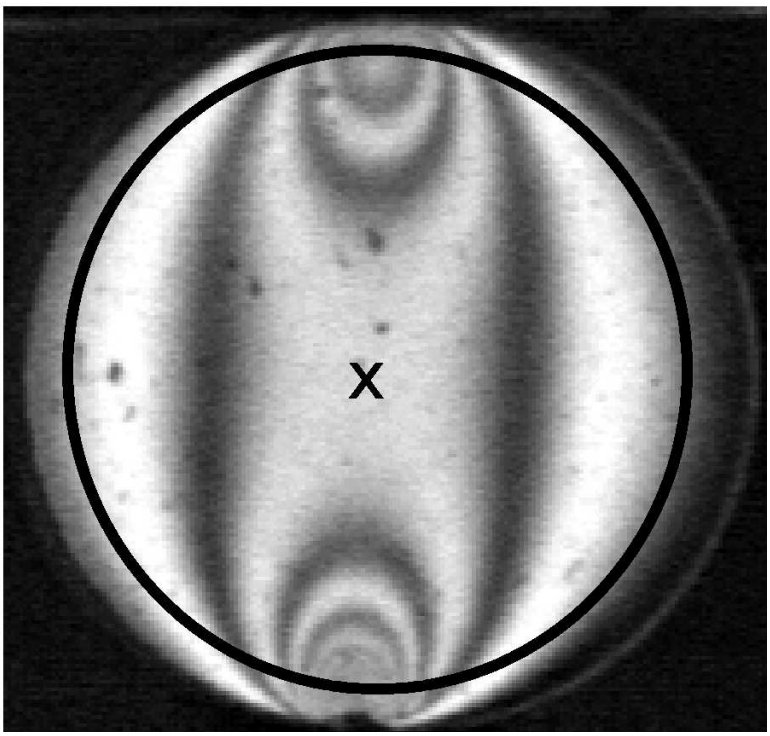

Figure 2.15: Diametrical forces acting on a disk: the center is marked as "x", and the area within the circular ring is used to obtain intensity data.

within the disk represents the region which we use as experimental data. The region used to get observed intensity is chosen carefully to avoid data points very close to the contact points. Very close to the contacts, the density of fringes increases very rapidly and produces data which is not very well resolved. In order to fit the model to the data, we need sufficient number of good data points, which we can obtain from the interior of the disk, while avoiding ill-resolved data near the contacts. In this way, as experimental data, we have a matrix of intensity values (I) at a given pixel location (i,j), in the image coordinate system. In order to set the fitting problem, we need to convert the pixel coordinates to physical coordinates with the axes centered at the center of the disk. This is accomplished by a simple linear transformation. Now we have, in physical coordinates of the disk, the following:

$$I(x,y)_{observed} = I_0 sin^2 \left[\frac{(\sqrt{(\sigma_{xx} - \sigma_{yy})^2 + 4\sigma_{xy}^2})\pi}{f_\sigma} \right] \tag{2.26}$$

This is the equation we will use to extract the contact forces. On the left side of the equation, we have experimental intensities at various locations within the disk. On the right side, we have the theoretical values of intensities at these locations depending on the external forces. Our goal is to find the external forces which result in theoretical intensities closest to the observed intensities at all of the data points under consideration.

This goal is best achieved by performing a nonlinear least-squares fit between the observed intensities, and the theoretical solution, keeping the external forces as free parameters. The fitting procedure, when finished should yield us the contact forces as best-fit parameter values. The algorithm used for performing the nonlinear least-squares fit is due to Levenberg & Marquardt [PFTV92]. We implement a two dimensional nonlinear fitting procedure.

The Levenberg-Marquardt algorithm starts with the user supplied data for the intensities at various locations of the disk, the coordinates of those points, the analytic expressions for the theoretical intensities, and the derivatives of this analytic expression with respect to the fitting parameters. Given this basic information, and initial guesses for the fitting parameters, the algorithm begins computing the least-square error between the observed values and the computed values. It then increments the initial guesses by a small amount and recomputes the least-square error. If the error increases, the values of the parameters are reduced by a small amount. If the error decreases, the new parameter values replace the initial guesses. The process can be repeated until the change in the error is less than a predetermined small amount. In this way, the algorithm settles on the final values of the fitting parameters, which

are taken as the measured contact forces. This is a barebones sketch of the algorithm, which in practice has many subtleties, like any numerical analysis of nonlinear problems. The details can be found in [PFTV92].

A peculiar feature of any nonlinear fitting procedure is the dependence on initial guesses of the fitting parameters. This dependence on initial values is problematic even in one dimension. In two spatial dimensions, the problem is even more compounded. Borrowing the language of energy minimization problems, our fitting procedure is equivalent to finding the global minimum of a complicated two-dimensional energy landscape. If one starts with initial guesses of parameters which are very close to the correct values, the convergence is rapid and usually accurate. On the other hand, a different set of initial guesses may converge rapidly but only onto a local minimum. Convergence onto a global minimum is not guaranteed. In view of this, we augment our fitting procedure to find the best-fit parameters by large number of initial guesses of parameter values within a certain range. We then compare the final least-square errors of these converged solutions, and select the best-fit parameter set with the minimum error. This step further improves the accuracy of the method.

In practice, the range of initial guesses we supply is based on the following observation. Each contact force on a disk has magnitude and direction. The magnitude of the contact force can be guessed reasonably accurately by using prior calibration. The calibration tells us what the intensity pattern looks like around the contact, when a force of certain magnitude is applied. What this calibration does not tell us is the direction in which this force acts. The job of the nonlinear fitting procedure is to give us not only a more accurate measure of the magnitude of the force but also its direction. In order to obtain this direction precisely and unambiguously, we supply a range of initial guesses with the same magnitude but different directions, implement the fit, obtain the best-fit parameter values for each set of initial guesses, and select

the set with the lowest error. In most cases, this procedure produces an accurate estimation of both the magnitudes and directions of the contact forces acting on the disk.

A second area of concern for nonlinear fits in general is the number of fitting parameters. The overall convergence properties of the fitting procedure depend on the number of parameters to be fitted; more parameters require more representative data points. This in turn affects the computational effort. In our case we can reduce the number of fitting parameters by enforcing force balance and torque balance; a fundamental requirement for frictional particles to be in static equilibrium. Thus, for N contact forces, we have 2N unknown force components that we need to determine. Since the disk is in static equilibrium, all the 2N parameters are not independent. The force balance condition on X and Y components of forces produces two constraints:

$$\sum_{i=1}^{N} F_{ix} = 0 \tag{2.27}$$

$$\sum_{j=1}^{N} F_{jy} = 0 \tag{2.28}$$

$$\tag{2.29}$$

where F_{ix}, and F_{jy} are the X and Y components of contact forces.

The torque balance produces one more constraint.

$$\sum_{i=1}^{N} \vec{R_i} \times \vec{F_i} = 0 \tag{2.30}$$

where, R_i is the radius vector between the center of the disk and i-th contact, and F_i is the force at the contact. $\times$ is the vector product.

In the end we have 3 constraints on our 2N free parameters, which reduce the number of free parameters to 2N-3. This is of substantial help in reducing com-

Image	Experimental Force (N)	Best-Fit force (N)	Error (%)
1	0.149 ± 0.001	0.146	0.3
2	0.198 ± 0.001	0.200	0.2
3	0.298 ± 0.001	0.299	0.1
4	0.372 ± 0.001	0.376	0.4

Table 2.1: A table of experimental and computed values of forces

putational time and improve the efficiency of the algorithm. In addition, it is also physically meaningful, since any best-fit force components are necessarily force and torque balanced.

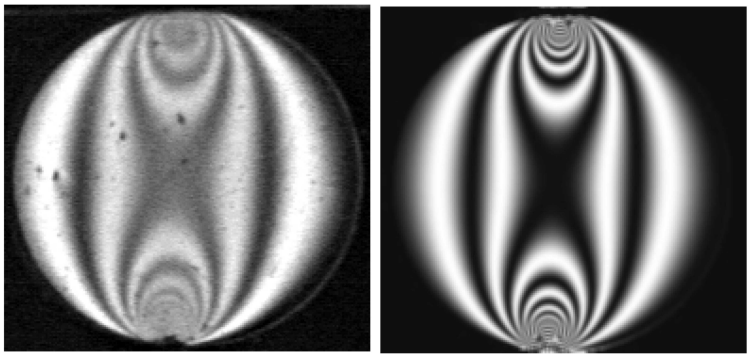

Figure 2.16: Experimental image of a diametrically loaded disk (left), and the best-fit image obtained after obtaining the contact forces (right).

Once the contact forces are obtained, we can use the theoretical model to visualize the response of the disk to the contact forces by computing the intensities using the best-fit force values. It gives an easily verifiable visual check as to the reasonableness of the measured force values. Figure 2.16 shows an example of an experimental image and the best-fit image generated from the best-fit force values.

Figure 2.17 shows such numerically generated best-fit images constructed from the best-fit contact forces of the diametrically loaded disks used to obtain the fringe value f_σ. These images are in the same sequence as in Figure 2.12. The similarity between the observed and best-fit images is readily apparent. Table 2.1 shows the values of the applied force and those obtained from solving the inverse problem in

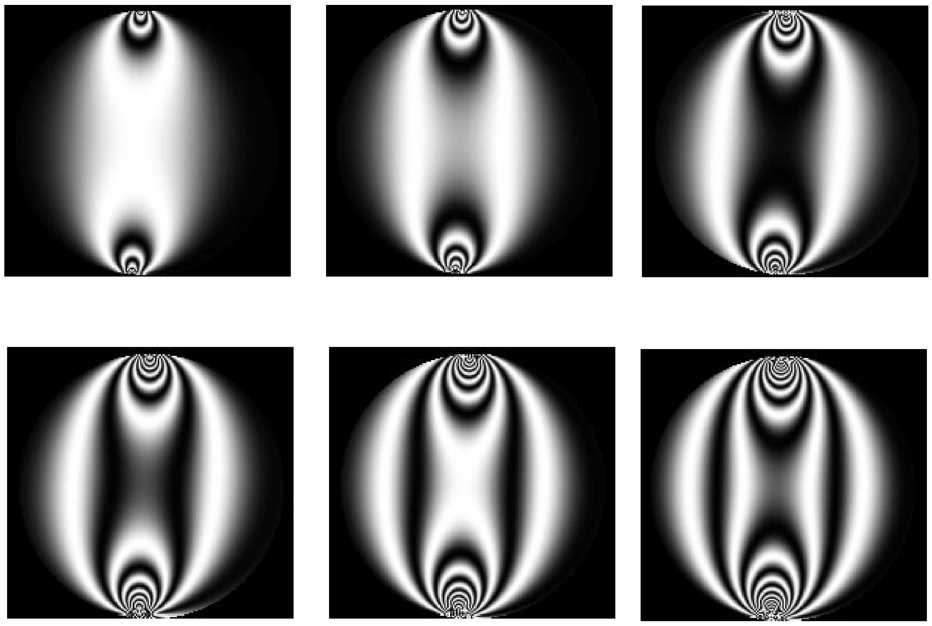

Figure 2.17: Best-fit images of the calibration images shown in Figure 2.12.

each case. The errors are very small in these simple two-contact cases primarily due to the fact that after imposing force and torque balance, we are left with only one free parameter.

The main idea to be grasped from Figure 2.16 and Figure 2.17 is that the method proposed here works rather well in extracting contact forces from experimental stress images. The examples presented so far should be considered as "proof of principle" type of evidence.

We now examine how well the method works when there are more than two contact forces acting on the disk. Essentially the procedure is exactly the same except for the fact that there are more free parameters now.

Figure 2.18 shows a comparison between the experimental image with three loads applied to a disk, and the best-fit image generated after finding the contact forces. The agreement between the observed photoelastic response and the theoretical response is again evident. The contact at the bottom the image was loaded with a

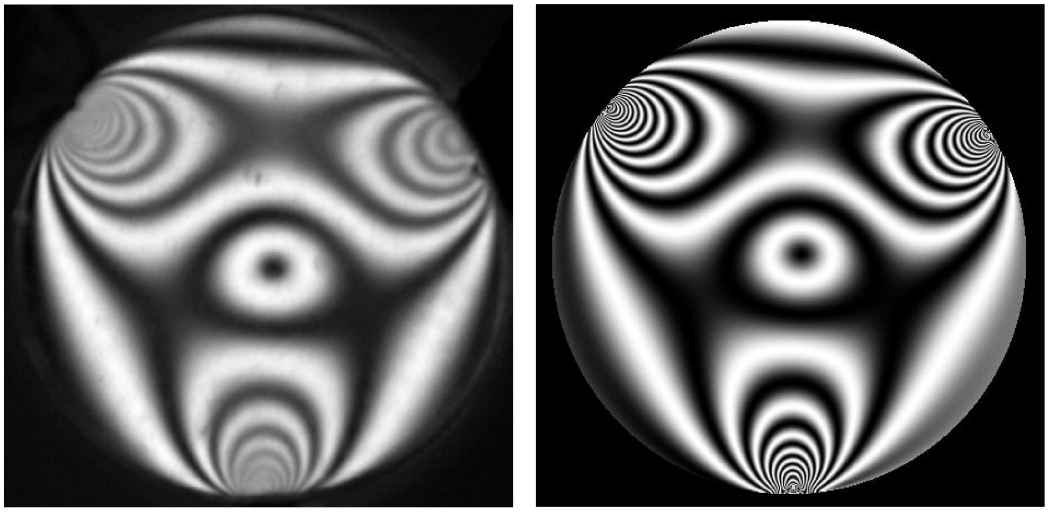

Figure 2.18: Experimental image of a disk with three contacts (left) and the best-fit image (right).

force gauge, which gave an independent measure of the force. The applied load was 0.663 N and the force obtained after the fitting procedure was 0.685, which is an error of roughly 3%. This is expected since the large forces have resulted in high fringe density, which has not been well-resolved at the contacts.

2.4.2 An array of disks: multi-contact, multi-particle problem

The next significant test of our procedure for contact force measurements is for the case of an array of disks under some arbitrary boundary load. The contact locations, as well as the normal and tangential forces developed between the particles are somewhat random, or at the very least, not carefully controlled. In this situation, we can truly test both aspects of our method; accuracy with which we can obtain the centers, and contact locations in an automated fashion, and the accuracy in the normal and the tangential components of the contact forces.

Figure 2.19 (left) shows a small collection of disks confined in a rectangular enclosure, with a force applied on the disk at center of the bottom boundary. The

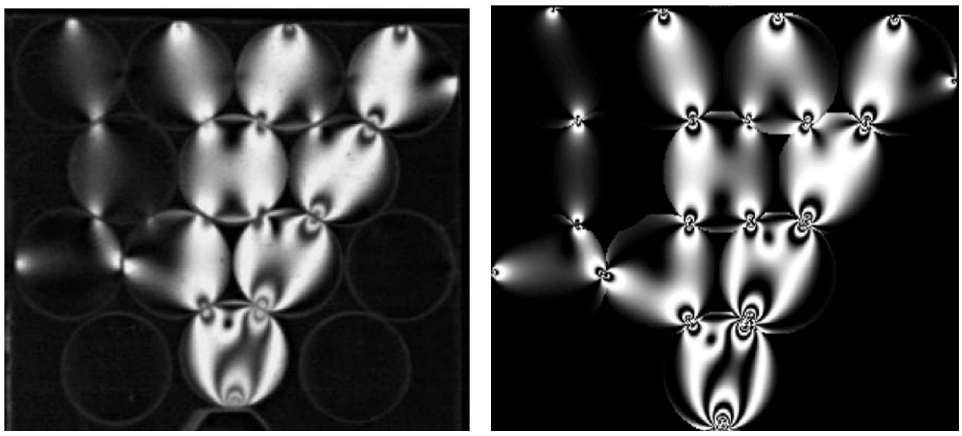

Figure 2.19: Experimental image of an array of disks (left), and the best-fit image obtained after obtaining the contact forces (right).

applied force is measured with a force gauge. The centers of the disks and contact locations are found by methods described in earlier sections. Each disk is treated as an independent object, and solved for separately. Thus, we start with the disk at the bottom boundary, and find the normal, and the tangential contact forces for that disk. We know the value of one of the contact force magnitude since it is measured with the force gauge. We can compare the value of the force measured via the force gauge and the one obtained by solving the inverse problem, giving us an estimate of the error at that contact, which is roughly 1.2%. Each disk is solved for subsequently, starting with the contacting neighbours of the first disk. This allows us to supply the forces found for the first disk as initial guesses for contact forces of the other disks. Once all the contact forces have been found, the best-fit image is computed.

Figure 2.19 shows the best-fit image computed after all the disks have been solved for. The fit again appears good, although not as good as in Figure 2.17, or in Figure 2.18. This is because in order to capture more disks, the resolution per disk has to be lowered.

In most situations of interest, we will not have a measure of the force on one or more boundary particles. For these cases, it is highly desirable to have an estimate

of the errors in the best-fit force values which is in some sense an internal measure. One internal measure of errors in fitting is the usual χ^2, or the least-square error. This measure pertains only to the fitting algorithm; how well the observed, and the theoretical values match for the data points chosen to be used for solving the inverse problem. In order to have a more physical measure of the errors in force measurements, we employ the following procedure.

As mentioned earlier, our procedure treats each disk separately, and solves for the contact forces on one disk at a time. The only constraint we have is that the forces and torques be balanced *for that particular disk*. This still laves one more constraint on the entire array of disks, viz. Newton's third law. The forces between the disks have to be equal and opposite. We *do not* impose the third law on our system. Instead we use the third law as a measure for the errors in the contact force measurements. Since a contact is shared between two disks, we get two values for the normal and the tangential component of the force at that contact. Ideally, they should be equal and opposite, but in practice they are somewhat different. We calculate the difference between the values obtained for the normal, and the tangential component and also the total magnitude of the force. We use these differences to estimate the errors in contact force measurements for disks in the bulk sample.

Using this procedure, we find that the average error in the magnitude of contact forces are small (≤ 5 %) for forces between 0.15 N and 1.5 N, but they are relatively higher (5-10 %) for forces lower than 0.15 N and higher than 1.5 N. The reasons for higher errors at both the very low, and very high end are different. At the low end of forces, there is very little intensity variation data to make a precise measurement of forces. At the high end, we have two limitations; one is the resolution of the imaging device itself, and the other is the sensitivity of the material itself, which is dictated by the stress-optic coefficient. Force measurements with the lowest errors are obtained

when the fringes are well-resolved, which happens in the above mentioned range of 0.15 N - 1.5 N. In most of our experiments, the loads on any given disk are always lower than 1.5 N, and the average force in most cases is around 0.4 - 0.6 N.

From all of the above data and discussion, a few important conclusions can be drawn. The method proposed in this thesis to extract vector contact forces is successfull. The method not only yields the magnitudes of contact forces but also the directions. In other words, we can obtain not only the normal forces, but also the tangential forces acting on the disk at each contact. The inverse method is effective even if the boundary forces are not known. The errors in the measurements are small for most of the force-range of interest to us.

We can now begin our systematic study of granular systems under different loading conditions, like isotropic compression, pure shear, simple shear etc., with the help of grain-scale contact force measurements; such an approach was feasible only via numerical simulations so far. The grain-scale contact force measurements can be used to gain a deeper understanding of the bulk response of the system. We will investigate these issues in the subsequent chapters.

Chapter 3

Response of granular systems to compression and pure shear

We begin, starting with this chapter, to apply our method of measuring grain-scale normal and tangential contact forces to granular systems under different conditions. Our objective is to study the behavior of granular systems under different loads in terms of the contact force distributions, the spatial structure of force-chains, and the geometry of contact networks. We would like to ascertain if there are any significant differences in the response of the system to different loads like pure shear and isotropic compression, and find ways to quantify these differences.

3.1 Introduction

A fundamental goal of granular mechanics is to understand the inhomogeneous distribution of interparticle forces manifested qualitatively as filamentary force chains, and their spatial correlations, specifically in response to forces at the boundaries [GHL$^+$01, RC01]. Achieving this goal is of central importance in civil engineering, geophysics, and physics [JNB96a, BJ97, Ned92] for understanding challenging problems like jamming, shear induced yielding and mechanical response. Here, we present novel experimental data for both normal and tangential grain-scale forces inside a two-dimensional system of photoelastic disks subjected to pure shear and isotropic compression. Various statistical measures show the underlying differences in these two stress states. These differences appear in the distributions of normal forces (more rounded for compression than shear) although not in the distributions of tangential forces (exponential in both cases). Sheared systems show anisotropy in distributions

of both the contact network and the contact forces. Anisotropy also occurs in the spatial correlations of forces, which provide a quantitative replacement for the idea of force chains. Sheared systems have long-range correlations in the direction of force chains. Isotropically compressed systems have short-range correlations regardless of the direction.

Under the action of external stresses, grains in dry granular materials form an inhomogeneous contact network, which carries most of the external load via force chains. The resultant network is different for shearing than for isotropic compression and is history-dependent due to friction. Previous experiments [MJN98, TVCR98, LMF99] have reported an exponential tail for the distribution of contact force magnitudes. This tail can be successfully predicted by many models [GG03, SvHSvS03] with radically different mathematical structures and microscopic assumptions. Testing the validity of these models requires that the predicted force distributions be verified by measurements of full vectorial contact forces in the bulk of the sample. It is also important to find other distinguishing signatures characterizing the nature of force chain networks under different boundary conditions, an important goal of the present work.

In the following experiments, we visualize internal stresses in each grain and by solving the full inverse photoelastic problem [Fro41] for each disk, we obtain normal and tangential force components for each contact between disks. We use this microscopic contact force information to investigate differences in the distributions of contact forces, and the force chain structure, arising from two different types of loads: pure shear and isotropic compression. We find that forces have distinctive angular distributions and spatial correlations depending on the macroscopic preparation. In particular, forces have long-range correlations in the direction of force chains for sheared systems, but are correlated over a much shorter range, regardless of direction

for isotropically compressed systems.

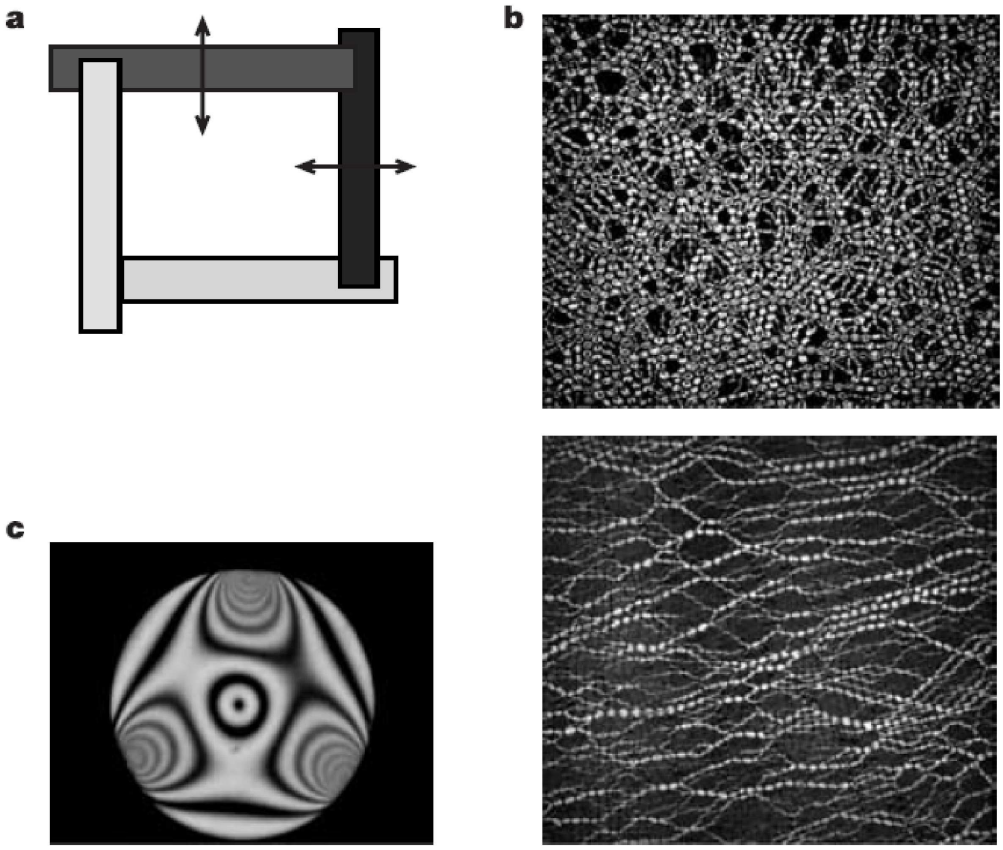

Figure 3.1: a: Biaxial test apparatus, b: (top) Isotropically compressed system, (bottom) sheared system, c: Single disk pattern.

3.2 Experimental system and methods

Our experimental system is a two-dimensional (2D) array of approximately 2500 bidisperse photoelastic (birefringent under strain) disks subjected to pure shear and isotropic compression. Figure 3.1a shows the schematic diagram of the biaxial test cell. The biaxial test apparatus rests horizontally on a sheet of Plexiglas and is used to impart pure shear and isotropic compression. Motorized linear slides move two walls of the biaxial cell precisely and independently with a velocity of .024 cm/s.

The system is illuminated from below and a high-resolution camera captures digital images from above. Each image captures roughly 250 particles located around the center of the cell, roughly 10% of the total number of particles. The system is imaged through crossed circular polarizers.

For each type of load, incremental deformations are applied in a quasi-static manner, beginning with a stress-free state. The sheared states are created by compressing in one direction and expanding by an equal amount in the other direction with strains ($\epsilon_{xx} = \epsilon_{yy} = |\delta L/L|$) ranging from 0 to 0.042. Isotropically compressed states are created by compressing in both directions with strains ranging from 0 to 0.016. The particles used in the experiment are either 0.8 cm or 0.9 cm in diameter and 0.6 cm in height with a Young's modulus of 4 MPa and friction coefficient 0.8. The number ratio of small to large disks is 4:1.

Figure 3.1b shows typical system size images for isotropically compressed state (top) and sheared state (bottom). Figure 3.1c shows an example of the observed stress pattern for a single particle at the resolution 0.01 cm/pixel used in these studies.

Although previous approaches [DDJdJ72b, DW83, SN85, DX93] have obtained contact forces using photoelastic techniques, they were neither automated nor suitable for a large enough number of particles to generate statistical information. Measurements of contact forces in our method are performed in a completely automated fashion for all disks except those at the boundary of the image.

Our algorithm (Chapter 2) for extracting contact forces involves fitting the observed photoelastic pattern inside each disk to the plane elasticity solution [LL70b] for the stresses inside a disk, treating the force components as fitting parameters. In effect we solve the 2D isotropic elasticity equations for each disk assuming a perfect line contact between 3D cylinders. As long as the deformations are not too large, as is the case in our experiments, the 2D solution is a good approximation. As the experi-

mental image is a highly non-linear function of the contact forces with the possibility of multiple solutions, we perform a non-linear least-squares fit using about 500 data points for each disk. The best-fit parameter values are our measured contact forces.

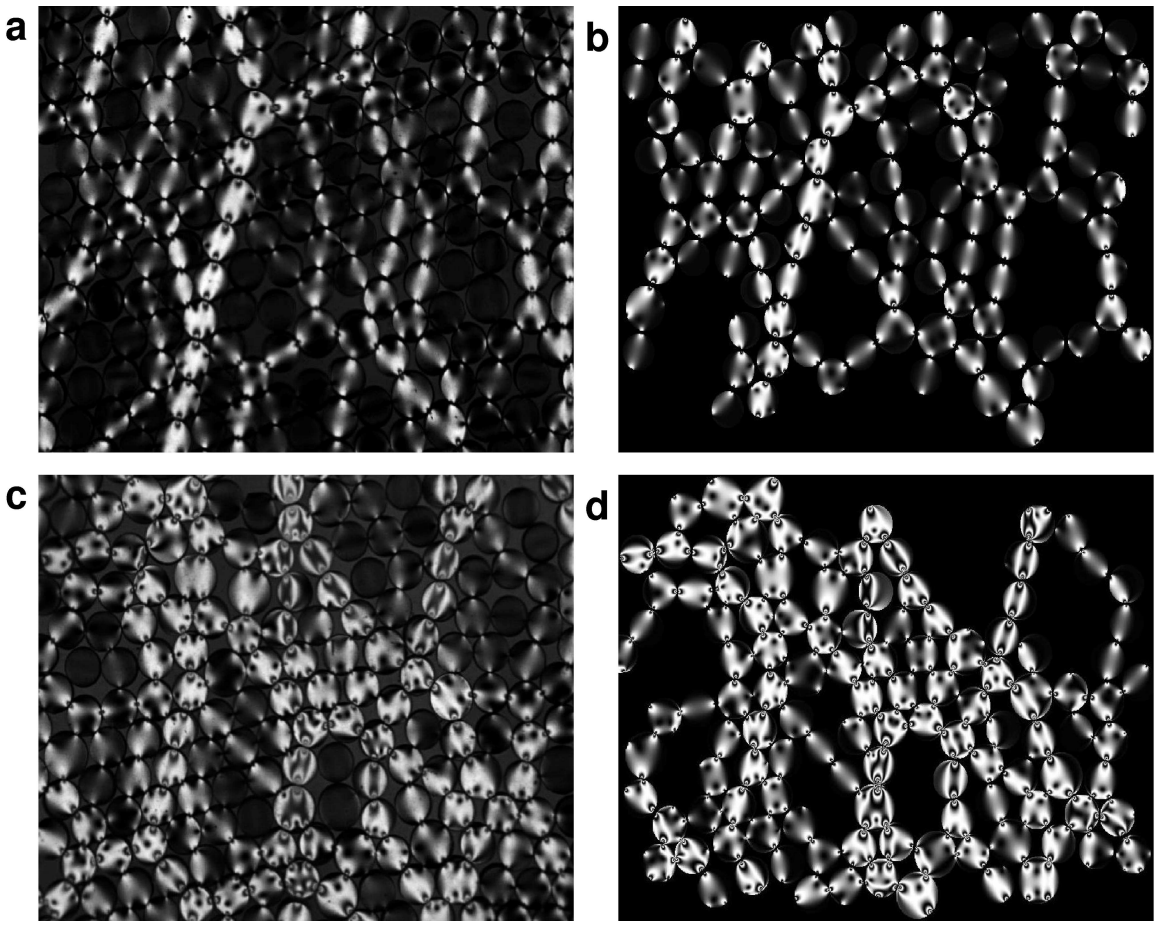

Figure 3.2: a,c : Experimental images, b,d: Best-fit images.

For each realization, we compare the image computed using the best-fit contact forces and the original experimental image. Figure 2 shows two such realizations. The computed images (Fig 2b, d) agree well with the experimental images (Fig. 2a, c) in terms of capturing the broad features of force chains. The error estimates found by calibration and by computing the average difference of pairs of forces at each contact are around 10 % for low forces and 5% for mean-to-high forces. The agreement between the observed stress field inside each disk and the computed stress

field validates the use of 2D approximation. The data presented below (Fig. 3, Fig. 4) is obtained from five realizations for each stress state. We use the contact forces obtained by the procedure outlined above to investigate the distributions of contact forces and the anisotropy induced by external loads.

3.3 Results

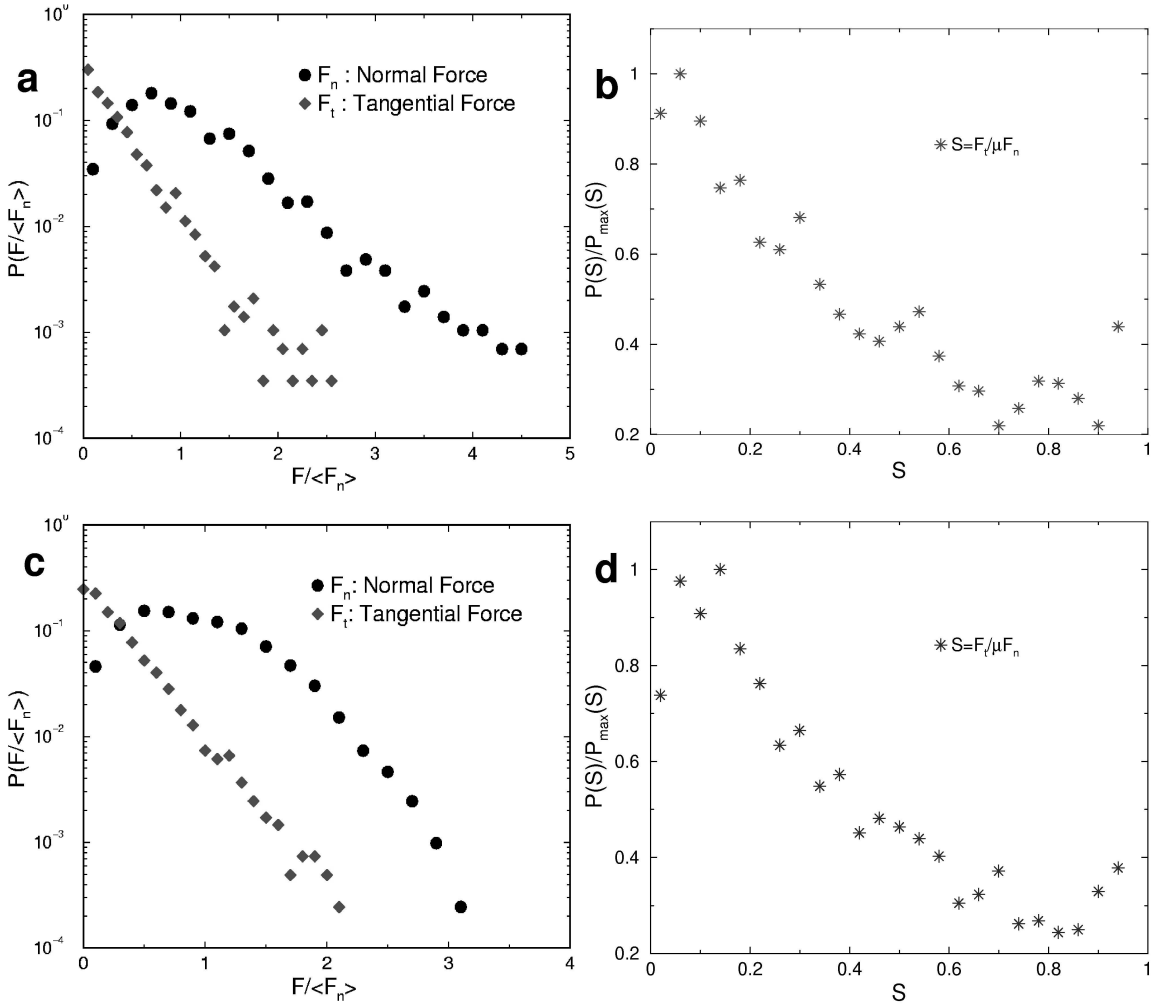

Figure 3.3: Distributions of the contact forces, and mobilized friction for sheared, and isotropically compressed systems. a) Probability distributions of the normal, and the tangential forces for sheared systems. b) Mobilized friction for sheared systems. c) Probability distributions of the normal and the tangential forces for isotropically compressed systems. d) Mobilized friction for isotropically compressed systems.

Figure 3.3 shows the distributions of the normal force, the tangential force and the ratio of tangential to normal force, for a sheared system and an isotropically compressed system. The deformation for isotropically compressed and sheared systems is 0.016 and 0.042 respectively. The normal and the tangential forces are normalized by the mean normal force, $< F_n >$. The mean normal force is around 0.25 N, and 0.4 N for sheared and isotropically compressed systems respectively. The normal force distribution for the sheared system (Figure 3.3a) has a peak around the mean, a roughly exponential tail and a dip towards zero for forces lower than the mean. In contrast, for isotropically compressed systems, the normal force distribution (Figure 3.3c) dips towards zero for forces below the mean, is broad around the mean, and decays faster for large forces compared to the sheared system. The tangential force distributions have a nearly exponential tail for forces larger than the mean for both the sheared (Figure 3.3a) and the isotropically compressed system (Figure 3.3c). The mean tangential forces are an order of magnitude smaller than the mean normal forces: a feature responsible for a smaller range of maximum tangential forces.

In order to investigate the role of friction in the system, we study the distribution of the variable $S =\mid F_t \mid /\mu F_n$, where μ is the static friction coefficient, F_t is the tangential force, and F_n is the normal force. The variable S gives information about how far away a contact is from the Coulomb failure criterion. If a contact is at the Coulomb failure criterion, S=1. Figure 3.3b and Figure 3.3d show the distributions of S for the sheared and the isotropically compressed system, respectively. For both types of loading conditions, the distribution of S shows that most of the contacts are much below the Coulomb failure condition. Numerical simulations of 3D granular systems in a silo geometry by Landry et al. [LGSP03] report similar results for the distributions of the normal forces and the tangential forces in sheared systems. The distributions of the mobilized friction in the interior of the system reported by

Silbert et al. [SGL02] are qualitatively similar to our results for the sheared systems. The similarity in the distributions of the mobilized friction for the sheared and the isotropically compressed systems could be due to the fact that our sheared system is well below the shear yield limit and that our distributions are obtained from regions far away from the walls.

Figure 3.4 shows the contact orientation, variation of the mean force and spatial correlations of forces for the sheared and isotropically compressed systems. The mean co-ordination numbers for the sheared system and the isotropically compressed system are 3.1 and 3.7, respectively. The deformations for each type of loads are the same as in Figure 3.3. Figure 3.4 a & b show the distribution of contact angles of contacts carrying forces larger than the mean, for the sheared and the isotropically compressed system, respectively.

Figure 3.4 c & d show the angular variation of the mean normal force, normalized by the maximum of the mean normal force, for the sheared and the isotropically compressed system, respectively. Starting from the center of the image, the image is divided into 24 angular bins of 15 degrees each and the average normal force in each bin is plotted against the mean value of that bin. The angle is measured with respect to the horizontal axis. The parameters of the fit in c are a=0.563, b=0.727 and $\theta_0 = 0.374$. The parameter a gives the mean force, b is a measure of anisotropy of the mean force and θ_0 gives the direction in which the mean force is maximum.

Figure 3.4e shows the spatial correlations of forces for the sheared system in the direction of force chains and perpendicular to it. Figure 3.4f shows the spatial correlations for the isotropically compressed system in the same two directions used for sheared system. The insets of e & f show the greyscale representations of the 2D correlations. The darker regions correspond to low correlation values and brighter regions to high correlation values. The computations are performed in Fourier space,

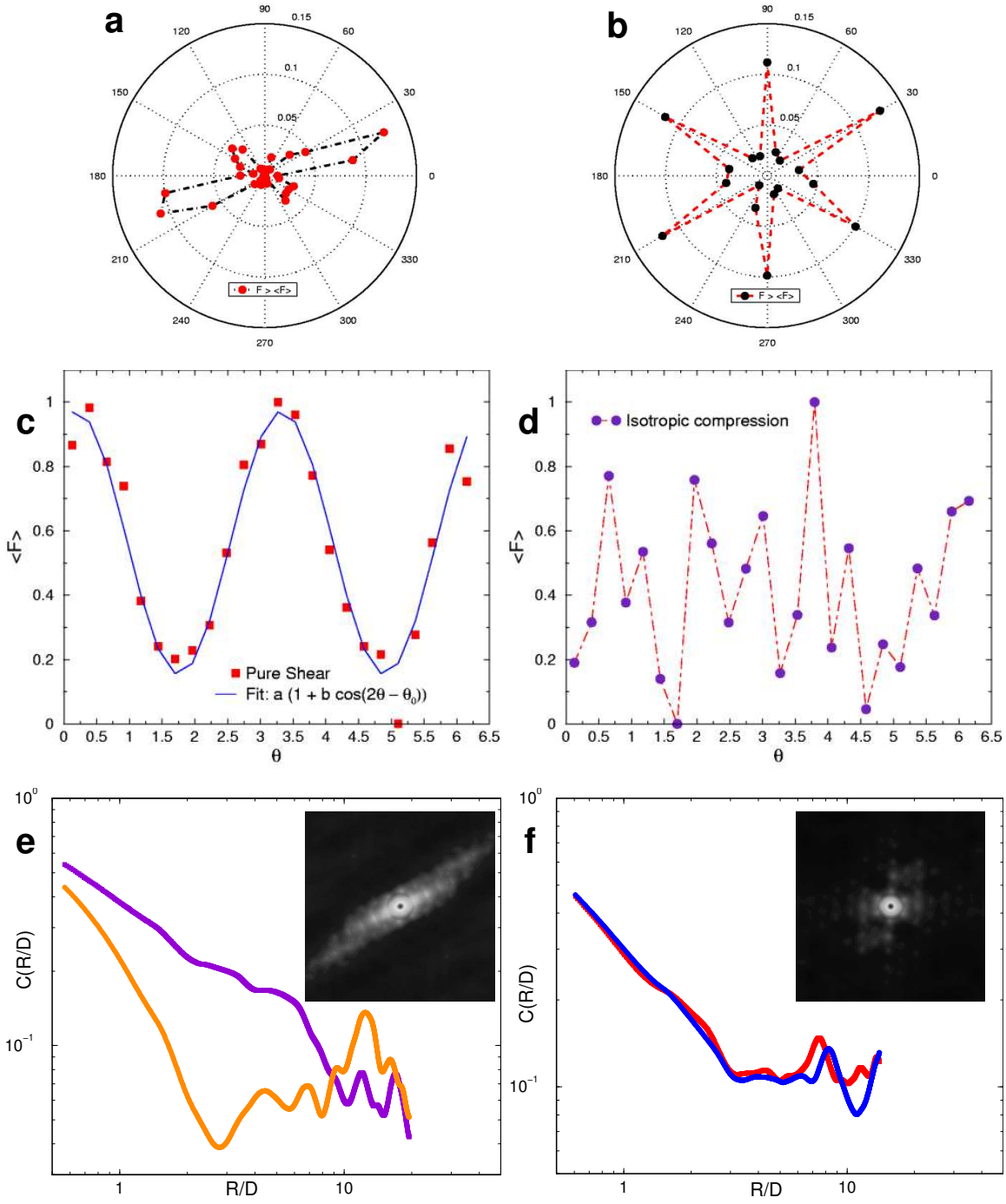

Figure 3.4: Contact orientation, variation of the mean force and spatial correlations for the sheared and isotropically compressed systems.

as the image sizes are large (1600x1152). The plots are on a log-log scale with distance R normalized by the average diameter D of the disks.

Our next focus of investigation is the shear induced anisotropy. The anisotropy induced by an external load has two distinct effects; one, a purely geometric effect, is to introduce anisotropy in the contact network, and the other, a mechanical effect, is to develop an anisotropic force chain network and alter the stress distribution in the system. In order to investigate the geometric anisotropy, we study the distribution of contact angles for contacts carrying forces larger than the mean force. The sheared system Figure 3.4a shows a strongly anisotropic distribution with a large number of contacts aligned along the direction of majority of force chains and a small number of contacts in the direction perpendicular to it. In contrast, the isotropically compressed system exhibits a distribution with a six-fold symmetry Figure 3.4b, indicating that the contacts are distributed evenly along these directions. A simple measure characterizing the mechanical anisotropy is the angular variation of the mean normal force as shown in Figure 3.4c and Figure 3.4d, for the sheared and the isotropically compressed system, respectively. For the sheared system, the mean normal force shows a periodic variation with peaks roughly in the direction of force chains. The variation can be adequately described by a second order Fourier expansion (Figure 3.4c), a result consistent with previous studies [BPC04]. In contrast, for the isotropically compressed system, the mean normal force is distributed randomly around an average value (Figure 3.4d).

A more quantitative characterization of the force chain structure can be obtained by computing the 2D spatial correlation function of the magnitude of the forces on the particles. Here, the idea is to provide a well-defined quantitative measure to replace the rather vaguely defined notion of a force chain. Specifically we computed $< \mathbf{F}(\mathbf{x})\mathbf{F}(\mathbf{x}+\mathbf{r}) >$, where $\mathbf{F}(\mathbf{x})$ is the sum of the magnitudes of the contact forces

on a particle, $\mathbf{x}$ gives the position vector of the point under consideration, and <> implies an average over $\mathbf{x}$. Because we want to study the variation of this correlation in different directions, we do not average over angles. Thus, the correlation function gives spatial correlation between forces separated by a distance r in different directions. Figure 4e and Figure 3.4f show the 2D correlation functions for the sheared system and the isotropically compressed system, respectively. The inset in each case shows greyscale representation of the 2D correlation functions. For the sheared system, the 2D correlation image (Figure 3.4e, inset) reveals that the force correlations are much larger and of much longer range in the direction of the long force chains. Figure 3.4e, which depicts the variation of correlation function with distance in the direction of, and perpendicular to, the force chains, indicates that the spatial correlation in the force chain direction persist for up to 15 particle diameters, whereas in the perpendicular direction they fall to background values within a couple of particle diameters. The correlation range in the direction of force chains is comparable to half the image size, which is 15 particle diameters in length. This length is also the Nyquist cut-off frequency of the Fourier method for computing the force correlation function in our computed images. The above data suggests the interesting possibility that the spatial force correlation may in fact be power-law type in the direction of long force chains for large system sizes.

In complete contrast to sheared systems, the isotropically compressed system has nearly uniform force correlation in all directions (Figure 3.4f, inset). This behavior is confirmed by examining the spatial correlation function in the same two directions used for the sheared case as shown in (Figure 3.4f). The correlation functions drop to background values in both directions after two particle diameters. Thus, no preferred direction is found in the isotropically compressed system, whereas in the sheared system the boundary stress creates an anisotropic stress state characterized

by long force chains aligned in a specific direction. Our results strongly indicate that sheared systems exhibit not only geometric but also mechanical anisotropy and that force correlations serve as an additional distinguishing signature characterizing stress induced anisotropy in granular systems. The rather long range of correlations in the force chain direction is important for understanding the approach to continuum behavior.

The observations reported here open up a completely new regime of comparison between theoretical models and experiments. One of the earliest computations of interparticle contact forces comes from the numerical experiments by Radjai et al. [RJMR96b], which are contact dynamics simulations of rigid, frictional particles under biaxial shear. Although the boundary conditions of the simulations and our experiments are not identical, these simulations seem to be the closest match to our experiments. Since our current experimental resolution does not allow us to measure very small forces, we restrict our comparison to forces higher than the mean. In qualitative agreement with our data for the sheared systems, the simulations obtain an exponential tail for forces larger than the mean for the distributions of both the normal and the tangential forces.

Two recent models, which study the force distributions in 2D systems of frictionless particles under isotropic compression and shear, are also relevant for the present data. A force ensemble approach by Snoeijer et al. [SVvHvS04] assumes equal a priori probability for all force networks consistent with force balance constraints on each particle. In this model, the distribution of the magnitude of the force has a peak around the mean force, finite P(f) at f = 0, and a tail decaying faster than an exponential for compressed systems. For sheared systems, the model has an exponential regime for normal forces up to three times larger than the mean (Snoeijer, J., private communication). A new lattice model [TSS$^+$05] considers triangular lattices

with force balance constraints on each node, which allows isotropic and anisotropic force chain networks. The lattice model prediction for the distribution of normal forces is an exponential tail for the sheared systems and a faster than exponential decay of the tail for compressed systems. The predictions of both models for sheared and isotropically compressed systems are in qualitative agreement with the present data. The absence of friction in both these models precludes a comparison of the distributions of tangential forces.

We have obtained experimentally, for the first time to our knowledge, the distributions of both the normal and the tangential components of contact forces, at the grain scale, in a bulk granular system. We find significant differences in the normal force distributions for sheared and isotropically compressed systems. We have demonstrated that the force distributions, the force correlations and the angular distributions are essential in capturing the anisotropy of force networks in systems subjected to shear and that force correlations could serve as an additional test for various models. Looking towards the future, we are now in a position to address a variety of important issues like the nature of jamming transition, and plasticity in sheared systems. These issues are vital for gaining a deeper understanding of the macroscopic behavior of granular systems from microscopic observations.

Chapter 4

Jamming in isotropically compressed systems

In this chapter we probe isotropically compressed systems further, but this time from the point of view of jamming. Starting from a loose system, we study when exactly the system jams and becomes mechanically stable, and what changes occur in the system at the point where it begins to jam. We study these issues with the help of a biaxial setup and measurement of contact forces.

4.1 Introduction

A solid – in contrast to a fluid – is characterized by mechanical stability that implies a finite resistance to shear deformation. It is well established that such stability can originate from long-range crystalline order that emerges at a fluid-crystal phase transition. On the other hand, there is no general agreement on the mechanism for how mechanical stability arises for a disordered solid. Disordered or amorphous materials encompass systems as diverse as molecular and colloidal glasses, gels, and granular packings. For granular systems, it is known that the elastic moduli of stable granular packings increase faster with pressure than expected from effective medium theories that take only the individual particle contact into account [God90]; thus collective effects play an important role close to the limit of mechanical stability [MGJS04, SRS$^+$05].

A particularly striking aspect of the limit of mechanical stability was discovered recently in computer simulations [SEG$^+$02, OLLN02, OSLN03]: For increasing density, the number of contacts per particle, $\langle Z \rangle$, increases discontinuously at the transition

point from zero to a finite number and continues to grow with the distance from the critical point as a power law. A power-law exponent of 1/2 was identified in these studies for both two-dimensional, and three-dimensional simulations without friction; a more recent simulation found a slightly higher exponent of 0.6 in three dimensions [DTS05]. The initial simulations[SEG$^+$02, OLLN02, OSLN03] also identified scaling laws for other quantities, such as the pressure P. In particular, P is expected to grow above the jamming transition as $(\phi - \phi_c)^\psi$, where $\psi = \alpha - 1$ in the simulations, and α is the exponent for the interparticle potential. Related discontinuous transitions followed by a square-root law are known from scattering experiments in glass-forming liquids [PBF$^+$91, YN96, ABT$^+$03].

To date, tests of jamming have been based on simulations. It is then crucial to apply experimental tests to these predictions. In the following, we present experimental data for coordination number (Z) and pressure (P) based on a method that yields an accurate determination of the transition point and identifies the power laws in Z and P for a two-dimensional experimental system. For frictionless disks, it is known that in the isostatic limit for the packing, when the number of constraints on each disk equals the number of unknown forces, the average Z equals 4. For frictional disks, because of one extra constraint of torque balance, the average Z is 3. Also known from simulations is the power-law growth in P with increasing packing fraction (ϕ). These are quantitative predictions, which we test here and find the jamming point for our system. By measuring both P and Z, we can also obtain a sharper value of the critical packing fraction, ϕ_c, for the onset of jamming.

4.2 Experimental setup and methods

Figure 4.1a shows a schematic of the apparatus. We use a bidisperse mixture of approximately 3000 polymer photoelastic (birefringent) disks with diameter 0.74 cm

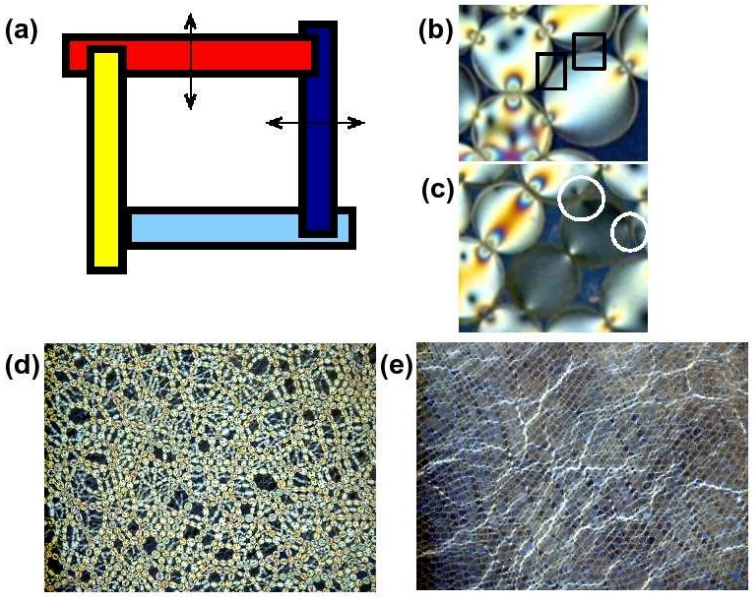

Figure 4.1: Schematic cross-section of biaxial cell experiment. Sample images of highly jammed/compressed and almost unjammed states.

or 0.86 cm. 20% of the disks are large and 80% are the smaller sized disks. This is the minimum possible number ratio which avoids crystallization. The disks have Young's modulus of 4 MPa, and a static coefficient of friction of 0.85. The model granular system is confined in a biaxial test cell which rests on a Plexiglas sheet [MB05]. The test cell is a rectangular enclosure 42 cm $\times$ 42 cm in size, with two movable walls, which are adjusted by stepper motors. The displacements of the walls can be controlled very precisely and the linear displacement step size used in this experiment is 0.004 cm; this is approximately .005D, where D is the average diameter of the disks. The setup is horizontal and placed between crossed circular polarizers and imaged from above with a high resolution (8 MP) CCD color camera. The camera captures roughly 1200 disks in the center of the cell. The disks, when viewed through crossed circular polarizers, enable us to visualize the stress field within each disk, as shown in Figure 4.1

The experimental procedure involves quasi-static compression or decompression

of the system. For compression, the system is initially in a stress-free state, and for decompression, the end state is a stress-free state. The results for both protocols are similar. In what follows we will show data mainly for decompression. Figure 4.1d shows the state of the system at the beginning of decompression phase; a highly stressed and jammed state. Figure 4.1e shows the state of the system towards the end of decompression phase when the system is almost unjammed and has very small amount of stress.

The procedure for data taking from an initially compressed state begins by compressing the system by 1.6 % from an originally stress-free state. We decompress the system by simultaneously moving the two walls outwards by a uniform steps of 0.004 cm. After each step, tapping is applied to relax stress in the system. Two images are captured at each decompression state; one with polarizer and one without. The image with polarizers gives stress information and the one without polarizers is used to locate disk centers using standard image processing methods. This quasi-static step-wise decompression is continued until the system is stress-free.

An important issue is the determination of contacts. Previous studies have mainly used the particle overlap criterion to determine contacts. In numerical studies, overlap beyond a threshold value also signifies transmission of force through the contact. In contrast, in experimental systems, finding correct contacts based on overlap or euclidean distance criterion is susceptible to larger errors due to contributions from false positive (Figure 4.1b, black square) as well as false negative (Figure 4.1c, white circle) contact assignment. The false positives occur when two particles with high stress are neighbors but not exerting any force on each other, whereas false negatives occur when the forces through the contacts are so low that the intensity of light it produces falls close to the limit of imaging sensitivity.

We overcome both issues raised above and increase the precision of contact deter-

mination by employing a two step process. The first step involves obtaining possible contacts based on the distances between disk centers, and employing a threshold (10%D) below which the disks are considered to be in potential contact. This estimate of contacts is significantly improved by utilizing the photoelastic stress images at various exposure times for each state, such that eventually most of the force transmitting contacts can be seen. As seen in Figure 4.1b,c, the contacts through which there is force transmission, appear as source points for the stress pattern. This effect can be quantified by measuring the intensity and the gradient square of the intensity (G^2) around the contact [How99]. A true, force bearing contact can be distinguished by employing appropriate thresholds in intensity and in G^2. The threshold in intensity is useful in capturing contacts with very small forces, reducing errors due to false negatives, whereas the threshold in G^2 helps in capturing contacts with larger forces and reduces errors due to false positive, since the G^2 around a contact is significantly higher for a true force bearing contact. The final error in average coordination number is around 2%. The errors are not the same for every ϕ; they are about 3.5% for very low ϕ and about 1.5% at high ϕ. The average coordination number can be computed either by counting only the force bearing disks or by counting all the disks including rattlers, which are disks without any contacts. The rattlers do not contribute to the mechanical stability of the system. We present data for both cases.

From a mechanical point of view, the pressure of the system is one of the most important quantities for isotropically compressed systems. Here, the pressure is computed from the measured contact forces [MB05]; the Cauchy stress tensor $\sigma_{ij} = \frac{1}{2V}\sum(F_i x_k + F_k x_i)df$, for each disk is computed first, where V is the volume of the disk. The trace of the tensor is found for each disk, which is then averaged over the entire system to yield the pressure. Finally, ϕ is calculated by measuring the total area of the disks and dividing it by the area of the confining box at each de-

compression state. We perform two sets of experiments; one with a relatively larger range in ϕ (0.8390 - 0.8650), and also larger step size in ϕ (0.016). The second set of experiments are done at a finer scale, once the jamming region is identified from the first set. In the second set, we have a smaller range of ϕ (.840745 - .853312), and a finer step size in ϕ (0.000324). This allows us to determine the jamming point with an unusually high precision.

4.3 Results

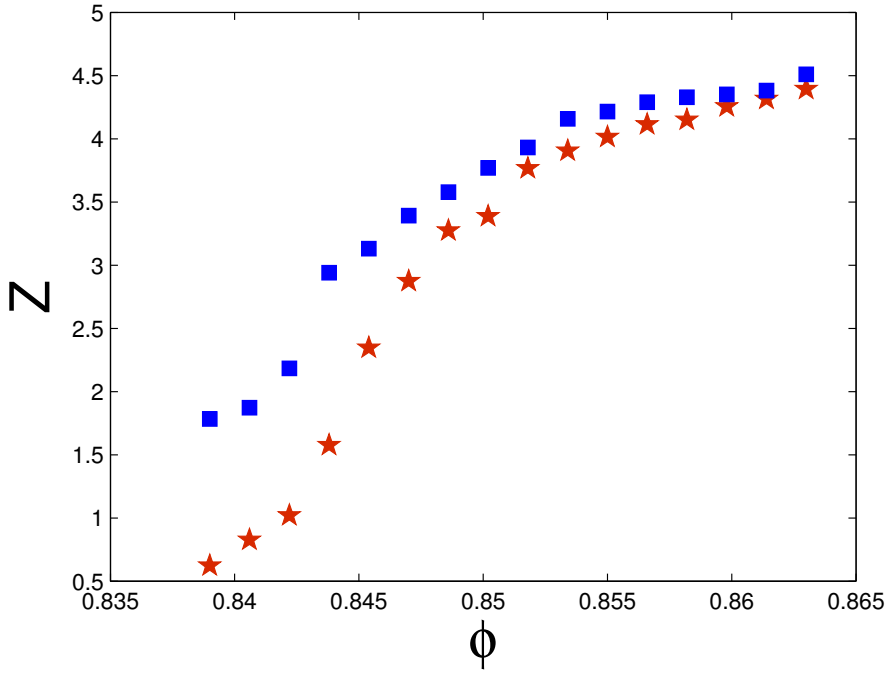

Figure 4.2: Z vs ϕ for a relatively larger range of ϕ.

Figure 4.2 shows data for Z over a relatively broad range of ϕ. The data for $Z(\phi)$ indicate a significant rise in Z at the jamming transition. The rise in Z is clearly shows some rounding, and we discuss below some likely origins of this feature. Figure 4.2 shows two curves; one with rattlers (red stars) and one without rattlers (blue squares). At higher ϕ, the variations of the cureves are similar. At lower ϕ, the

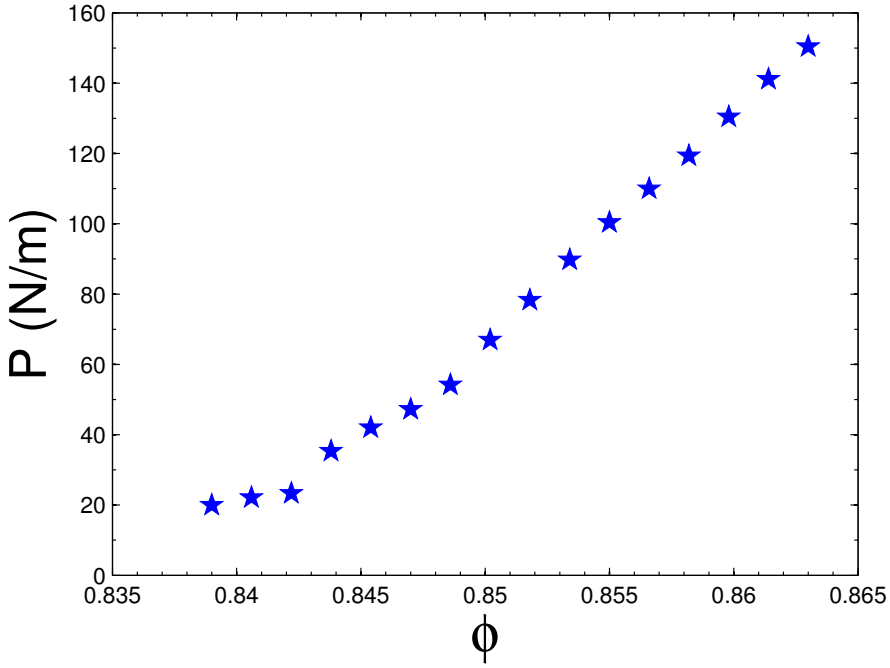

Figure 4.3: Pressure vs ϕ for the larger range in ϕ.

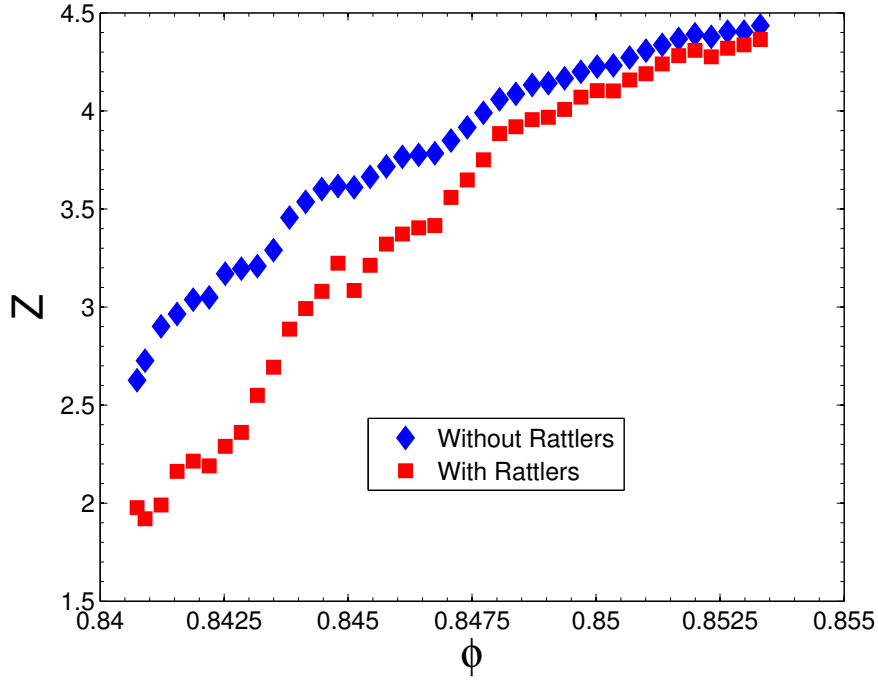

Figure 4.4: Z vs ϕ at a finer scale in ϕ.

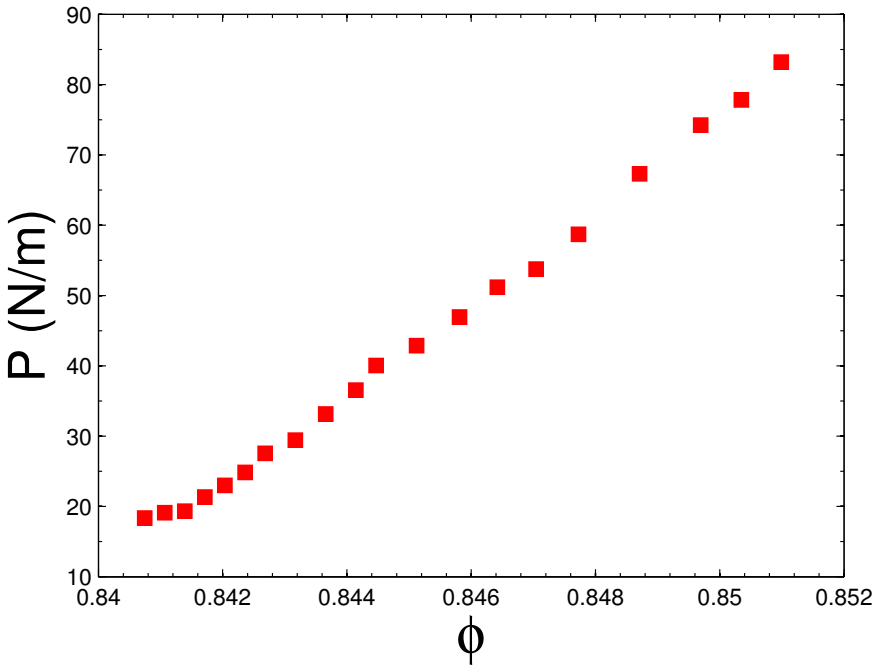

Figure 4.5: Pressure vs ϕ at a finer scale in ϕ.

behavior differs; the values of Z drops much lower for the case with rattlers, and the transition is somewhat less apparent.

Figure 4.3 shows data for variation of Pressure (P) over a broad range in ϕ. $P(\phi)$ also shows a sharp change in slope at a well defined ϕ. The pressure is not identically 0 below jamming for the same reason that the jump in Z is not perfectly sharp.

Figure 4.4 shows the variation in Z with ϕ over a narrow range close to the jamming point. Again, over a relatively narrow range, the distributions change dramatically. We again consider two cases; one with rattlers excluded from the coordination number calculation and the other in which they are included. The behavior is similar to the long-range case.

From the case where rattlers are excluded (blue squares) we observe a clear transition point at $\phi_c = 0.8422 \pm .0005$, where the coordination number is 3.04. Beyond this ϕ_c, Z increases as a power-law given by $(Z - Z_c) = b(\phi - \phi_c)^\beta$. This is a clear

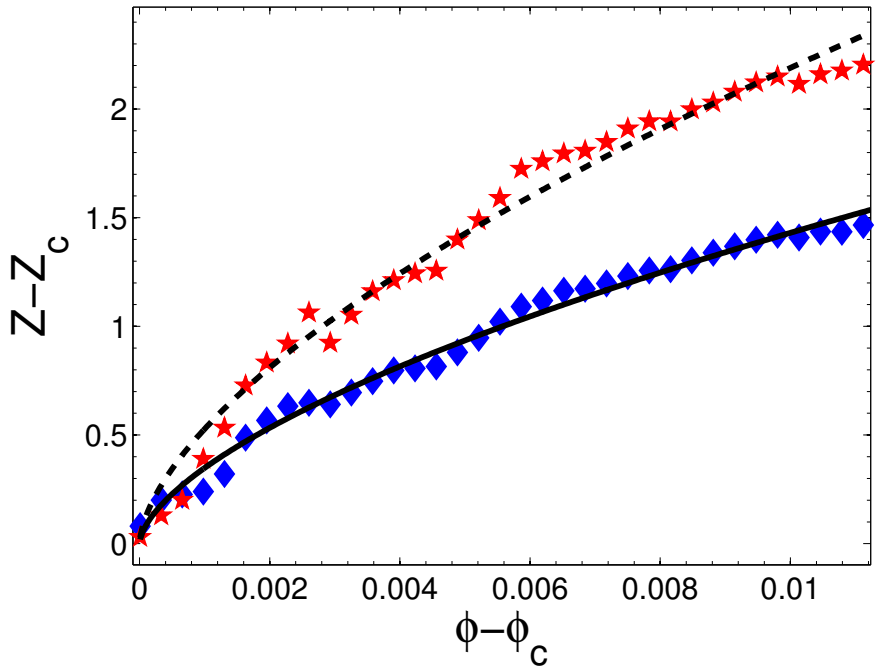

Figure 4.6: Power-law fits for Z vs $\phi - \phi_c$.

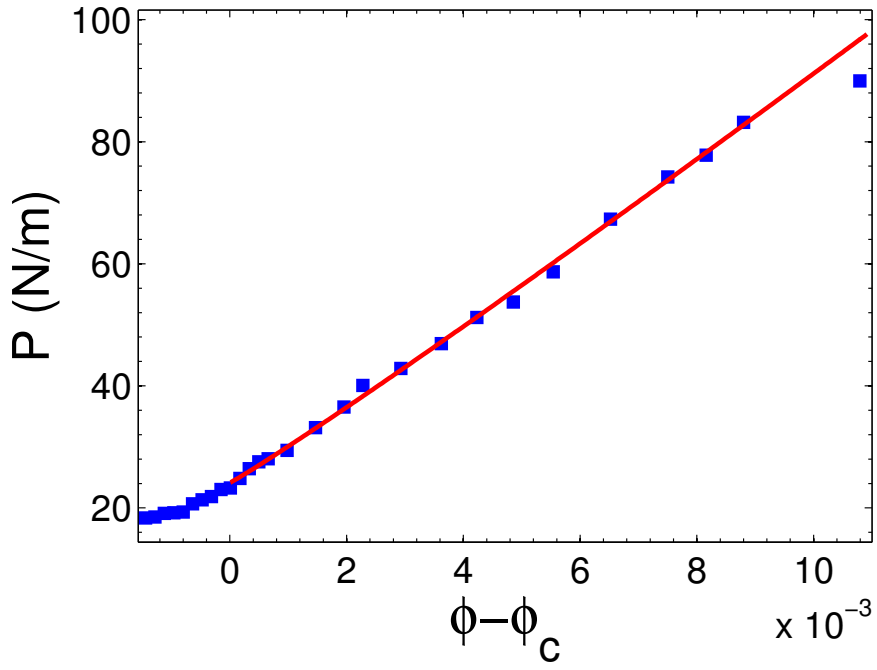

Figure 4.7: Power-law fit for P vs $\phi - \phi_c$.

ϕ_c	Without Rattlers		With Rattlers	
	Z_c	β	Z_c	β
0.84058	2.390 ± 0.135	0.5166 ± 0.064	1.198 ± 0.310	0.5024 ± 0.093
0.84075	2.512 ± 0.138	0.5472 ± 0.073	1.071 ± 0.359	0.4601 ± 0.090
0.84172	2.632 ± 0.151	0.4935 ± 0.077	0.9747 ± 0.458	0.3631 ± 0.083
0.84204	2.858 ± 0.127	0.5637 ± 0.086	1.183 ± 0.413	0.3665 ± 0.079
0.84236	2.916 ± 0.133	0.5555 ± 0.093	1.744 ± 0.298	0.445 ± 0.088
0.84269	3.003 ± 0.124	0.5627 ± 0.095	1.989 ± 0.267	0.4691 ± 0.092
0.84301	3.075 ± 0.12	0.5603 ± 0.095	2.28 ± 0.235	0.5245 ± 0.108

Table 4.1: A table showing power-law exponents, and critical coordination number obtained as fitting parameters, at various critical packing fractions.

signature of jamming in the system. The curve with rattlers included has much lower coordination numbers, and the transition-like behavior is smeared out, although the power-law increase in Z with ϕ is still evident. Due to rounding of the curve around the proposed ϕ_c, it is likely that the exact value of the critical packing fraction could be in a range from 0.84 to 0.843. The nature of the growth of Z depends on the choice of ϕ_c, as we demonstrate below.

We now focus more closely on the regime very close to and just above jamming, with an eye towards testing recent predictions for the critical exponents. Figure 4.6 shows the variation of $Z - Z_C$, above jamming on a fine scale. The actual power-law increase in both instances are also shown in Figure 4.6 as solid lines. The fits to the experimental data are good. As mentioned previously, the power-law exponents can be different for different ϕ_c. In order to examine this variation, we examine a range of values for ϕ_c and obtain the exponents to the power-law fits, as shown in Table 4.1. Here, ϕ_c is selected, and Z_c, and β are the fitting parameters. It can be seen that the exponent ranges from 0.51 to 0.56, and Z_c ranges from 2.39 to 3.075, for the case without rattlers. For the case with rattlers, the exponents show more variation (0.36 - 0.52), and the errors in Z_c are larger. The values of the power-law exponents for the case without rattlers are roughly between the values predicted by Silbert et al., and O'Hern et al. ($\beta = 0.5$), and Donev et al. ($\beta = 0.6$). Both of these sets

of simulations apply to frictionless particles. By contrast, for frictional disks under shear, Aharonov and Sparks obtain the much lower value, $\beta = 0.36$. However, a direct comparison is not possible to the case of jamming under isotropic conditions.

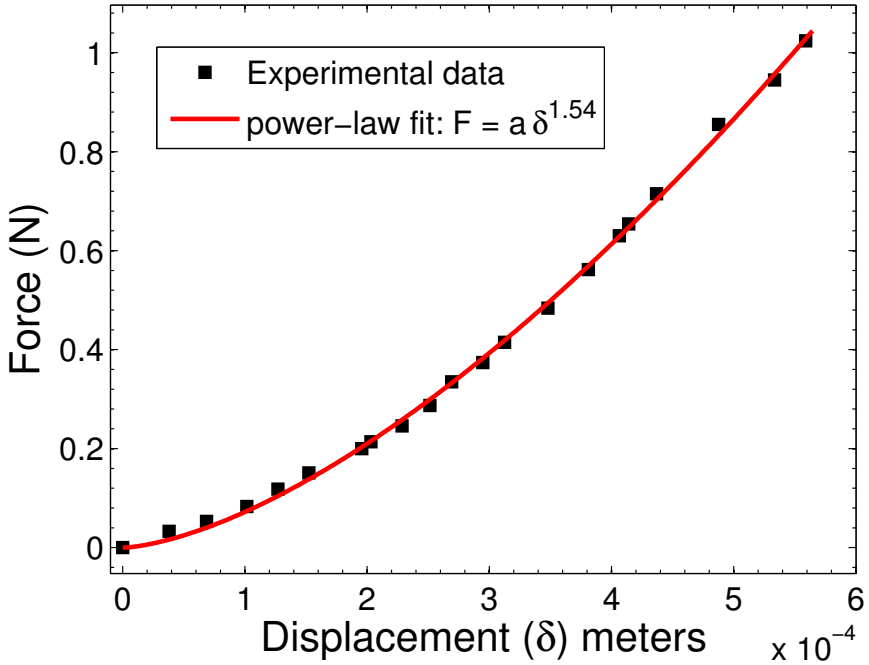

Figure 4.8: Force vs. deformation curve for a single disk: Hertzian fit.

Figure 4.7 shows the variation of pressure with packing fraction. A clear transition is again observed when the packing fraction is at $\phi_c = 0.8422 \pm .0005$. The pressure increases with an exponent of $\psi = 1.1$, slightly greater than 1.0 beyond the critical packing fraction, a feature observed in all of the numerical studies mentioned above. The value of ψ that we measure is very close to what one might expect from the predictions of [SEG+02, OLLN02], assuming that our disks are ideal. In that case, linear elasticity predicts a contact force potential that is nearly harmonic, i.e. such that the potential varies quadratically in the disk compression, and $\alpha = 2$, hence $\psi = \alpha - 1 \simeq 1$. However, a careful calibration of the potential for our disks indicate an α that is slightly greater than 1.0. We believe that this occurs because initially,

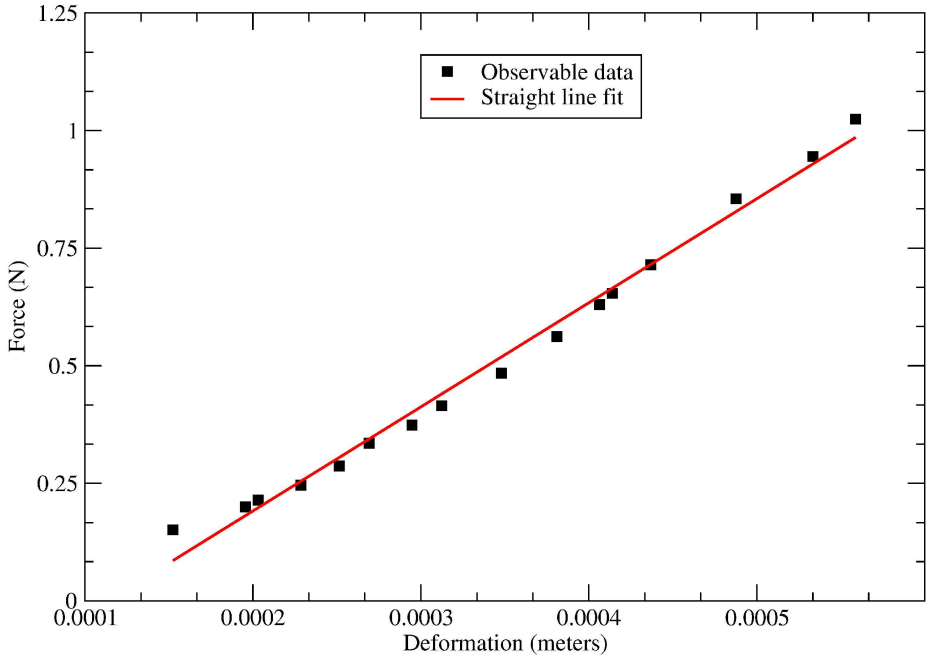

Figure 4.9: Force vs. deformation curve for a single disk: Linear fit.

as two particles are pushed together, there is deformation of the asperities on the surfaces of the particles, which behave like Hertzian contacts. The force law then becomes more linear for somewhat larger compressions, once the asperities have been larger "flattened".

This issue becomes clear from Figure 4.8 and Figure 4.9. Figure 4.8 shows for a single disk under compression, the variation of the force with compression. The forces are measured with a digital force gauge with a resolution of 0.001 Newtons. The deformation is measured by a micrometer with a resolution of 2.45×10^{-5} meters The curve can be fit very well by a Hertzian force law of the type $F = a_0 + b\delta^{\gamma}$, where $\gamma = \frac{3}{2}$ for a Hertzian solid. The actual exponent we obtain is $1.54 \pm .04$. This calibration covers the full range of forces (0 N - 1 N) reasonable for our disks. In practice, all our measurements are performed by imaging. The nonlinear response of the camera and the nature of birefringent material is such that a recognizable optical

intensity signal begins only beyond 0.010 N. If we then restrict our force-deformation fit to forces greater than 0.010 N, then we get a reasonable linear fit to the curve. This would be in line with the preceding observation about the value of ψ being close to 1.

The value of the critical packing fraction obtained from the pressure is very close to the one obtained from Z vs ϕ curve. This result clearly is consistent with a simultaneous transition in both Z and P occurs at a critical packing fraction.

We now turn to the rounding that we observe, particularly in Z quite close to the transition.

One of the causes for this rounding is friction between the disks and the Plexiglas base, which prevents small fragments of force chains to persist and retain a small amount of stress. Moreover, the motion of the walls induces a small amount of shear, which retains a small amount of stress near the jamming point. The same cause also produces anisotropy in stress and contact network before a system is fully jammed; indications of these anisotropies can be seen in Figure 4.1e. Moreover in this region the grains in the packing are still undergoing substantial rearrangements, and hence strictly speaking are not jammed.

We conclude by noting that these experiments, the first of which we are aware, demonstrate the novel nature of jamming transition. These results take advantage of the high resolution in contact number that is afforded when the particles are photoelastic. They show, modulo some rounding in Z, the predicted jump in the mean particle coordination number, Z at a $\phi_c = 0.8422$ for both Z and P. Above ϕ_c, Z and P follow power laws in $\phi - \phi_c$ with respective exponents of 0.56 and 1.1, which are reasonably consistent with recent predictions for *frictionless* particles. The effects of friction are likely to be modest, based on recent results[MB05] which show that the mean frictional force is only about 10% of the normal force for isotropic

compression. We observe some rounding, which may be attributed to two sources: 1) small residual friction with the base on which the particles rest, and 2) small residual shear stresses that are induced by preparation history. The ability of a small amount of shear to affect the jamming transition is interesting, and points to the need for a deeper understanding of failure under non-isotropic conditions.

Chapter 5

Plastic deformation in sheared systems

In this chapter we will investigate sheared systems from the point of view of plasticity of the system. A dense sheared granular system jams and unjams repeatedly under shear. For each sequence of jammed states, the stress and the energy in the system increases, and for every unjamming event, the system rearranges, and yields, resulting in a drop in the stress and the energy of the system. At the macro-scale, this behavior is sometimes seen as stick-slip behavior similar to that found in frictional properties of other systems. We see such rise and fall of stress in a simple situation like solid-on-solid friction [Per98], and also in highly complex systems like earthquake faults [MRS90, AHT00] .

Here we investigate the evolution of sheared systems. We measure both, the displacements of the particles and the forces on the particles to study how the system evolves under continued quasistatic shear. We hope to gain a better understanding of the macro-scale behavior of the system from grain-scale measurements. In particular, we study the stress-strain, or the energy-strain behavior of the system to understand the dissipative properties of the system. The stress measurements are augmented by tracking particle locations, and measuring the particle displacement profiles to understand particle motions during elastic segments, and plastic failure events.

The grain-scale mechanism of such a complicated macro-scale behavior is quite simple sounding. When a system is under shear, and a contact network is established, the contacting grains carry loads until they no longer satisfy force and torque balance. At this point, the grains slip against each other and rearrange so as to conform to the next mechanically stable arrangement. The process of slipping causes irreversible

energy loss, if the grains are frictional, and also irreversible or non-affine displacement. Non-affine displacement refers to the portion of the total displacement of the grain which is over and above that dictated by the boundary displacements. It is the non-elastic, or non-reversible, or non-affine displacement.

The crucial issue here is the meso-scale dynamics, or the effects of collective motion of small groups of grains. It is the collective behavior of such irreversibly rearranging groups of particles, which give rise to the macro-scale properties of the system. Recently, there have several interesting theoretical approaches put forward, which explicitly take account of irreversible deformation of groups of particles [FL98, TWLB02, ML04b, ML04a, AHT00].

One such approach is the Shear Transformation Zone (STZ) theory [Arg01, FL98], which imposes transformation rules for the local rearrangement of a group of grains, and studies the global effects of such transformations. Other approaches are more directly numerical [TWLB02], where different quantities are used to define the irreversible part of the deformation and the pattern of the non-affine displacement throughout the system is studied. These approaches have begun to shed more light on some of the intriguing phenomena exhibited by sheared granular systems, like the formation of shear bands, shear localization, and plastic failure events in granular systems.

In the rest of the chapter, we begin by briefly describing some of the theoretical ideas behind the STZ theory, and other related works. We then briefly describe our experimental procedure, and present our results.

5.0.1 Theoretical approaches

We will cover a few recent numerical, and theoretical studies, which deal with the role of non-affine displacements in sheared amorphous systems. We will in particular

describe the STZ theory, and briefly mention numerical simulations by Tanguy et al.

The ideas behind the STZ theory came about from simulations on metallic glasses [Arg01, Arg82, AS04], and experiments on soap bubble rafts [AK78, AS82]. These works revealed that the smallest scale or "atomic scale" motions during plastic shear were confined to a cluster of particles few particle diameter in length. These results led Argon to put forward a mean field theory of the transitions localized in space termed as the "Shear Transformation Zones" (STZs), where each such STZ was a unit of plastic deformation. Falk and Langer later found the mean field equations of motion for the number density of STZs, which were found to be applicable to strain hardening in metallic glasses [FL98]. Such an approach may not be limited to metallic glasses, but could be potentially useful in many amorphous systems including granular systems [ML04a]

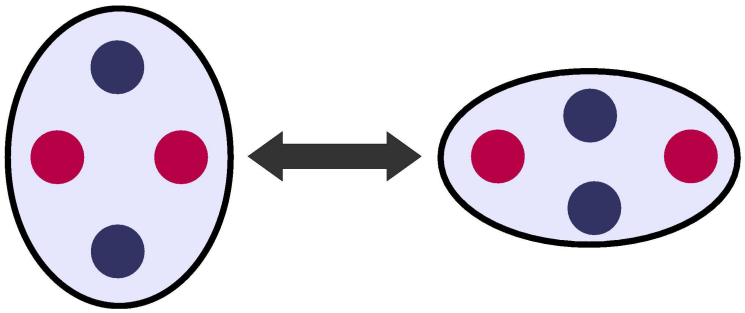

Figure 5.1: Schematic diagram of the Shear Transformation Zone.

Figure 5.1 shows a unit of STZ. Consider this group of four particles in an initial state (left). A two-state transformation rule brings farther particles closer, and pushes nearer particles farther apart, while still maintaining this group as a local cluster (right). This is a simple example of a local, irreversible transformation zone. A number of such STZs are distributed throughout the system, but the STZs themselves do not diffuse in the system. A key ingredient of the STZ, and related models is to describe global plastic deformations in terms of these local units of irreversible

deformations.

Recently Maloney and Lemaitre have extended these ideas to include interacting STZs, and studied plasticity in amorphous systems using athermal quasi-static simulations (AQS). The main idea behind this simulation is to apply alternate steps of elastic deformation with energy relaxation, which keeps the system in a local energy minimum [ML04b].

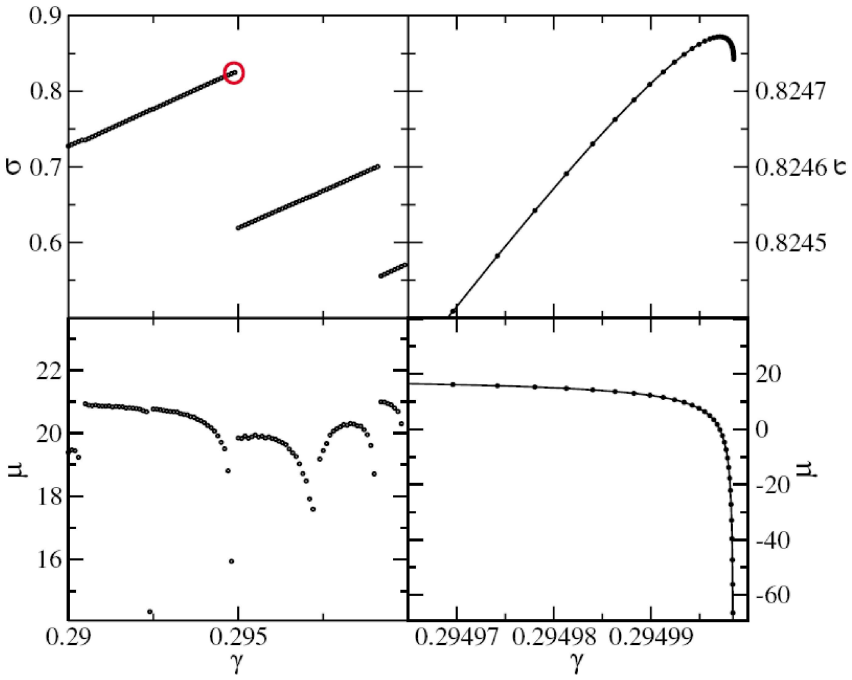

Figure 5.2: Stress-strain behavior and elastic moduli, from [ML04b].

Their detailed study of the onset of plastic failure, reveals several interesting features associated with plasticity in sheared amorphous systems. They have found that macroscopic stress and energy fluctuations arise as a series of reversible branches of the stress-strain curve, interrupted by irreversible events. The elastic moduli of the system diverge at these transition points. These observations are captured in Figure 5.2, taken from [ML04b]

A second set of observations deal with the spatial profiles of the non-affine dis-

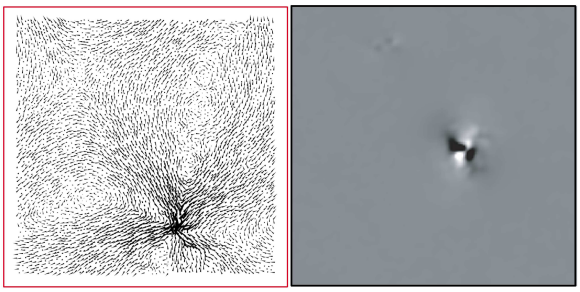

Figure 5.3: Non-affine displacement at the onset of plastic failure. (from [ML04b, ML04a]).

placement field, and the energy changes in the system. It was found that at the onset of a plastic failure event, the non-affine displacement field, and the energy changes show quadrupolar alignment, as can be seen in Figure 5.3 (modified from [ML04b, ML04a])

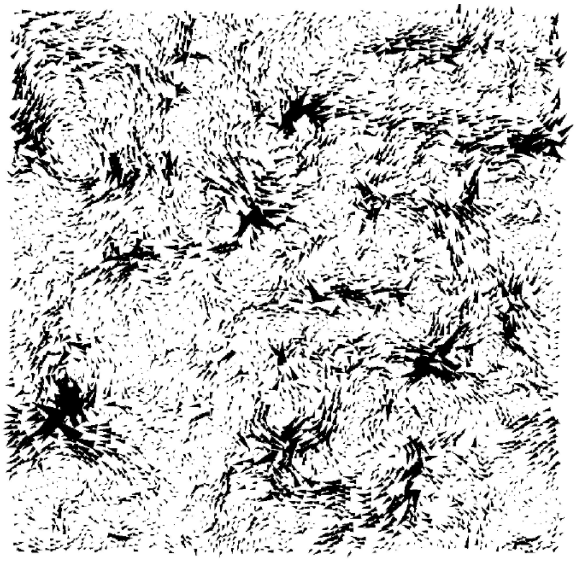

Figure 5.4: Non-affine displacement of sheared system. (from [TWLB02]).

Studies of sheared amorphous systems by Tanguy et al. [TWLB02] show similar interesting results. These are numerical simulations of a large number of disk-shaped two dimensional particles with Lennard-Jones interaction potentials. They find a breakdown of continuum elasticity below a characteristic length-scale of approximately 30 molecules. The studies also find that the non-affine displacement field

shows correlated, vortex patterns, also with a correlation length of 30 molecules, as seen in Figure 5.4.

A similar study of plasticity in uniaxially compressed granular system by Åström et al. [AHT00] in the context of earthquake fault zones reveals that the displacement pattern of grains fall in distinct zones; in the upper and lower part the grains move homogeneously, where as two narrow shear bands appear, where the grains are rotating. The authors term these groups of rotating particles "roller bearings".

These theoretical and numerical studies have opened up a way to understand macroscopic plastic behavior using "atomic-scale" properties. Another appealing feature of these studies is that they have experimentally testable predictions. In our case, with the help of our biaxial test apparatus, we can create a variety of precise loading conditions, and combined with the grain-scale position, and contact force measurements, we can test some of these predictions concerning irreversible deformations in sheared granular systems.

5.1 Experimental procedure

The experimental setup for this experiment is much like the previous experiments. We use a biaxial test apparatus to apply pure shear to the system, and image the system from above with a high resolution (8 MP) color CCD camera.

As in earlier experiments, we use a bi-disperse mixture of approximately 8 mm and 9 mm photoelastic disks. The fraction of smaller disks is 80 % and those of the larger disks is 20 %. The total number of disks is 3000. The material parameters of the disks are exactly as before. The imaging resolution is such that 1 pixel corresponds to .0001 meters. In other words, each disk is imaged within a window of roughly 80×80 pixels. As shown in Figure 5.5, the setup is placed horizontally, and imaged from above, through crossed circular polarizers. Two of the walls of the biax are

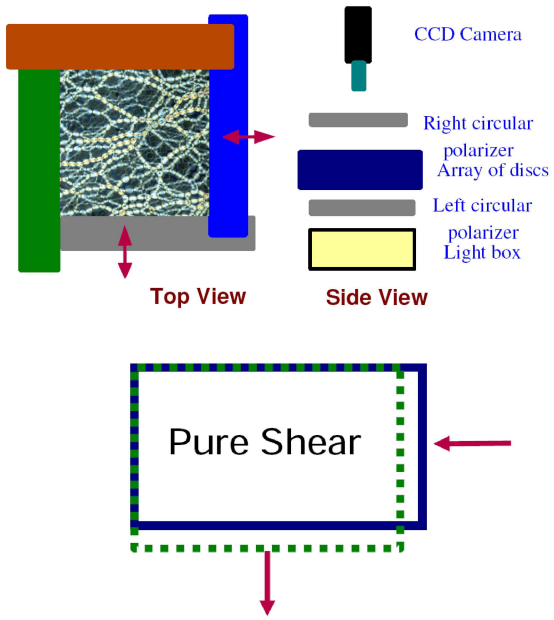

Figure 5.5: Experimental setup (top) and schematic illustration of application of pure shear (bottom).

moved as shown in Figure 5.5 (bottom), to apply pure shear. The initial box size is roughly 40 cm $\times$ 40 cm, and the strain is measured as:

$$Strain = \epsilon = \frac{\mid \delta L \mid}{L} \tag{5.1}$$

The experimental procedure is briefly summarized in the following. We start from a stress-free state in which the disks are randomly placed, so as to ensure that there is no global or large-scale crystallization. Incremental, quasistatic deformation is applied to the system by moving one of the walls inwards, and the perpendicular wall outward by the same amount. The linear distance per step $\delta L \approx 0.05D$, where D is the average diameter of the disk. The strain step in these experiments is always 0.0012.

The state of the system is imaged at every shear step after a strain of about 8 %. Two images are captured; one with polarizers, and the other without polarizers. The

polarized image gives stress information and the unpolarized image is used to obtain disk centers. The images cpatured are RGB images of size 3264×2448 pixels. At the resolution per disk mentioned above, we can capture roughly 1300 disks around the center of the biax; slightly less than 50% of the disks. This allows us to obtain information about most of the bulk system, and leaving out the boundaries to avoid boundary effects.

The difference in this experiment compared to our previous experiments is the application of shear in forward and reverse direction. One of the goals of this study is to understand the energy dissipation of the system; cyclic loading and unloading is traditionally used to extract any hysteretic features in the system. In the present study, we restrict our protocol to one cycle.

Figure 5.6 shows six stages in each forward and reverse portion of the shear cycle. Each image is 3264×2448 pixels in size, which corresponds to 32 cm $\times$ 25 cm. On the top left is the image of the system at a shear strain of 8 %, where we begin imaging. The last image in the second row is at the end of forward shear portion where the strain is 11.2 %. The direction of the shear is reversed after this point, and the system is brought back to its same shape and size in the same number of deformation steps. The first image in the third row is the first reverse shear step. The rightmost image in the last row is at the end of the reverse shear portion of the shear cycle, where the strain is 0.08.

Our approach for analyzing these data is as follows:

- From the unpolarized images of the entire cycle, find disk centers
- Use the disk centers to track each disk throughout the cycle
- Use the stress images to determine forces on the disks by methods previously described

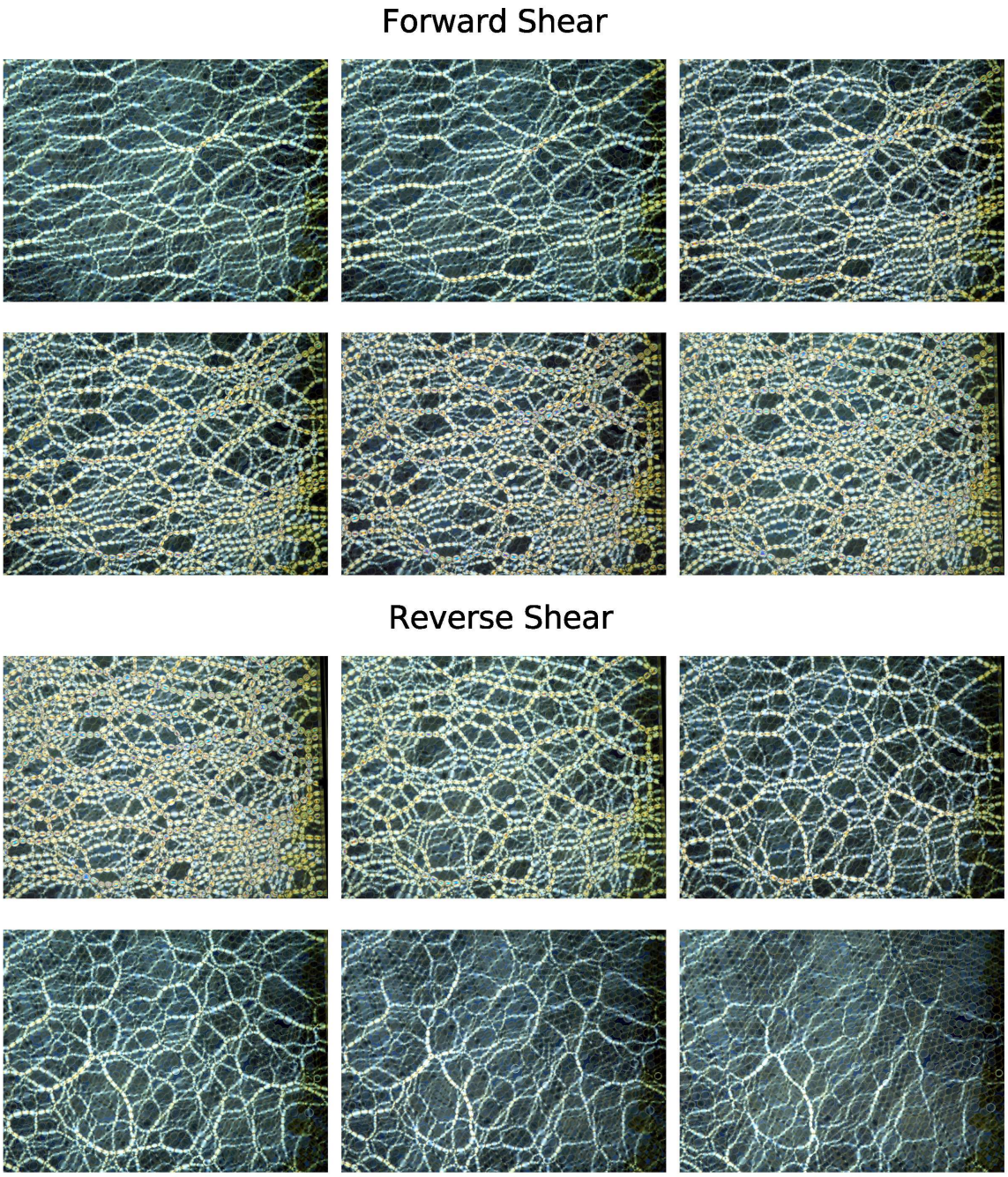

Figure 5.6: Stress images for one cycle of shear. Each image is 3264 × 2448 pixels, which corresponds to 32 cm × 25 cm in size.

- track positional and stress changes for each disk throughout the shear cycle

The positional changes will give us information about the collective motion of the disks during elastic segments, and at the plastic failure event. The force measurements, which in turn give us the stresses and energies of the disks, inform us about the energy changes in the system.

The forces in the system are determined in two separate ways. One method is the empirical approach using the gradient square (G^2) technique described in Chapter 2. The average gradient square over a disk gives us an estimate of the magnitude of the force on that disk. From prior calibration it is known that G^2 is linearly proportional to the force, and can be used to estimate the average force. The average over the entire image, i.e. all the disks in the image, gives us the average stress in the system.

The second method is the more exact method of finding contact forces at each contact of each disk in an image by the inverse problem solution method described in Chapter 3. It gives us the exact Cauchy stress tensor for each disk. The trace of this tensor gives us the average pressure on a disk, which when averaged over the entire image, gives us the average pressure over the system.

5.2 Results

We begin the results by describing the qualitative features seen in Figure 5.6. In the first image in the first row, one can observe a well developed stress state with long force-chains roughly along the principal strain direction. There are smaller side-chains with weaker forces, which may act as a backbone structure supporting the strong force-chains. Between each successive image, the strain increases by 0.0072. The second row of images are towards the middle and end of the forward shear portion. The rightmost image in the second layer is the last step in the forward

shear, where the strain is roughly 11.2%. There is a visible increase in stress not only along the long force-chains previously established, but also along the side chains.

The direction of the shear is reversed from this point on. In exactly the same number of deformation steps, the system is returned to its initial shape and size starting from the top left image. The leftmost image in the third row shows the stress state after the first reverse step. Again, the successive images have strain difference of .0072. The rightmost image in the fourth row shows the state of the system when the system returns to the same size as that when we began imaging the system. As can be seen from the image, the stress is much lower than the initial state, and the direction of the strongest force-chains is roughly vertical. This state of stress is clearly not the same as the very first image, either in magnitude of stress or the direction of strong force-chains. This points to large overall rearrangement of the disks, and "dissipation" of stress, though from the stress images, only the reduction in stress can be readily observed. In the following section we will present more quantitative results on the variations in stress with increasing shear.

5.2.1 Stress and energy changes

As described in the previous section, we measure stress from photoelastic images by two different methods. We will first present the results obtained by employing the empirical G^2 technique. The principal advantages of this method are ease of implementation, and relatively smaller computational time. At the same time, when combined with a rigorous calibration between the applied force on the disk and the G^2 averaged over the disk, the method is very accurate in estimating the amount of force or the average pressure on the disk.

Traditionally, the stress-strain behavior of any material is of fundamental significance to ascertain the constitutive behavior of the system, which in most cases can

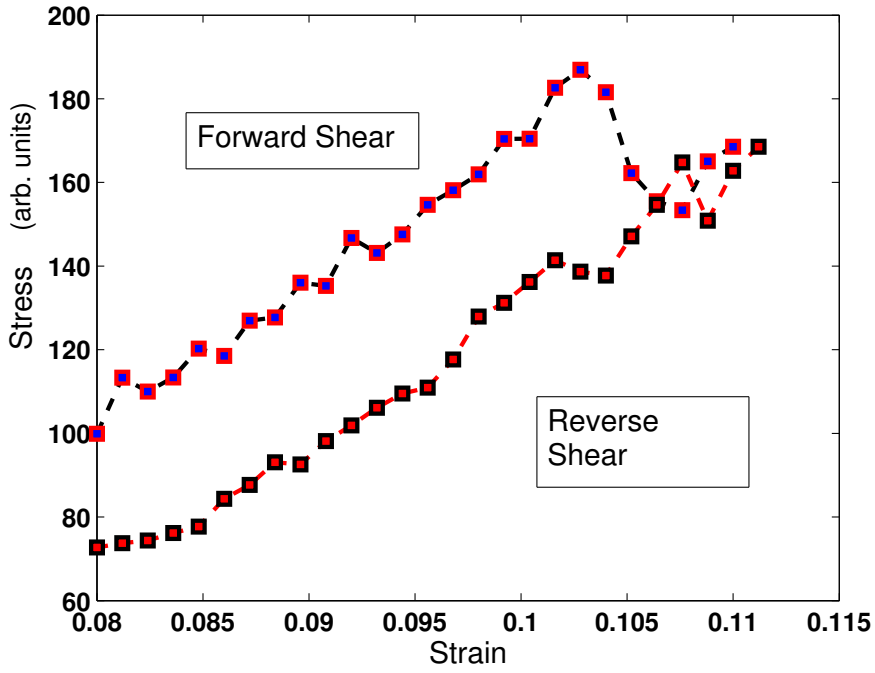

Figure 5.7: Experimental stress-strain curve for forward and reverse shear using the G^2 technique.

not be derived from first principles. Figure 5.7 shows the stress-strain curve for the entire cycle of forward and reverse shear. The most striking feature of this curve is its hysteretic nature, which confirms the drop in stress during the reverse shear phase quantitatively.

The second aspect of importance is the nature of variation of each branch of the curve. Consider the upper curve for the forward shear. It can be observed that there segments during which the stress increases linearly. These are segments during which the system behaves like an elastic solid. During these linear, elastic segments, all the shear stress imposed on the system is borne by the pre-existing network of force-chains.

The elastic portions are interrupted by sudden drops in stress within a single strain step. These events are plastic events where the system can no longer support

the additional shear stress imposed on it, while still retaining its mechanical stability. The system responds by rearranging the particles such that a new mechanically stable configuration is achieved, and the stress on the system is reduced. This is achieved with the help of not only individual grain-scale motions, but also a more correlated collective motion of the grains. The magnitudes of stress drops vary, depending on the exact stress state of the system. Stress drops of both small and large magnitudes can be observed.

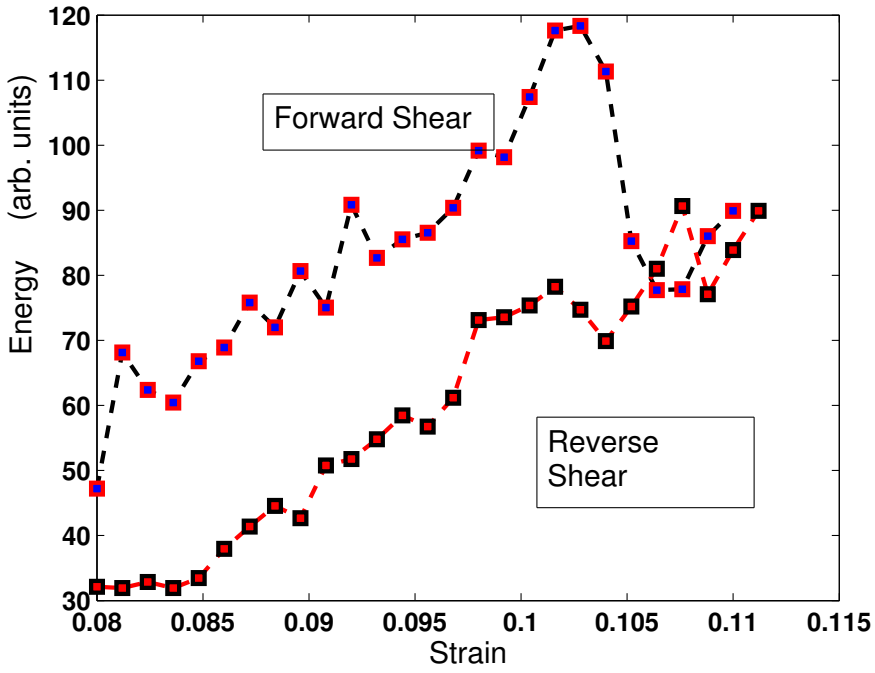

Figure 5.8: Experimental energy-strain curve for forward and reverse shear using the G^2 technique.

The elastic and plastic regions of the material behavior can be seen more clearly in the energy-strain curve. The energy is obtained as the average $(G^2)^2$. The drops in stresses are of larger magnitudes. The total area inside the hysteretic loop represents the energy loss of the system.

We turn next to a similar analysis of the stress-strain behavior, but this time using the vector contact force measurement technique described in this thesis. Figure 5.9

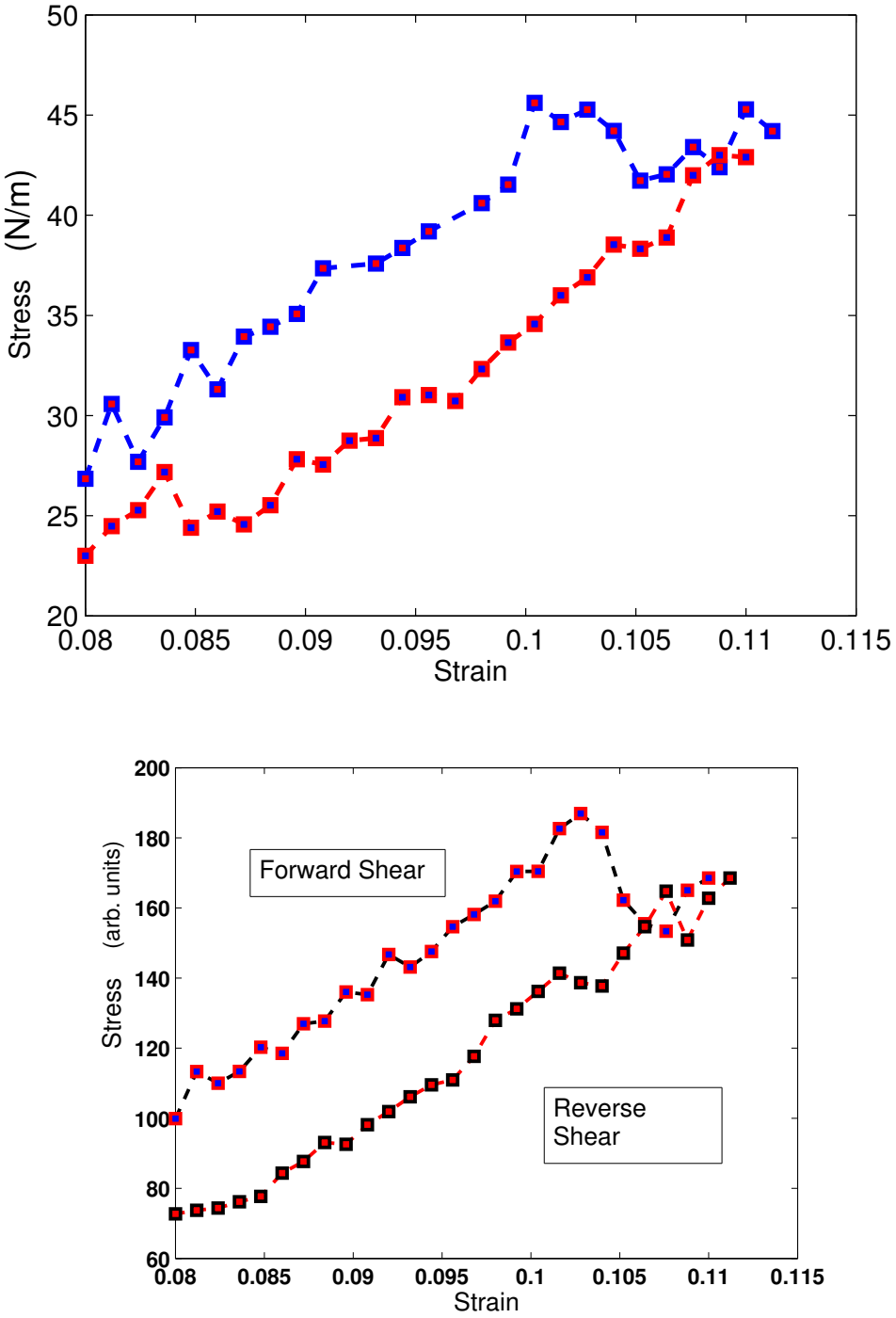

Figure 5.9: Experimental stress-strain curve for forward and reverse shear obtained using the force components measurement technique (top). The same curve using the G^2 technique, shown for comparison (bottom).

(top) shows the stress-strain behavior over the entire cycle. The plot is remarkably similar to Figure 5.7, which is reproduced in Figure 5.9 (bottom), for comparison. We can observe similar features in both plots. There are elastic segments, and plastic failure events, with the trends of both curves being almost the same, though one can also observe minor differences. This kind of stick-slip behavior is seen in many systems as discussed earlier. It is well known in solid friction studies. In granular systems, besides the overall stick-slip behavior, there are many intriguing aspects associated with motion of grains under shear. We next examine the effects of shear on displacements of the grains.

5.2.2 Particle displacements

Particle displacements offer us further insight into the response of the system to pure shear. We begin imaging the system when there is 8% shear strain already present. We track subsequent development of the system upon application of more shear. One aspect of this is the developement of shear bands in the system, which is a typical occurence in sheared granular systems. Also the grains within a shear band support a small fraction of the applied load. Within our experimental operating parameters, we can examine the dynamics of such shear bands.

Figure 5.10 shows a striking pattern of displacements. The figure is obtained in the following manner. First, the centers of disks are found for each strain step. The disks in each of these sets are uniquely tagged to make them identifiable. Then the locations of the disk centers are compared between a strain state and the previous strain state, which give the displacement for each disk. The mean displacement is subtracted from the displacement of the individual grain displacement. The resulting displacement vectors are scaled and plotted as a vector field. The red arrows are placed for ease of visualization. Each image is roughly 30 cm $\times$ 23 cm in size; a smaller size than the

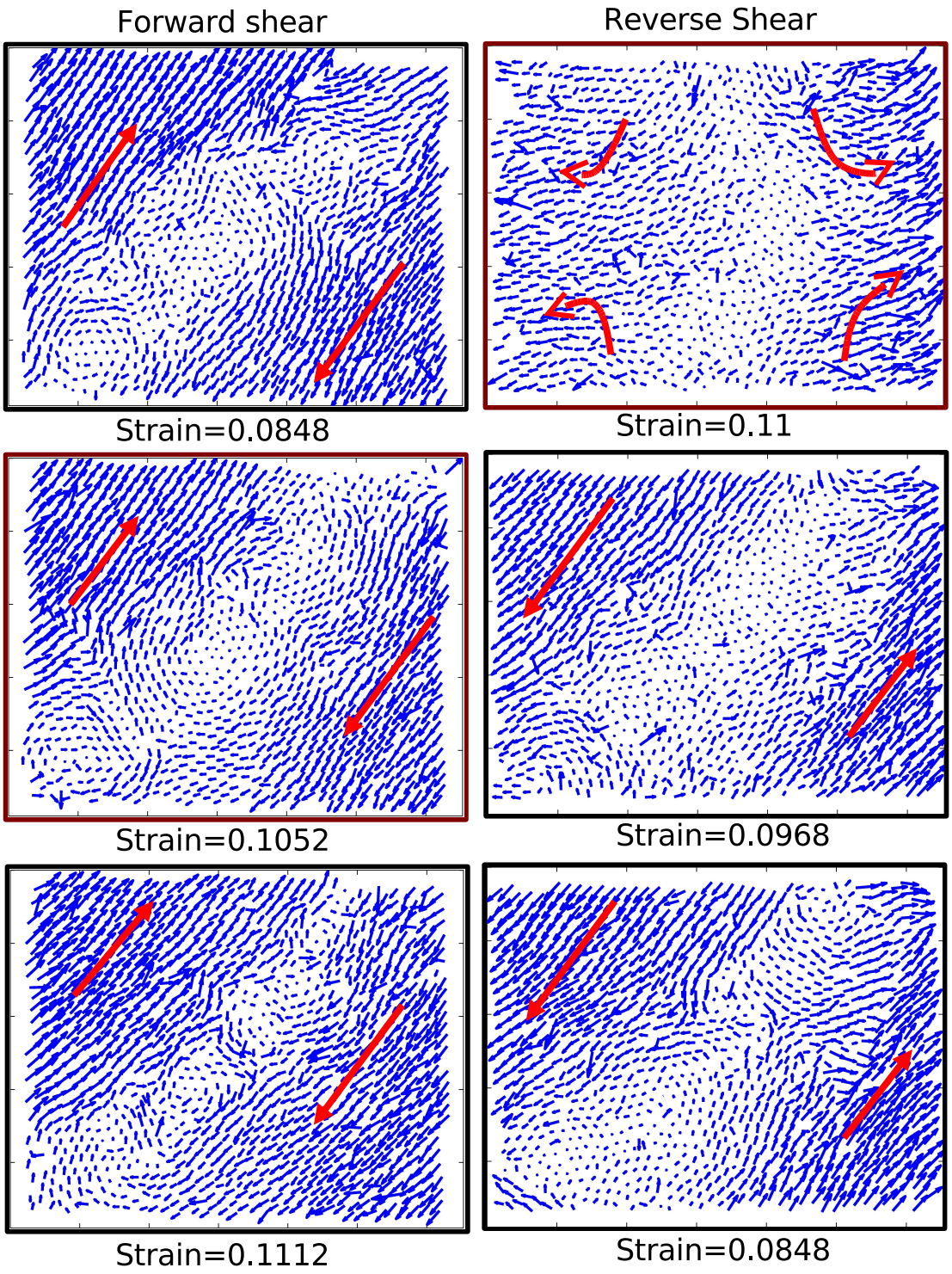

Figure 5.10: Particle displacements: forward shear (left column), and reverse shear (right column).

stress images, because the boundary layers have been discarded.

Let us walk through these six displacement vector field plots. Figure 5.10 has two columns, left and right. The three plots in the left column show the displacement field at three different strains during the forward shear phase, and the ones in the right column for the reverse shear phase. The initial strain at the beginning of imaging is $\epsilon = .08$.

Consider first the forward shear portion (left column). The first plot shows the displacement field in an early elastic segment of the stress-strain curve. One can immediately observe three distinct regions of different displacement patterns:

- region in the upper left part moving uniformly upwards at 45 deg
- region in the lower right part moving uniformly downwards at -45 deg
- a central band of grains roughly along the diagonal, with a well-defined *vortex pattern*

The diagonal band with vortices is the shear band in the system, roughly aligned along the principal strain direction. The second plot at $\epsilon = 0.1052$ is the displacement field after the largest plastic event captured in the stress-strain curve. The behavior does not show any dramatic differences from the elastic region, though the width of the band may be somewhat different. The third plot is the last step in the forward shear portion. The displacement pattern is still the same with three distinct regions, but the shear band is significantly narrower. At each strain step some rearrangement of the actual vortex pattern within the band is always evident. The location of the band also shifts somewhat during the forward cycle.

Perhaps the most dramatic event of the entire sequence of forward-reverse shear occurs when the very first strain step is taken in the reverse direction. The first image

in the right column shows the event quite clearly. The entire three-region displacement pattern is destroyed within a strain step of .0012. Not only the homogeneous displacement in the corners is destroyed but the shear band and the vortex motion of the grains is also destroyed. The pattern in the previous step is replaced by a pattern that looks more *quadrupolar* in nature. The motion of grains in all four corners is along different directions, with minimal displacement in the central region of the image. This change in the displacement pattern could be due to sudden change in the principal strain direction being imposed on a pre-existing direction, or it could be due to plastic events taking place over the entire system as opposed to local failure events due to grain slipping. A noteworthy point is that the stress does not show a large drop at the shear reversal point (Figure 5.9).

The second plot in the reverse shear phase at $\epsilon = 0.0968$ shows the development of a flow similar to the three-region flow of forward shear phase. The three-region flow pattern in reverse direction is established only after four or five strain steps. Until then, a transient pattern with remnants of quadrupolar pattern exists. Although the two corner regions show homogeneous displacement, the vortices in the diagonal are not as well-defined as in the forward shear case.

The third plot is at the end of the reverse shear phase, when the system returns to the shape and size it had as the first plot in the forward shear phase ($\epsilon = 0.0848$). The displacement pattern is similar to the forwad flow, but with the directions reversed. Also noticeable is the formation of vortices along the diagonal. The vortex pattern is not as fully developed as the forward shear case, but the shear band is distinctly present, and so are the two elastic displacement regions in the corners.

Thus, the reversal of shear has a dramatic effect of eliminating the flow pattern in the system, including the elimination of the vortex pattern in the shear band. A shear band does begin to develop in the reverse flow but only after a relatively long

transient.

In these displacement plots, we have shown only one type of displacement; with the mean displacement subtracted. There are other measures to characterize non-affine displacements, which could yield somewhat different displacement patterns. Nevertheless, a comparison with the theoretical and numerical works cited earlier may not be completely out of place. All of these studies show examples of vortices in the non-affine displacement pattern. The boundary condition in these studies is simple shear, whereas in our experiments we apply pure shear. This could account for the differences in the location and distribution of the vortices, primarily due to different principal strain directions.

5.2.3 Energy fluctuations

Finally we turn our attention to energy fluctuations. Recall that according to [ML04b, ML04a], at the plastic failure event, the energy fluctuations show a quadrupolar pattern. In actuality, this pattern is observable when a failure event is studied at a finer scale and single drop resolves into a cascade of smaller energy drops. Experimentally this would amount to observing the process almost dynamically with an extremely high resolution in strain steps. Currently this is beyond the scope of any experiments. Instead, we examine what happens to the energy fluctuation patterns in our system, at the plastic failure event of largest magnitude. This should give us some indication of the spatial distribution of energy fluctuations.

Figure 5.11 shows the energy fluctuations after the largest plastic failure event, as decided by the magnitude of the stress drop in the stress-stain curve. It is a difference image of the average energy of the disks at two strain steps. The bright regions are negative changes, and the dark regions are positive changes. There is some pattern of energy fluctuations and a hint of quadrupolar structure, but it is not definitive.

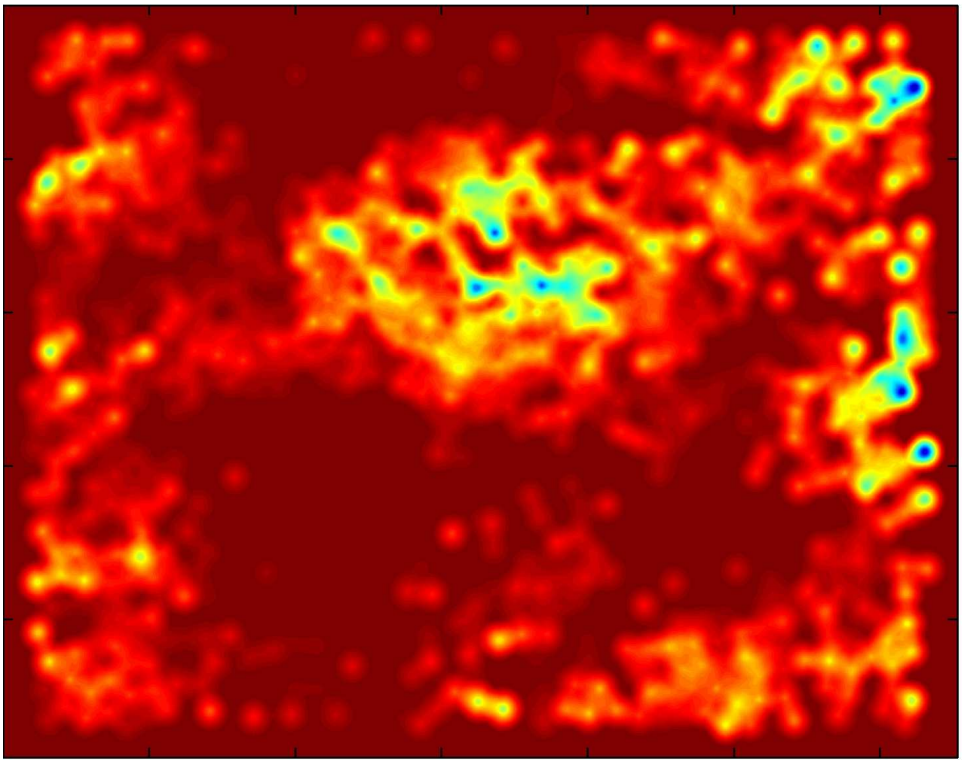

Figure 5.11: Energy fluctuations at the largest plastic failure event.

However, at this resolution in strain steps, we may not be able to capture the effect.

5.3 Conclusions

We have conducted a cyclic shear experiment in order to understand the response of the system to shear in terms of stress-strain relation, energy dissipation, and the grain-scale and collective motion of the particles.

We have found several interesting properties in our study.

- The stress-strain curve obtained using both the G^2 method, and the vector force measurement method, show very similar trends. Each has elastic segments with linear growth in stress interrupted intermittently by drops in stress, typical of stick-slip type of motion.

- The stress-strain curve has a clear hysteretic nature, signifying energy dissipation.
- The energy fluctuations after a plastic event have spatial patterns which may be quadrupolar
- The particle displacement profiles for the forward shear phase show a three-region pattern; elastic motion in two corners, and vortex motion in the shear band diagonally across the system.
- This pattern is destroyed completely upon reversing the shear direction. The resulting displacement has quadrupolar nature. A profile similar to the forward shear is established towards the end of reverse cycle.

These observations, to our knowledge, are the first experimental measurements of macroscopic properties of sheared granular systems, from grain-scale force measurements. Combined with grain-scale displacement measurements, these observations allow us to study a number of important properties of sheared granular systems, and the nature of plastic deformations in amorphous, athermal systems.

Chapter 6

Conclusions and future directions

In this thesis, we have experimentally studied the behavior of 2D granular systems under a variety of conditions. We began our journey by outlining the need for studying granular systems under different boundary conditions. We then argued for a need to experimentally obtain grain-scale contact forces, and proposed a novel method of measuring both the normal and tangential forces. We demonstrated successful implementation of the method. We then proceeded to apply this method to study the distribution of forces, the structure of force chains and correlations between them. We began by studying isotropically compressed, and pure sheared systems. We found significant differences in the force-chain networks and the distribution of normal forces. We also devised a new measure to quantify force chains.

Our next set of experiments dealt with isotropically compressed and sheared systems separately. We studied the issue of jamming transition in isotropically compressed system. We found the jamming point for our system and a discontinuous transition in the average coordination number and the pressure at the jamming point. We also studied sheared systems from the point of view of plastic deformation, and the evolution of the system under cyclic shear. In particular, we studied the stress-strain behavior of the system, and the motion of individual grains. We found that the stress-strain behavior is hysteretic, signifying energy dissipation. We also found vortex patterns in the motion of grains.

We briefly summarize the main results from each experiment below, and present a few ideas about the next stage of development in experimental methods, and some open questions that need to be studied in future.

6.1 Summary of results

6.1.1 Experimental method

We begin by summarizing experimental methods not only because they are novel but also because they represent a significant step forward in terms of the detail with which we can study granular systems. Although restricted to two dimensions, we have been able to measure, for the first time to our knowledge, the normal and the tangential forces in bulk granular systems. We can accomplish this task in an automated fashion with good accuracy on a large number of grains ($\approx$ 1000 grains). We have made use of birefringent disks, which allow us to visualize stresses in the system. The measurement of contact forces is accomplished in a least-squares sense by fitting the plane elasticity model to the observed intensity profile within each disk.

In order to be able to study the response of granular systems to different kinds of boundary loads, we need to have an experimental setup that can impose a variety of boundary conditions precisely, and repeatedly. We built a biaxial test apparatus to accomplish this. It is a simple enclosure with four walls, two of which can be moved independently and precisely. By moving the walls appropriately, we can create states with uniaxial compression, isotropic compression, and pure shear. We use this setup in all our subsequent experiments.

6.1.2 Distribution of contact forces in granular systems

In chapter 3 we study two kinds of systems, isotropically compressed and pure sheared. We apply our method of finding grain-scale contact forces, and obtain the distributions of the normal and the tangential components, for both kinds of systems. We find that the tangential forces are much smaller in magnitude as compared to the normal forces, and their distributions for both isotropically compressed and

sheared systems fall off exponentially. In contrast, the distributions of normal forces show significant differences. The distributions of normal forces for sheared systems have an exponential tail, whereas for isotropically compressed systems they fall off faster than an exponential. We then characterized the spatial organization of force-chain network in each case. We found that sheared systems have long force chains roughly in the principal stress direction. We characterized this spatial distribution of force chains by two-dimensional spatial correlation of magnitudes of forces, and found that sheared systems have long-range almost power-law like correlation in force-chain direction. This is a novel measure that quantifies the qualitative idea of force-chains.

6.1.3 Jamming in isotropically compressed systems

In chapter 4 we study the jamming behavior in isotropically compressed systems. We start with a stress-free system, and find the packing fraction at which the system jams. We find the packing fraction at which the system jams ($\phi_c \approx 0.8422$). We also find a significant rise in the average coordination number of the system as the system goes through the jamming transition ($Z_c = 3.04$). The variation of $Z - Z_c$ shows a power-law increase beyond the jamming point. The exponent of the power-law is around 0.56. We also measure the contact forces in the system, and find the mean pressure. As the system jams, the pressure also shows a clear transition at $\phi \approx 0.8422$. The pressure also shows a power-law increase as a function of $\phi - \phi_c$, with an exponent of 1.1, a value close to that predicted by simulations.

6.1.4 Plastic deformations in sheared systems

In chapter 5 we examine sheared systems from the point of view of plastic deformation. We measure grain-locations, and employ particle tracking to study the motion of grains. We also measure contact forces to obtain the stress-strain behavior of the

system. Using the measured contact forces, we compute the energy of the system at every deformation state and find the energy changes in the system. The stress-strain curve for the entire cycle of forward and reverse shear clearly shows a hysteresis loop. The stress-strain curve has elastic segments of linearly increasing stress interrupted by drops in stress, signifying plastic failure events. The displacement profile of the particles also shows interesting features. The displacement during the forward shear portion has two homogeneously moving regions in the upper-left, and lower-right corners of the image, and diagonally across the image we can see well-formed vortices. This pattern is abruptly destroyed upon reversing the shear, and the profile looks more quadratic. These observations are qualitatively similar to some recent numerical, and theoretical studies.

6.2 Future directions

We have made a beginning in studying granular systems at the grain-scale. Although we have been able to find some new results, and an improved understanding of a small number of issues, the task has just begun. Many more questions remain to be answered, and *can* be answered using the techniques developed in this thesis. Progress can be made on two fronts; on the one hand, each of the systems described, can be studied in further detail by exploring aspects that have not been analyzed, and on the other hand, experimental techniques can be improved even further, which in turn will bring more questions that *can* be investigated within reach. We will outline some directions regarding both issues, which are feasible in near future.

6.2.1 Open questions in granular physics

let us outline some outstanding questions, and some avenues that have been opening up due to recent advances in theoretical, numerical, and experimental progress:

- The distributions of forces for sheared, and isotropically compressed states need to be investigated further. We need more experimental data at the low-force end to ascertain the behavior of these distributions completely.

- Although we know that the distribution of contact forces in isotropically compressed systems falls off faster than an exponential, we do not know its exact nature. Is it Gaussian? Or is it some other function? Does it depend on the system size? How does the functional form of the distribution change with compression? These are some of the questions that can be answered upon more investigation.

- For both sheared and compressed systems, *quantitative* characterization of the force-chain networks has just begun. We need more study to ascertain the changes in the force-chain networks due to increasing compression, and shear. For example many quasi-static, and dynamic phenomena show interesting formation and break-up of force chains.

- A related theme is whether or not the force-chain networks can be modelled by percolation models, or graph theoretic models. An experimental study of this issue is being carried out by John Wambaugh, a fellow graduate student.

- The phenomenon of jamming is complicated. The inter-grain forces at the jamming transition are quite low. As discussed earlier, this is the region that needs more attention and study, in order to get a clearer understanding of the problem.

- The jamming behavior, in all likelihood, will turn out to be different for isotropically compressed and sheared systems. A study of jamming transition similar to the one presented in this thesis can be done for the sheared systems.

- Our study of plastic deformation in sheared systems has revealed some interesting features. More analysis can reveal whether we can capture units of shear Transformation Zones or not. Moreover, the correlation between plastic deformation, and shear-induced anisotropy has yet to be studied. Probing these issues can help in improving our understanding of plastic failure events.

- A longstanding problem in granular systems is the response of the system to small perturbations, or finding the "Green's function" for the system. The experimental setup, and the force measurement technique we have developed can be used effectively to obtain such a response function for both isotropic, and anisotropic stress states.

- returning to a general theme, all of our experiments have been performed on very soft particles. We have not established how does particle elasticity affect any of the effects observed in our experiments. We can study these effects by using harder particles, which are also closer to many numerical simulations, and theoretical studies.

6.2.2 Improvements in experimental methods

The experimental improvements proposed here are based on the questions raised above, and our experience about the limitations of the experimental approach outlined in this thesis. As mentioned in the previous section, we may need to extend our experiments to include harder particles. Also, the issue of low-force measurements needs consideration. Accurate measurements of low forces requires a material with more sensitive stress-optic response.

During the course of experiments presented in this thesis, we have encountered an issue, which somewhat limits our scope of analyses, and was mentioned in chapter 4. At the very low-force end, during compression or shear, we encounter a very small but

noticeable induced-shear effect. When the grains are about to touch each other, the packing fraction of the system is low. In this regime, there are two effects of moving the boundary walls of the biaxial test apparatus; one effect is meso-scale frozen-in stresses, and the other effect is a lag in the transmission of the effects of moving a boundary to the bulk sample. Both issues are related and possibly have a common cause.

The meso-scale frozen-in stresses refer to small fragments of force-chains, which can not be removed by tapping or other mechanisms. This happens most frequently near the boundaries of the system, and could be due to locally enhanced packing fraction. It results in a slightly anisotropic stress state.

The transmission of the effects of moving a boundary do not reach the bulk system until a sufficiently dense packing has been reached. If we start from an initial stress-free state, some amount of compression goes towards compaction of the system, which again is most prominant at the boundaries, which in turn causes small fragments of force-chains locally.

One cause common to both these effects could be friction between the disks and the Plexiglas base, which although not high is not negligibly small. It is most noticeable, and pertinent when the overall stress is the system is very low; precisely the kinds of situations described above. In low packing fraction states when a wall is moved, ideally the grains near the boundary should start moving and come to rest only when they are stopped by collisions with other grains, and so on for every subsequent layer of grains. This would result in the effects wall-motion being carried all the way to the bulk system. This does not happen in our experimental system due to friction with the base. The grains near the wall move but stop before coming in contact with any other grain.

We have planned for an improvement in the experimental setup, and a change

in the material of our model granular system, which removes the above mentioned problems all at once. In the next version of the experimental setup, we intend to completely remove friction with the base by levitating the disks on a substrate with air cushion, much like an air-hockey table. This would be accomplished by replacing the Plexiglas base with a porous board and supplying pressurized air through it. It would ensure that the grains behave exactly as described in the ideal case, and would remove problems of frozen-in force-chain fragments, and transmission of wall-motion to the bulk system.

A fall out of changing the base to a non-transparent material is that our current method of transmission photoelasticity no longer works. We need to switch to *reflection photoelasticity*, where polarized light is reflected off of a material with metallic backing, so that the same effect is accomplished, but with reflected light. The disks we will use will have reflective backing, and the available material (Vishay Measurements, PS-1) is stress-optically around 15 times more sensitive, and 700 times harder than our present material. This new material is ideal for low-force measurements, and is much closer to realistic hard grains.

Combining both these improvements would result in hard grains, with a high stress-optic sensitivity, floating on a frictionless surface, a situation very close to numerical simulations and theoretical models!

In conclusion, with the help of the improvements outlined above, combined with the existing contact force measurement technique, future students could investigate many of the open questions posed earlier, and I wish them happy investigating!

Chapter 7

APPENDIX

In this appendix, we sketch the relevant formulations of the elasticity theory needed in order to obtain the solution for the stresses in a disk under concentrated loads. We need to begin with two-dimensional (2D) elasticity theory, give the solution to the half-plane problem and then proceed to give the solution to the disk problem.

In order to solve for the stresses or strains within a stationary elastic solid subjected to boundary forces, several additional conditions need to be met:

- Condition of equilibrium: The boundary forces and tractions must balance each other, and the body must be in static equilibrium
- Constitutive relation: The relashionship between the stresses and strains must be known.
- Compatibility condition: The deformations and strains must preserve the continuity of the solid.

For an elastic solid where either the stresses or the strains are negligible in the third dimension, we have the so-called *plane stress* and *plane strain* situation respectively. The plane stress situation is applicable to thin disk problem, whereas the plane strain approximation is more suitable for a long cylinder loaded axially.

In two dimensions, the stress tensor has three independent components, σ_{xx}, σ_{yy}, and σ_{xy}. The complete stress tensor is:

$$\sigma = \begin{pmatrix} \sigma_{xx} & \sigma_{xy} \\ \sigma_{yx} & \sigma_{yy} \end{pmatrix}. \tag{7.1}$$

The condition of equilibrium is given by:

$$\begin{cases} \partial_x \sigma_{xx} + \partial_y \sigma_{xy} + F_x &= 0 \\ \partial_x \sigma_{xy} + \partial_y \sigma_{yy} + F_y &= 0 \end{cases} \tag{7.2}$$

Alongwith the equilibrium conditions, for a 2D linear elastic solid, if there are no body forces like gravity, the compatibility conditions for stresses are:

$$(\partial_x^2 + \partial_y^2)(\sigma_{xx} + \sigma_{yy}) = 0 \tag{7.3}$$

These equations apply equally to plane stress and plane strain problems, and they do not contain any material constants. The solution of any 2D problem can now be attempted by knowing the boundary loads.

G. B. Airy introduced a function *stress function* $\Phi(x, y)$, which identically satisfies the equilibrium conditions. The stress function is related to the stresses as:

$$\begin{aligned} \sigma_{xx} &= \partial_y^2 \Phi \\ \sigma_{yy} &= \partial_x^2 \Phi \\ \sigma_{xy} &= \partial_x \partial_y \Phi \end{aligned} \tag{7.4}$$

Substituting equation 7.4 in equation 7.3 yields:

$$\frac{\partial^4 \Phi}{\partial^4 x} + \frac{\partial^4 \Phi}{\partial^2 x \partial^2 y} + \frac{\partial^4 \Phi}{\partial^4 y} = 0 \tag{7.5}$$

The Airy stress function satisfies the bi-harmonic equation, and is most commonly used to solve a particular problem. There are very few problems that can be solved by directly integrating the bi-harmonic equation. A more common strategy is to make an educated guess for Φ, or use symmetries of the problem to find a stress

function that will satisfy equation 7.5 and the boundary conditions; much like the 2D fluid flow problems of flow around objects of complex geometrical shapes. Another approach used often is to start with partial solutions from a known and solved problem, and adjust the solution for the boundary conditions under consideration. This approach, for example, has been used repeatedly, whenever the solution of the half-plane problem can be used as a starting guess.

There are direct methods though, of solving equation 7.5. One method is to try polynomial solutions and fix the coefficients so that the equation is satisfied. The other approach is to use Fourier series, and find the coefficients in the series by integration.

7.1 Half plane

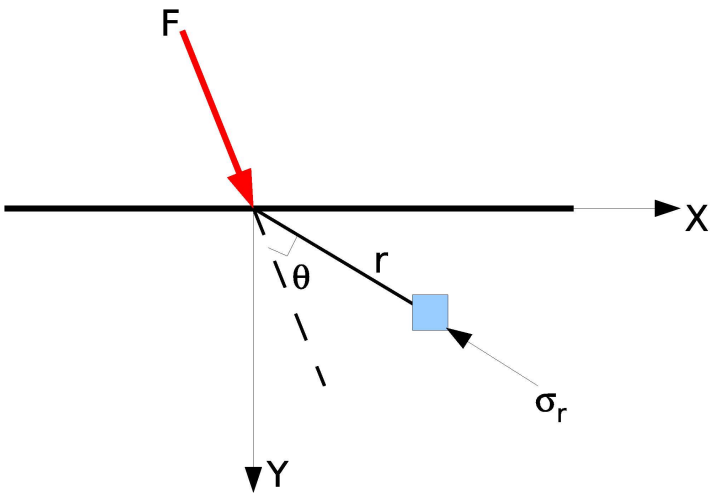

Figure 7.1: Line load on a semi-infinite half plane.

Consider a line force F acting on a semi-infinite plane, as shown in Figure 7.1. Consider an area element within the solid, at a distance r from the point of the application of the force, and at an angle θ *from the direction of the application of the*

force. The Cartesian coordinate system is as shown.

For the case of half plane, it is advantageous to solve the bi-harmonic equation in polar coordinates. We assume the solution to be $\Phi = cFr\theta \sin\theta$, where c is a constant. This form of Φ satisfies the compatibility condition, and from equilibrium equations we have:

$$\sigma_{rr} = \frac{2cF\cos\theta}{r}, \qquad \sigma_{\theta\theta} = 0, \qquad \sigma_{r\theta} = 0 \tag{7.6}$$

The force acting on any volume element at a distance r must be equal to the applied force. Therefore, the boundary conditions become:

$$\sigma_{\theta\theta} = 0, \qquad \sigma_{r\theta} = 0, \qquad \theta = \pm\frac{\pi}{2} \tag{7.7}$$

$$2\int_0^{\frac{\pi}{2}} (\sigma_{rr}\cos\theta) r d\theta = -F \tag{7.8}$$

Substituting equation 7.6 in the above equation, we get:

$$4cF\int_0^{\frac{\pi}{2}} \cos^2\theta d\theta = -F \tag{7.9}$$

Integrating the equation gives $c = -\frac{1}{\pi}$. Substituting the value of c in equation 7.6 gives for the radial stress,

$$\sigma_{rr} = -\frac{2F}{\pi}\frac{\cos\theta}{r} \tag{7.10}$$

The Cartesian components of the radial stress in the XY axes shown in Figure 7.1 are given by:

$$\begin{aligned}
\sigma_{xx} &= -\frac{2F}{\pi}\frac{y^3}{(x^2+y^2)^2} \\
\sigma_{yy} &= -\frac{2F}{\pi}\frac{yx^2}{(x^2+y^2)^2} \\
\sigma_{xy} &= -\frac{2F}{\pi}\frac{y^2x}{(x^2+y^2)^2}
\end{aligned} \tag{7.11}$$

This completes the solution for a line load on a semi-infinite plane. Two noteworthy points are:

- The contours of equal stress are circles with diameter d that have the X axis as a tangent, and their centers are on the Y axis. The stress on these circles is $\sigma_{rr} = -\frac{2F}{\pi d}$.
- The direction of the application of the force does not have to be normal; the angle to an area element is measured with respect to the direction of the force. This property is used in deriving the solution to the disk problem.

7.2 Solution to the disk problem

Consider a disk with arbitrary number of forces acting on it as shown in Figure 7.2, each having arbitrary magnitude and arbitrary direction. This is the most general case that can be constructed for a 2D disk problem. The only condition on the forces is that both components of forces are balanced, and the torques are balanced.

The disk problem again is no solved most fruitfully by direct methods but by starting with a partial solution; in this case the half plane solution outlined above. Each force is considered independently, and the stress field due to each force is assumed to be of the same form as the radial stress of the half plane problem. It is clear

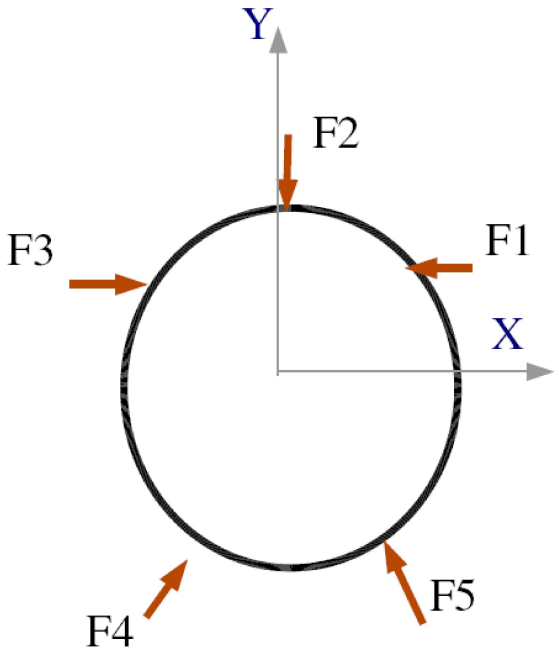

Figure 7.2: Schematic diagram of a disk under concentrated loads.

that the disk problem has different boundary conditions and different symmetries, therefore we will need to adjust the solution so as to match all boundary conditions.

The key difference here is that the circumference of the disk is stress-free except at the points of application of forces. In the half plane problem, there was only one force acting at one point and the boundary was flat. Here there are several forces, and the arc segments between these load points are stress free.

The general solution follows exactly along the lines of a disk acted on by forces along a chord, which is not the diameter of the disk. A consideration of a single force tells us what the additional factor should be. The situation is illustrated in Figure 7.3. We assume a radial stress solution of the same form as the half plane. At point M on the circumference, the compressive load is $(\frac{2F}{\pi})\frac{\cos\theta_1}{r_1}$, along the direction AM. Let O be the origin of polar coordinates, and the distances and angles are measured as shown in Figure 7.3. The stress acting on the the element tangential to the boundary at point M can be calculated from observing that the angle between the normal MO

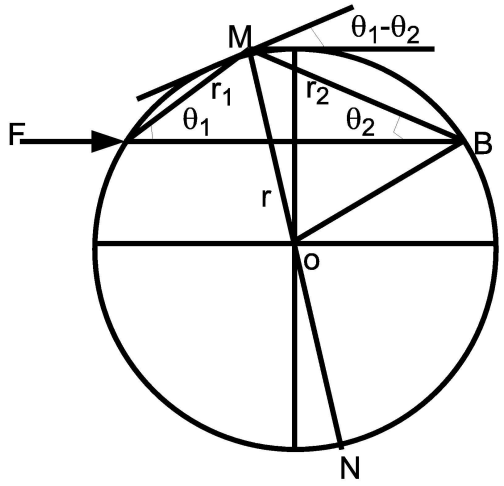

Figure 7.3: Point force on a disk along a chord.

to the element and the direction r_1 is $\frac{\pi}{2} - \theta_2$. Then we use the formula for the projection of stress along any direction θ:

$$\sigma_r = \sigma_{rr} \cos^2 \theta \tag{7.12}$$

$$\sigma_\theta = \sigma_{rr} \sin \theta \cos \theta \tag{7.13}$$

To find the normal and the tangential components at M, we substitute $\frac{\pi}{2} - \theta_2$ for θ, and obtain:

$$\sigma_{rr} = -\frac{2F}{\pi} \frac{\cos \theta_1}{r_1} \sin^2 \theta_2 \tag{7.14}$$

$$\sigma_{r\theta} = -\frac{2F}{\pi} \frac{\cos \theta_1}{r_1} \sin \theta_2 \cos \theta_2 \tag{7.15}$$

From the triangle AMN, $r_1 = d \sin \theta_2$, where d is the diameter of the disk, the above equations can be written as:

$$\sigma_{rr} = -\frac{F}{\pi d} \sin (\theta_1 + \theta_2) - \frac{F}{\pi d} \sin (\theta_2 - \theta_1) \tag{7.16}$$

$$\sigma_{r\theta} = -\frac{F}{\pi d} \cos (\theta_1 + \theta_2) - \frac{F}{\pi d} \cos (\theta_2 - \theta_1) \tag{7.17}$$

This is the stress acting on the boundary element at M. It can be considered as a superposition of three stresses:

- A normal stress uniformly distributed along the boundary:

$$-\frac{F}{\pi d}\sin(\theta_1+\theta_2) \tag{7.18}$$

- A shearing stress uniformly distributed along the boundary:

$$-\frac{F}{\pi d}\cos(\theta_1+\theta_2) \tag{7.19}$$

- A stress whose normal and tangential components are:

$$-\frac{F}{\pi d}\sin(\theta_2-\theta_1) \quad and \quad -\frac{F}{\pi d}\cos(\theta_2-\theta_1) \tag{7.20}$$

The angle between the force F and the tangent at M is $\theta_1 - \theta_2$, therefore the stresses in equation 7.20 are of magnitude $\frac{F}{\pi d}$, and act in the direction opposite to the direction of force F.

Now if we have a number of forces acting on a disk in static equilibrium, we assume as before that each of them produces a radial stress distribution. Then the stresses that need to be applied at the boundary in order to maintain such a stress distribution are, from equation 7.18, equation 7.19, and equation 7.20:

- A normal stress uniformly distributed along the boundary:

$$-\sum\frac{F}{\pi d}\sin(\theta_1+\theta_2) \tag{7.21}$$

- A shearing stress uniformly distributed along the boundary:

$$-\sum\frac{F}{\pi d}\cos(\theta_1+\theta_2) \tag{7.22}$$

- A stress whose intensity and direction is obtained by the vector sum of expressions equation 7.20, where the summation is over all the forces on the boundary.

where, $\sum$ is the sum over all the forces acting on the disk.

Now the sum of the torques with respect to the center of the disk, due to all the forces is given by:

$$\sum \frac{F \cos(\theta_1 + \theta_2) d}{2}, \tag{7.23}$$

which is zero due to torque balance, which in turn means that the tangential stresses equation 7.22 are zero. Also the third contribution to the stresses, the vector sum of equation 7.20 is zero due to force balance. Therefore we are left with only one additional term, equation 7.21. The effect of this term can be nullified by adding a uniform *tension* of magnitude:

$$\sum \frac{F}{\pi d} \sin(\theta_1 + \theta_2) \tag{7.24}$$

to the sum of radial distributions. In the end, the total stress field inside the disk due to *any number of arbitrary forces* is given by:

$$\sigma_{rr} = -\sum_i \frac{2F_i}{\pi} \frac{\cos\theta_i}{r_i} + \sum_i \frac{F_i}{\pi d} \sin(\theta_1 + \theta_2)_i \tag{7.25}$$

$$\sigma_{r\theta} = 0 \tag{7.26}$$

Bibliography

[ABT+03] S. Adichtchev, T. Blochowicz, C. Tschirwitz, V. N. Novikov, and E. A. Rössler, *Reexamination of the evolution of the dynamic susceptibility of the glass former glycerol*, Phys. Rev. E **68** (2003), 011504.

[AD94] Y. A. Andrienko and M. S. Dubovikov, *Optical tomography of tensor fields: the general case*, J. Opt. Soc. Am. **A** (1994), no. 11, 1628–1631.

[ADG92] Y. A. Andrienko, M. S. Dubovikov, and A. D. Gladun, *Optical tomography of a birefringent medium*, J. Opt. Soc. Am. **A** (1992), no. 9, 1761–1764.

[AHT00] J. A. Åström, H. J. Herrmann, and J. Timonen, *Granular packings and fault zones*, Phys. Rev. Lett. **84** (2000), no. 4, 638–641.

[AK78] A.S. Argon and H.Y. Kuo, *The structure of, and plastic flow in a bragg bubble glass*, Rapidly Quenched Metals III **II** (1978//), 269 – 76 (English).

[Amo99] G. Amontons, *De la resistance causee par les machines.*, Mémoires de l'Academie Royale A **12** (1699), 257.

[Arg82] A. S. Argon, *Mechanisms of inelastic deformation in metallic glasses.*, Journal of Physics and Chemistry of Solids **43** (1982), no. 10, 945 – 961 (English).

[Arg01] A.S. Argon, *Plastic deformation in metallic glasses*, Acta Metallurgica **27** (1979/01/), no. 1, 47 – 58 (English).

[AS82] A. S. Argon and L. T. Shi, *Analysis of plastic flow in an amorphous soap bubble raft by the use of an inter-bubble potential.*, Philosophical Magazine A: Physics of Condensed Matter, Defects and Mechanical Properties **46** (1982), no. 2, 275 – 294.

[AS04] A.S. Argon and L.T. Shi, *Development of visco-plastic deformation in metallic glasses*, Acta Metall. (USA) **31** (1983/04/), no. 4, 499 – 507 (English).

[BCC95] J.P. Bouchaud, M.E. Cates, and P. Claudin, *Stress distribution in granular media and nonlinear wave equation*, Journal de Physique I **5** (1995), 639.

[BJ97] R.P. Behringer and J.T. Jenkins (eds.), Powders and Grains 97, Balkema, Rotterdam, The Netherlands, Kluwer Academic Publishers, 1997.

[BPC04] Cambou B., Dubujet Ph., and Nouguier-Lehon C., *Anisotropy in granular materials at different scales*, Mechanics of Materials **36** (2004), no. 12, 1185–1194.

[BWS+05] Jasna Brujic, Ping Wang, Chaoming Song, David L. Johnson, Olivier Sindt, and Hernan A. Makse, *Granular dynamics in compaction and stress relaxation*, Physical Review Letters **95** (2005), no. 12, 128001.

[CBCW98] P. Claudin, J.-P. Bouchaud, M.E. Cates, and J.P. Wittmer, *Models of stress fluctuations in granular media*, Phys. Rev. E **57** (1998), 4441.

[Che97] T.Y Chen, *Digital determination of photoelastic birefringence using two wavelengths*, Experimental Mechanics **37** (1997), 232–236.

[CL31] E.G. Coker and L.N.G.Filon, *A treatise on photoelasticity*, Cambridge University Press, New York, 1931.

[CLFB+06] Xiang Cheng, Jeremy B. Lechman, Antonio Fernandez-Barbero, Gary S. Grest, Heinrich M. Jaeger, Greg S. Karczmar, Matthias E. Mobius, and Sidney R. Nagel, *Three-dimensional shear in granular flow*, Physical Review Letters **96** (2006), no. 3, 038001.

[CLM+96] S. N. Coppersmith, C.-h. Liu, S. Majumdar, O. Narayan, and T. A. Witten, *Model for force fluctuations in bead packs*, Phys. Rev. E **53** (1996), no. 5, 4673–4685.

[Cou76] C.A. Coulomb, *Sur une application des regles de maximis and minimis a queques problèmes de statique relatifs a l'architecture*, Mémoires de Math. de l'Acad. Royale des Sciences (1776), 343.

[CWBC98] M. E. Cates, J. P. Wittmer, J.-P. Bouchaud, and P. Claudin, *Development of stresses in cohesionless poured sand*, Phil. Trans. R. Soc. Lond. A **356** (1998), 2535–2560.

[Dan57] P. Dantu, *Contribution a l'etude mecanique et geometrique des milieux pulverulents*, Proc. Of the 4th International Conf. On Soil Mech. and Foundation Eng. **1** (1957), 144.

[DB05] Karen E. Daniels and Robert P. Behringer, *Hysteresis and competition between disorder and crystallization in sheared and vibrated granular flow*, Physical Review Letters **94** (2005), no. 16, 168001.

[DdJdJ72a] A. Drescher and G. de Josselin de Jong, *Photoelastic verification of a mechanical model for the flow of a granular material*, J. Mech. Phys. Solids **20** (1972), 337–351.

[DDJdJ72b] A. Drescher and G. De-Josselin-de Jong, *Photoelastic verification of a mechanical model for the flow of a granular material*, Journal of the Mechanics and Physics of Solids **20** (1972), 337.

[dG98] P.-G. de Gennes, *Reflections on the mechanics of granular matter*, Physica A **261** (1998), 267–293.

[DR65] A.J. Durelli and W.F. Riley, *Introduction to photomechanics*, Prentice-Hall, Inc., 1965.

[DSR00] M. Da Silva and J. Rajchenbach, *Stress transmission through a model system of cohesionless elastic grains*, Nature **406** (2000), 708.

[DTS05] A. Donev, S. Torquato, and F. H. Stillinger, *Pair correlation function characteristics of nearly jammed disordered and ordered hard-sphere packings*, Phys. Rev. E **71** (2005), 011105.

[DW83] A.J. Durelli and D. Wu, *Use of coefficients of influence to solve some inverse problems in plane elasticity*, Transactions of the ASME. Journal of Applied Mechanics **50** (1983), 288.

[DX93] S.G. Paikowsky K.J. DiRocco and F. Xi, *Interparticle contact ofrce analysis and measurements using photoelastic techniques*, 2nd Int. Conference on Discrete Element Methods, March 18-19, 1993, IESL (MIT), 1993, pp. 449–461.

[EGD94] B.J. Ennis, J. Green, and R. Davies, *The legacy of neglect in the United States*, Chemical Engineering Progress **90** (1994), 32.

[Eib84] J. Eibl, *Design of silos – pressures and explosions*, The Structural Engineer **62A** (1984), 169.

[EMJN02] J. Michael Erikson, Nathan W. Mueggenburg, Heinrich M. Jaeger, and Sidney R. Nagel, *Force distributions in three-dimensional compressible granular packs*, Phys. Rev. E **66** (2002), no. 4, 040301.

[FL98] M Falk and J Langer, *Dynamics of viscoplastic deformation in amorphous solids*, Physical Review E **57** (1998), no. 6, 7192.

[Fro41] M.M. Frocht, *Photoelasticity, vol. i & ii*, John Wiley & Sons, New York, 1941.

[GG02] C. Goldenberg and I. Goldhirsch, *Force chains, microelasticity, and macroelasticity*, Physical Review Letters **89** (2002), 084302.

[GG03] ———, *Small and large scale granular statics*, Granular Matter **6** (2003), 87–97.

[GHL+01] Junfei Geng, D. Howell, E. Longhi, R.P. Behringer, G. Reydellet, L. Vanel, E. Clement, and S. Luding, *Footprints in sand: the response of a granular material to local perturbations*, Physical Review Letters **87** (2001), 035506/1.

[GLBH01] Junfei Geng, Emily Longhi, R.P. Behringer, and D.W. Howell, *Memory in two-dimensional heap experiments*, Physical Review E **64** (2001), 060301/1.

[God90] J. D. Goddard, *Nonlinear elasticity and pressure-dependent wave speeds in granular media*, Proc. R. Soc. London Ser. A **430** (1990), 105.

[Gre83] William B. Green, *Digital image processing : a systems approach*, Van Nostrand Reinhold Co., New York, 1983.

[Har40] J. P. Den Hartog, *Photoleasticity*, Science **92** (1940), no. 2391, 382.

[HB99] D. Howell and R. P. Behringer, *Fluctuations in a 2d granular Couette experiment: A critical transition*, Phys. Rev. Lett. **82** (1999), 5241.

[HB03] R. R. Hartlet and R. P. Behringer, *Logarithmic rate dependence of force networks in sheared granular materials*, Nature **421** (2003), 928–931.

[HBV99] D. Howell, R.P. Behringer, and C. Veje, *Stress fluctuations in a 2D granular couette experiment: A continuous transition*, Physical Review Letters **82** (1999), 5241.

[Her82] H. Hertz, *Über die berührung fester elastischer Körper*, J. für die reine u. angew. Math **92** (1882), 136.

[Hey52] R.B. Heywood, *Designing by photoelasticity*, Chapman and Hall Ltd., London, 1952.

[HJS96] Heinrich Hertz, D. E. Jones, and G. A. Schott, *Miscellaneous paper by heinrich hertz*, Macmillan and Company, New York, 1896.

[How99] D.W. Howell, *Stress distributions and fluctuations in static and quasi-static granular systems*, Ph.D. thesis, Duke University, 1999.

[Jan95] H.A. Janssen, *Getreidedruck in silozellen*, Zeits Vereins Deutch Ing. **39** (1895), 1045–1049.

[JNB96a] H. M. Jaeger, S. R. Nagel, and R. P. Behringer, *Granular solids, liquids, and gases*, Reviews of Modern Physics **68** (1996), no. 4, 1259–1273.

[JNB96b] H.M. Jaeger, S.R. Nagel, and R.P. Behringer, *Granular solids, liquids, and gases*, Reviews of Modern Physics **68** (1996), 1259.

[LGSP03] James W. Landry, Gary S. Grest, Leonardo E. Silbert, and Steven J. Plimpton, *Confined granular packings: Structure, stress, and forces*, Physical Review E (Statistical, Nonlinear, and Soft Matter Physics) **67** (2003), no. 4, 041303.

[LL70a] L. Landau and E. Lifschitz, *Theory and elasticity, 2nd edition*, Pergammon Press, New York, 1970.

[LL70b] L. D. Landau and E. M. Lifshit, *Theory of elasticity, 2rd edition*, Pergamon Press, Oxford, 1970.

[LMF99] Grunde Løvoll, Knut Jørgen Måløy, and Eirik G. Flekkøy, *Force measurements on static granular materials*, Phys. Rev. E **60** (1999), no. 5, 5872–5878.

[LN98] A.J. Liu and S.R. Nagel, *Jamming is not just cool any more*, Nature **396** (1998), 21.

[LNS+95] C.-h. Liu, S. R. Nagel, D. A. Schecter, S. N. Coppersmith, S. Majumdar, O. Narayan, and T. A. Witten, *Force fluctuations in bead packs*, Science **269** (1995), 513.

[MB05] T. S. Majmudar and R. P. Behringer, *Contact force measurements and stress-induced anisotropy in granular systems*, Nature **435** (2005), 1079–1082.

[MGJS04] H. A. Makse, N. Gland, D. L. Johnson, and L. Schwartz, *Granular packings: Nonlinear elasticity, sound propagation, and collective relaxation dynamics*, Phys. Rev. E **70** (2004), 061302.

[MJN98] D. M. Mueth, H. M. Jaeger, and S. R. Nagel, *Force distribution in a granular medium*, Phys. Rev. E. **57** (1998), no. 3, 3164–3169.

[ML04a] Craig Maloney and Anael Lemaitre, *Subextensive scaling in the athermal, quasistatic limit of amorphous matter in plastic shear flow*, Physical Review Letters **93** (2004), no. 1, 016001.

[ML04b] ———, *Universal breakdown of elasticity at the onset of material failure*, Physical Review Letters **93** (2004), no. 19, 195501.

[MMFJ64] J.H. Mickell, A.G.M. Michell, F.W.Niedenfuhr, and J.R.M.Radok, *The collected mathematical works of j.h. and a.g.m. michell*, P. Noordhoff Ltd., Groningen, The Netherlands, 1964.

[MOB96] B. Miller, C. O'Hern, and R. P. Behringer, *Stress fluctuations for continuously sheared granular materials*, Phys. Rev. Lett. **77** (1996), 3110–3113.

[MRS90] C. Marone, C.B. Raleigh, and C.H. Scholz, *Frictional behavior and constitutive modeling of simulated fault gouge*, Journal of Geophysical Research **95** (1990), 7007.

[Ned92] R.M. Nedderman, Statics and Kinematics of Granular Materials, Cambridge Univ. Press, Cambridge, 1992.

[Nic98] M. Nicodemi, *Force correlations and arch formation in granular assemblies*, Physical Review Letters **80** (1998), 1340.

[OLLN02] C.S. O'Hern, S. A. Langer, A. J. Liu, and S. R. Nagel, *Random packings of frictionless particles*, Phys. Rev. Lett. **88** (2002), 075507.

[OSLN03] C.S. O'Hern, L. E. Silbert, A. J. Liu, and S. R. Nagel, *Jamming at zero temperature and zero applied stress: The epitome of disorder*, Phys. Rev. E **68** (2003), 011306.

[PBF+91] W. Petry, E. Bartsch, F. Fujara, M. Kiebel, H. Sillescu, and B. Farago, *Dynamic anomaly in the glass transition region of orthoterphenyl. a neutron scattering study*, Z. Phys. B **83** (1991), 175–184.

[Per98] B. N. J. Persson, *Sliding friction: Physical principles and applications*, Springer Verlag, Berlin, 1998.

[PFTV92] W. H. Press, B. P. Flannery, S. A. Teukolsky, and W. T. Vetterling, *Numerical recipes in c: The art of scientific computing, 2nd edition*, Cambridge University Press, Cambridge, 1992.

[Ram00] K. Ramesh, *Digital photoelasticity: Advanced techniques and applications*, Springer-Verlag, Berlin Heidelberg, Germany, 2000.

[RC01] G. Reydellet and E. Clement, *Green's function probe of a static granular piling*, Physical Review Letters **86** (2001), 3308.

[RJMR96a] F. Radjai, M. Jean, J.-J. Moreau, and S. Roux, *Force distributions in dense two-dimensional granular systems*, Physical Review Letters **77** (1996), 274.

[RJMR96b] ———, *Force distributions in dense two-dimensional granular systems*, Physical Review Letters **77** (1996), 274.

[Rus99] John C. Russ, *The image processing handbook, 4th edition*, CRC Press, Boca Raton, FL, USA, 1999.

[RWJM98] F. Radjai, D.E. Wolf, M. Jean, and J.-j. Moreau, *Bimodal character of stress transmission in granular packings*, Physical Review Letters **80** (1998), 61.

[Sav97] S. B. Savage, *Problems in the statics and dynamics of granular materials*, Powders & Grains 97 (R. P. Behringer and J. T. Jenkins, eds.), Balkema, Rotterdam, 1997, pp. 185–194.

[SEG+02] L. E. Silbert, D. Ertaş, G. S. Grest, T. C. Halsey, and D. Levine, *Geometry of frictionless and frictional sphere packings*, Phys. Rev. E **65** (2002), 031304.

[SEVvH06] Jacco H. Snoeijer, Wouter G. Ellenbroek, Thijs J. H. Vlugt, and Martin van Hecke, *Sheared force networks: Anisotropies, yielding, and geometry*, Physical Review Letters **96** (2006), no. 9, 098001.

[SGL02] Leonardo E. Silbert, Gary S. Grest, and James W. Landry, *Statistics of the contact network in frictional and frictionless granular packings*, Phys. Rev. E **66** (2002), no. 6, 061303.

[SN85] A. Shukla and H. Nigam, *A numerical-experimental analysis of the contact stress problem*, Journal of Strain Analysis for Engineering Design **20** (1985), 241.

[Soc98] J. E. S. Socolar, *Average stresses and force fluctuations in non-cohesive granular materials*, Phys. Rev. E. **57** (1998), no. 3, 3204–3215.

[SRS+05] E. Somfai, J.N. Roux, J. H. Snoeijer, M. van Hecke, and W. Van Saarloos, *Elastic wave propagation in confined granular systems*, Phys. Rev. E **72** (2005), 021301.

[SVE+04] Jacco H. Snoeijer, Thijs J. H. Vlugt, Wouter G. Ellenbroek, Martin van Hecke, and J. M. J. van Leeuwen, *Ensemble theory for force networks in hyperstatic granular matter*, Physical Review E (Statistical, Nonlinear, and Soft Matter Physics) **70** (2004), no. 6, 061306.

[SvHSvS03] Jacco H. Snoeijer, Martin van Hecke, Ellak Somfai, and Wim van Saarloos, *Force and weight distributions in granular media: Effects of contact geometry*, Physical Review E (Statistical, Nonlinear, and Soft Matter Physics) **67** (2003), no. 3, 030302.

[SVvHvS04] Jacco H. Snoeijer, Thijs J. H. Vlugt, Martin van Hecke, and Wim van Saarloos, *Force network ensemble: A new approach to static granular matter*, Physical Review Letters **92** (2004), no. 5, 054302.

[TG70] Stephen P. Timoshenko and J. N. Goodier, *Theory of elasticity, 3rd edition*, McGraw-Hill, New York, 1970.

[TSS+05] Brian P. Tighe, Joshua E. S. Socolar, David G. Schaeffer, W. Garrett Mitchener, and Mark L. Huber, *Force distributions in a triangular lattice*

of rigid bars, Physical Review E (Statistical, Nonlinear, and Soft Matter Physics) **72** (2005), no. 3, 031306.

[TVCR98] Olivier Tsoungui, Denis Vallet, Jean-Claude Charmet, and Stéphane Roux, *ıpartial pressuresȷ supported by granulometric classes in polydisperse granular media*, Phys. Rev. E **57** (1998), no. 4, 4458–4465.

[TWLB02] A. Tanguy, J. P. Wittmer, F. Leonforte, and J.-L. Barrat, *Continuum limit of amorphous elastic bodies: A finite-size study of low-frequency harmonic vibrations*, Phys. Rev. B **66** (2002), no. 17, 174205.

[VC99] L. Vanel and E. Clément, *Pressure screening and fluctuations at the bottom of a granular column*, European Physical Journal B **11** (1999), 525.

[VCB+00] L. Vanel, Ph. Claudin, J.-Ph. Bouchaud, M.E. Cates, E. Clément, and J.P. Wittmer, *Stresses in silos: comparison between theoretical models and new experiments*, Physical Review Letters **84** (2000), 1439.

[VHB99] C. T. Veje, D. W. Howell, and R. P. Behringer, *Kinematics of a 2D granular Couette experiment*, Phys. Rev. E **59** (1999), 739.

[VHC+99] Loic Vanel, Daniel Howell, D. Clark, R. P. Behringer, and E. Clément, *Memoris in sand: experimental tests of construction history on stress distributions under sandpiles*, Phys. Rev. E **60** (1999), no. 5, 5040–5043.

[vN81] J. Šmid and J. Novosad, *Pressure distribution under heaped bulk solids*, I. Chem. E. Symposium Series **63** (1981), D3/V/1–12.

[WCC97] J.P. Wittmer, M.E. Cates, and P. Claudin, *Stress propagation and arching in static sandpiles*, Journal de Physique I **7** (1997), 39.

[YN96] Y. Yang and K. A. Nelson, *Impulsive stimulated thermal scattering study of α relaxation dynamics and the debye-waller factor anomaly in* ca0.4k0.6(NO3)1.4, J. Chem. Phys. **104** (1996), 5429–5436.

[ZM05] H. P. Zhang and H. A. Makse, *Jamming transition in emulsions and granular materials*, Physical Review E (Statistical, Nonlinear, and Soft Matter Physics) **72** (2005), no. 1, 011301.

Biography

Trushant Majmudar was born on September 23, 1971, in Mumbai, India. He spent his school years in Mumbai. He graduated from Mithibai College, Bombay University in 1993, with a specialization in Physics. He began his Mastres in Physics at University of Pune, India, in 1993 and earned his Mastres in 1995.

He then, continued in University of Pune, to pursue his Ph. D in Physics, and nonlinear dynamics in particular, under the guidance of Professor R. E. Amritkar. He left the program in 1998 and came to the United states to pursue his Ph. D. first at Northeastern University. He transferred to Duke University in the summer of 2000 to pursue his Ph. D. at Duke. He joined Professor Bob Behringer's lab and started studying granular physics. He has developed a novel system of measurement to find grain-scale contact forces in a granular system, and used it to study the behavior of granular systems under isotropic compression and shear.

Current Publications:

1. T. S. Majmudar and R. P. Behringer. "Contact force measurements and stress-induced anisotropy in granular systems." *Nature* **435**, 1079-1082 (2003).
2. Majmudar, T. S. and Behringer, R. P. "Contact forces and stress induced anisotropy.", Powders and Grains 2005, pp 65-68. Eds. Ramon Garcia-Rojo, Hans J. Herrmann and Sean McNamara. Balkema, Amsterdam.

Conferences Attended and Contributed Presentations

- American Physical Society, Division of Fluid Dynamics. (2000-2006).
- Dynamics Days Workshop (2001,2003).
- Gordon Research Conference: Granular and Granular Fluid Flow. (2004).
- Powders and Grains, 2005, Stuttgart, Germany.
- APS March Meeting, 2006, Baltimore, MD.